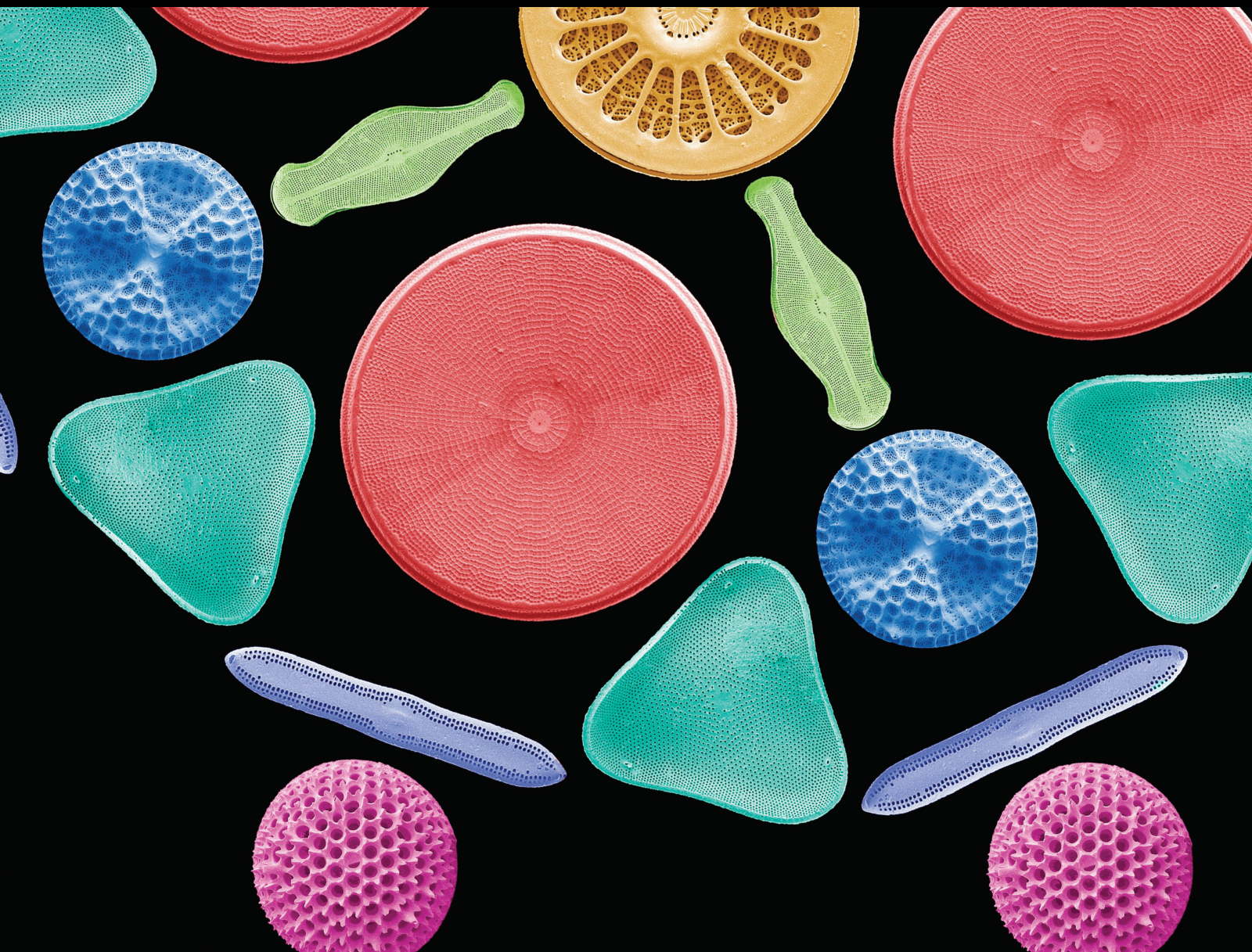# Application of Scanning Electron Microscopy in Metallurgical Research

Lead Guest Editor: Zhiping Xiong
Guest Editors: Andrii Kostryzhev, Yanjun Zhao, and Thaneshan Sapanathan

Application of Scanning Electron Microscopy in Metallurgical Research

Application of Scanning Electron Microscopy in Metallurgical Research

Lead Guest Editor: Zhiping Xiong
Guest Editors: Andrii Kostryzhev, Yanjun Zhao, and Thaneshan Sapanathan

Contents

WILEY | Hindawi

Research Article

Investigation on Microstructures and Mechanical Properties of the Hypoeutectic Al-10Si-0.8Fe-XEr Alloy

Peng Tang [iD],[1,2,3,4] **Yiyuan Liu** [iD],[1] **Yanjun Zhao** [iD],[1,2] **Zhiliu Hu**,[1,2] **Huachun Wang**,[3] **Linxin Peng** [iD],[4] **Songyun Deng**,[3] and **Kui Huang**[3]

[1]*School of Resources, Environment and Materials, Guangxi University, Nanning, China 530004*
[2]*Guangxi Key Laboratory of Processing for Non-ferrous Metal and Featured Materials, Guangxi University, Nanning, China 530004*
[3]*Guangxi Alnan Institute of Aerospace Transit Aluminum Alloy and Application, Nanning, China 530031*
[4]*School of Civil Engineering and Architecture, Guangxi University, Nanning, China 530004*

Correspondence should be addressed to Yanjun Zhao; zhaoyanjun71@163.com

In this paper, the effect of Er addition (0.2, 0.5, 0.65, 0.8, 1.0, and 1.5 wt. %) on the microstructure evolution and tensile properties of as-cast hypereutectic Al-10Si-0.8Fe alloy was investigated. The phases and their morphologies in these alloys were identified by XRD and SEM equipped with EDX with the help of metallographic analysis techniques; the length of the secondary phase (LSP) and secondary dendrite arm spacing (SDAS) of α-Al grain were quantified. The results indicated that the second phases (primary Si, eutectic Si, and iron-rich phases) and α-Al grain were significantly refined when the addition of Er increased from 0 to 0.8 wt. %. The mean LSP and SADS values were decreased to a minimum value when the Er addition reached 0.8 wt. %. However, the second phases and α-Al grain became coarser when the level of Er increased more than 0.8 wt. %. The analysis of XRD shows that Er mainly exists in the form of Er_2Si compound. The microstructure modification also has a significant effect on the mechanical properties of the alloy. The yield strength (YS), ultimate tensile strength (UTS), and elongation (EL) increase from 52.86 MPa, 163.84 MPa, and 3.45% to 71.01 MPa, 163.84 MPa, and 5.65%, respectively. From the fracture surface, the promotions of mechanical properties are due to the dispersion and pinning reinforcement caused by the Er_2Si phase.

1. Introduction

Al-Si alloys have low density, high strength, and excellent mechanical properties, which are widely used in the aerospace industry, the automotive industry, the construction industry, etc. [1–3]. With the development of science and technology, the performance requirements of cast Al alloy materials in various industries are constantly increasing. There are many ways to improve the performance of cast Al alloys, among which grain refinement is an efficient method [4, 5]. The commonly used refiners are Ce, La, Mn, and Ti [6–9], although research on refiners has achieved some results. But unfortunately, no efficient and cheap grain refiner has appeared. Therefore, better refinement effect and smaller cost consumption are the topics of continuous research by domestic.

In the processing of Al-Si alloys, a certain amount of Fe element is inevitably added. In order to simulate the actual use situation as much as possible, 0.8 wt% 在 element will be added in the experiment. Before the addition of a refiner, the second phase in Al-Si alloys is a bulk or plate-like Si phase, and long needle-like β-Fe phase appears when the Fe content increased [10–14]. The formation of these phases has an impact on the mechanical properties of aluminum alloys and reduces various mechanical properties. According to Qian et al.'s research [15], Er has a better regulation effect on the secondary phase in aluminum alloys. And Tantiwaitayaphan et al. [16] also reported that the addition of Er can reduce the degree of subcooling and cause the morphology of eutectic silicon to change. These research show that the rare earth element Er can improve the morphology of the secondary phase and improve the mechanical properties

of the aluminum alloys [17–21], but it has not been proposed which kind of particles the Er element will form with the Al-Si alloys to affect the morphology of the secondary phase.

In this experiment, Al-10Si-0.8Fe will be taken as an object. By increasing the content of the Er element, the effect of Er on the microstructure morphology, mechanical properties, and fracture behavior of the Al-10Si-0.8Fe alloy will be explored. The size of grains, the secondary phases, and the properties between secondary phases and the matrix would prominently impact the strength of these materials. And the second phases include primary silicon, eutectic silicon, and iron-rich phases. Therefore, we analyzed the statistical results of the secondary dendritic arm spacing (SDAS) and the length of second phase(LSP). By means of X-ray diffraction (XRD), scanning electron microscope (SEM)/energy-dispersive X-ray spectroscopy (EDX), and tensile fracture morphology, the principle and mechanism of adding the Er element to Al-Si-Fe alloy to enhance its properties were studied.

2. Experimental Materials and Methods

These hypoeutectic Al-10Si-0.8Fe-XEr (X = 0.0, 0.2, 0.5, 0.65, 0.8, 1.0, and 1.5 wt.%) alloys were developed using commercially pure Al (99.0 wt. %), Al-12Si master alloy, Al-75Fe master alloy, and Al-3Er master alloy through gravity casting method. There are also surface coatings (ZnO : Na_2SiO_3 : H_2O = 2 : 1 : 7), covering agents (NaCl : KCl = 1 : 1), refining agents C_2Cl_6, etc. The experiment was performed in a crucible resistance furnace, and the mass of the alloy smelted in each furnace was 600 g. The chemical compositions of the experimental alloys are listed in Table 1 (measured by the direct-reading spectrometer, SPECTROLAB/M11, Germany). The specific process is that the alloy Al-12Si and pure aluminum block are melted at 780°C, and the prepared iron agent is added, and the stirring is continued for 2 minutes to make the crucible composition more uniform and keep the temperature for 25 minutes. After raising the temperature to 800 ± 5°C, add an appropriate amount of Al-3Er intermediate alloy, stir and keep it for 25 min. The melt temperature is reduced to 720 ± 5°C, and the refining agent is added for deaeration after standing for 5 minutes. Finally, the slag pouring is performed, and the pouring temperature is 750 ± 5°C. Samples for metallurgical analysis and tensile testing were machined out from these cast ingots and cooled down at room temperature.

After the sample is prepared, the test sample is cut to obtain grinding, polishing, and corrosion treatment with HF solution (composed of 0.5 ml hydrofluoric acid and 100 ml H_2O) in order to better observe the metallographic phase. The metallographic analysis was conducted by the optical microscope (Zeiss/Observer. A1, Germany). The mean values of LSP and SDAS were evaluated using Nano-measurement software and statistical methods. At least 50 statistical samples were also randomly determined in each of the five view fields. Similar with the relevant literatures, the secondary dendrite arm spacing (SDAS) value and lengths of the second phases (LSP) were measured for investigating the effect of the added elements in these five view fields:

TABLE 1: Summary of the experimental alloys with different Er addition (unit: wt.%).

Sample no.	Addition content	Chemical composition of the experimental alloys			
		Si	Fe	Er	Al
#1	0	10.00	0.80	0.00	Bal.
#2	0.20	10.12	0.78	0.18	Bal.
#3	0.50	9.96	0.75	0.47	Bal.
#4	0.65	10.31	0.76	0.65	Bal.
#5	0.80	9.86	0.72	0.82	Bal.
#6	1.00	9.77	0.78	1.04	Bal.
#7	1.50	9.98	0.83	1.48	Bal.

$$\text{Mean L}_i = \frac{1}{m} \sum_{j=1}^{m} \left(\frac{1}{n} \sum_{i=1}^{n} L_i \right)_j, \tag{1}$$

where L_i is the LSP and SDAS of an arbitrary phase in the microstructure, n is the number of particles measured in a view field, and m is the number of the fields for quantification. In this case, the n value is determined as 50 and m is 5.

Meanwhile, these phases were observed by SEM (Hitachi TM4000Plus) coupled with EDX (IXRF 5500, USA) in this experiment, and the phase composition of the bulk sample was analyzed by XRD. Then, a universal testing machine is used to perform the tensile test to obtain the yield strength (YS), ultimate tensile strength (UTS), and elongation (EL) which were obtained at a strain rate of 1 mm/min. According to the ASTM E8M-04 standard, five tensile testing samples were machined out for each alloy. The fracture surfaces of these specimens were further investigated via the SEM.

3. Results

3.1. Evaluation Microstructure of Al-10Si-0.8Fe-XEr Alloys. The optical micrographs of Al-10Si-0.8Fe-XEr (X = 0.0, 0.2, 0.5, 0.65, 1.0, and 1.5) alloys are shown in Figure 1. In Figure 1(a), the Al-10Si-0.8Fe alloy contains needle-like second phase distributed around the dendritic α-Al, and the secondary dendrite arm spacing is relatively large. After adding the rare earth Er, the second phases were significantly refined from coarse polygonal and star-like shape to a fine block with smooth edges and corners when the addition of Er increased from 0 to 0.8%.When Er was added at 0.8 wt, the second phase had the best metamorphic effect and was the densest, and the second phase was refined into small particles, as shown in Figure 1(e). However, the second phases became coarser when the level of rare earth Er is more than 0.8%.

Figure 1(upper right corner) shows higher magnification metallographic images of these alloys. The Al-10Si-0.8Fe alloy contains gray, coarse needle-like eutectic silicon phase which is distributed around the α-Al phase, and the segregation is relatively serious; there are also a small number of polygonal bulky primary silicon phases in the structure. Most of the iron-rich phases are light gray, skeletal, or Chinese characters. They are entangled with eutectic silicon and adhere to the periphery of the α-Al phase. When Er is 0.8%,
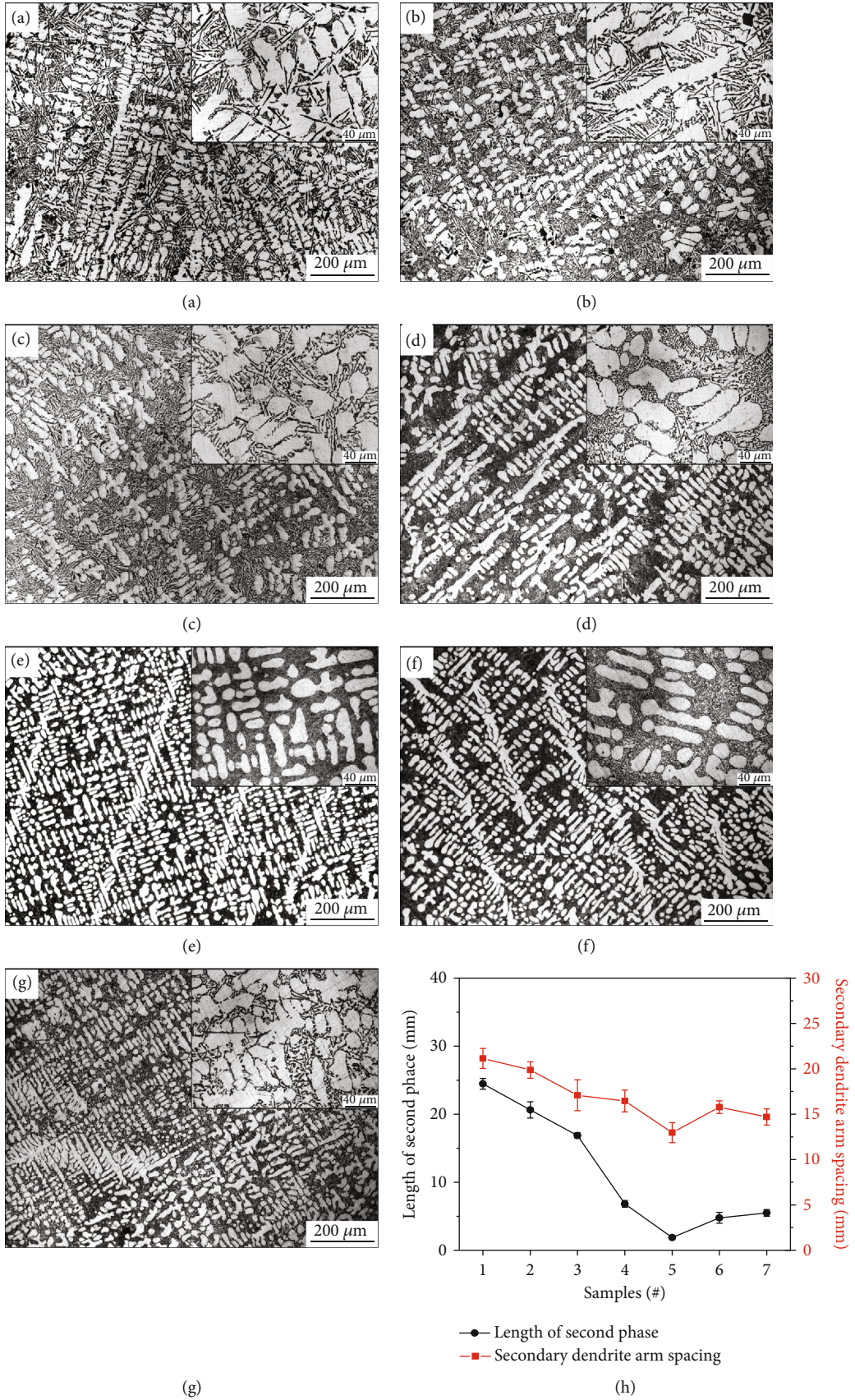
FIGURE 1: Optical micrographs of Al-10Si-0.8Fe alloys with different Er additions: (a) unmodified, (b) 0.20 wt.%, (c) 0.50 wt.%, (d) 0.65 wt.%, (e) 0.80 wt.%, (f) 1.00 wt.%, (g) 1.50 wt.%, and (h) statistical curve.

the α-Al dendrite grain boundaries have almost no edges, the shape becomes round and regular, and the structure becomes dense. The eutectic silicon distributed in the α-Al grain boundary is almost completely refined, and changes from a coarse needle-like shape to a dispersedly distributed fine particle or dot network.

The results in Figure 1(h)) indicated the eutectic silicon modification and the α-Al refinement effect of Er in the Al-10Si-0.8Fe alloy. When there is no Er element, the mean LSP and the SDAS values are 24.47 μm and 37.47 μm, respectively. As the amount of Er added increases, the mean LSP and SDAS values decrease rapidly. When the Er addition of Al-10Si-Fe alloy is 0.8%, the effect of refine and modification is the most obvious. The mean LSP and SDAS values reach the minimum value of 1.87 μm and 12.97 μm, respectively. When the amount of Er added continued to raise, the mean LSP gradually raised. Meanwhile, the value of SDAS gradually rose. After that, the SDAS values download again. Generally speaking, the SDAS value still showed an upward trend.

The XRD patterns of the rare earth element Er with different addition amounts are shown in Figure 2. The Er element will react with the silicon in the aluminum alloy to form an Er_2Si phase. At the same time, Al_9Si, $Al_{0.7}Fe_3Si_{0.3}$ and other phases also exist in the aluminum alloy.

The SEM with 0.2% and 1.0% Er are shown in Figure 3, and EDX are shown in Table 2. From Figure 3(a), the eutectic silicon in these alloys is mainly long and massive. According to the XRD and EDX, the gray needle phase at point 1 is presumed to be the Al-Si phase, and the white block at point 2 is the $Al_{0.7}Fe_3Si_{0.3}$ phase. From Figure 1, the alloy has been finely refined, and the eutectic silicon mainly appears in the form of short rods, particles, and thin strips. According to XRD and EDX, it can be inferred that the white particles in point 3 are the Er_2Si phase, and the white thin strips in point 4 are the AlSiEr phase. This shows that with the increase of Er content, the Er element starts to react with Al and Si to generate particles and thin phase. The addition of the Er element changed the morphology of the silicon phase and prevented its growth so that the second phase was refined.

3.2. Tensile Properties of the Al-10Si-0.8Fe-XEr Alloy. Figure 5 is a graph of the YS, UTS, and EL% of the Al-10Si-0.8Fe-*X*Er alloys. From Figure 5, the addition of Er improves the YS of the Al-10Si-0.8Fe alloy. The YS of the Al-10Si-0.8Fe alloy is 52.86 MPa. With the increase of the Er content, the YS of these alloys continues to increase. When the Er content increases from 0.5% to 0.65%, the YS of the alloy increases the most, 13.4%.When the content is 0.8%, the YS of the alloy is 71.01 MPa, which reaches the maximum value, which is about 34.3% higher than that of the Al-10Si-0.8Fe alloy. Once Er content is more than 0.8 wt.%, the yield strength of the alloy decreased significantly. The addition of Er element refines the eutectic silicon into fine particles, and the structure is uniform and dense. According to the Hall-Petch formula

$$\sigma = \sigma_0 + Kd^{-1/2}, \qquad (2)$$
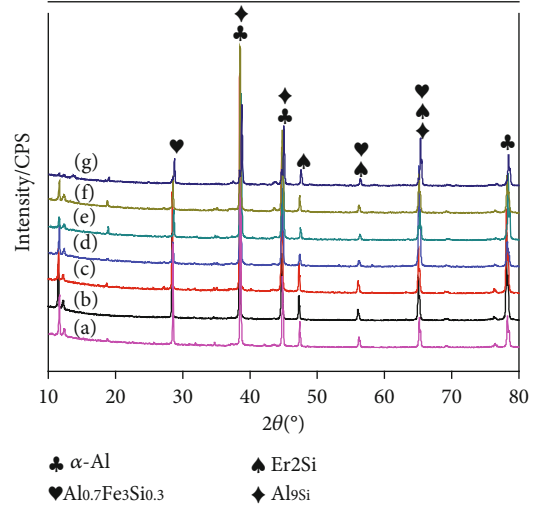
FIGURE 2: XRD patterns of alloys with different addition amounts of Er.

where σ is the yield strength, MPa; σ_0 is the yield strength of the single crystal, MPa; d is the grain size; and K is a constant.

With the refinement of grains, the interfacial area of the grains increases per unit volume and the grain boundaries hinder the movement of dislocations. The deformation caused by the stress during the stretching process can be dispersed into more grains. A great quantity of grain boundaries effectively hinders the movement of dislocations, and the dislocations continue to accumulate. Difficulty increases, and the yield strength of alloy materials in macroperformance increases. The experimental results show that when Er content is 0.8%, the grain size of the alloy structure reaches the minimum, and the yield strength reaches the maximum.

From Figure 5, the Er element also improves the UTS and %EL of the Al-10Si-0.8Fe alloy. When Er content is 0.8%, UTS reaches the maximum value of 213.31 MPa, increasing by 30.2%. When the content of Er exceeds 0.8%, UTS decreases, which may be due to the high content of Er and the large amount of long-needle iron-rich phase precipitation. Generally, with the increase of Er, the UTS of these alloys increases first and then decreases. When the content of Er is 0.8%, the UTS of these alloys are the highest. The %EL after fracture of the original alloy sample was 3.43%. When the Er content was 0.2%, eutectic silicon was refined and the %EL at break of the alloy increased slightly. When the content of Er increased to 0.5% and 0.65%, the length of the iron-rich phase in the tissue became longer, the morphology was mostly acicular, and the elongation rate decreased. The grain refining effect is best when Er content is 0.8%, the length of the iron-rich phase becomes shorter, the grain refining improves the deformation resistance of the alloy, and the elongation of the alloy reaches the maximum value. The maximum value was 5.49%, increasing by 60%.

The micrographs of the Al-10Si-0.8Fe-XEr alloy are shown in Figure 4. Figure 4(a)) shows the SEM image without Er, and it is clearly seen that the fracture surfaces are mainly covered by a cleavage surface without Er. This is

(a)

(b)
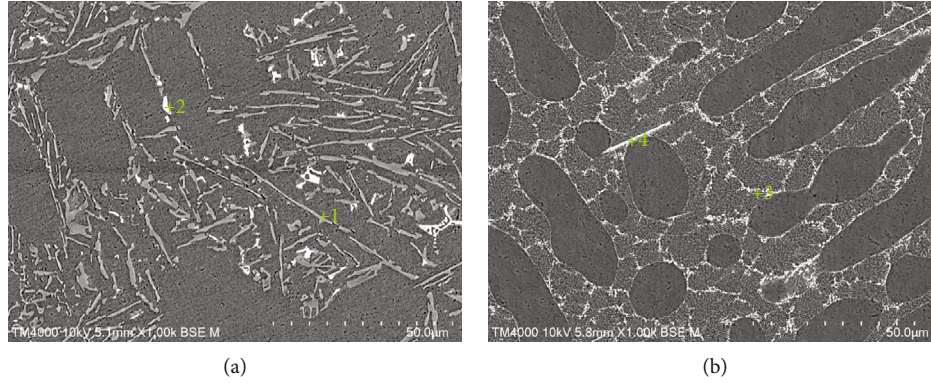
FIGURE 3: SEM morphology of alloys with different additions of Er: (a) 0.20 wt.% and (b) 0.80 wt.%.

TABLE 2: Elemental contents determined by EDX for the locations marked in Figure 4 (unit: at.%).

Point no.	Atomic (Al)%	Atomic (Si)%	Atomic (Fe)%	Atomic (Er)%
1	65.18 ± 2.10	34.82 ± 1.07	—	—
2	38.25 ± 1.12	36.15 ± 1.15	25.60 ± 1.13	—
3	8.82 ± 0.15	51.65 ± 2.20	4.92 ± 0.11	34.61 ± 1.07
4	37.02 ± 1.08	14.17 ± 0.21	—	48.81 ± 2.25

due to transgranular failure under the action of normal stress. The tensile fracture of the alloy showed a brittle fracture. It can be clearly seen from Figure 4(b) that the cleavage platform becomes smaller and a small number of dimples are formed. A small amount of white phase appears at the same time. Fractures also appear on the fibrous fracture surface. In addition, the number of folds and dimples increased with the increase of Er content. Meanwhile, seen from Figure 4(c), when the Er content reaches 0.8 wt.%, there are plenty of toughest fracture surface. And the white Er-rich phase is evenly distributed on the fracture surface, resulting in the best grain refining effect. Moreover, it can be observed that there are plenty of dimples present on the fracture surface. It is confirmed that the fracture mode of the alloy with the addition of 0.8 wt.% Er shows a mixed mode of brittle fracture and ductile fracture. However, when the addition of Er increased to 1.0 wt.%, a lager Er-rich phase appeared at fracture surface. It may reduce the tensile strength of the alloy.

In addition, EDS point analysis based on SEM (Figure 4) is shown at Table 3. According to Table 3, the gray cleaved surface (point 1) in Figure 4(b)) is the Al-Si phase. Point 2 is the white massive phase on the fracture. According to EDX, it can be known that the white phase is the Al-Si-Fe phase. And some Er elements are aggregated on the white phase. The fracture morphology corresponding to point 3 is gray fibrous. According to the results of EDX analysis, it can be known that the Er element content is higher here, which indicates that the Er element reacts with the matrix to form Er_2Si, which refines the eutectic silicon, thereby improving the alloy's strength. It can be seen from Figure 4(d)) that a number of white phase increases as the

amount of Er added increases, and they are more uniformly distributed on the substrate. As can be seen from EDX point 4 in Table 3, there is a great quantity of Er in the white phase, which means that excessive Er will coarse eutectic silicon, thereby reducing the tensile strength and increasing the brittleness of these alloys.

4. Discussion

In this study, the rare earth element Er can better refine the eutectic silicon in the Al-Si-Fe alloy, and the size of the eutectic silicon can be reduced by 38% when added in an appropriate amount. This is because during the nucleation and growth of α-Al grains during solidification, some Si and Fe atoms will enter the grains, and at the same time, some other elements will enrich the surface, making the α-Al grain size smaller [22]. The Er element added at the same time will generate the Er_2Si phase which can be used as heterogeneous nuclei to promote grain refinement. The growth surface of the eutectic silicon is (111), and it is preferentially grown during the solidification and crystallization process. When no refiner is added, the eutectic silicon continuously grows to the sides by atomic deposition on the inherent step of the grain boundary, so that the appearance becomes coarse strip and block phase. After adding the rare earth element Er, it will be deposited on the grain boundary. This makes the growth of the silicon phase nonuniform and accumulates on the twins, resulting in constitutional supercooling. At the same time, the growth mode of silicon is changed, which changes the morphology of the Si phase [23]. The thermodynamic formula is as follows:

$$\Delta Gv = -\frac{\Delta H \Delta T}{Tm}, \qquad (3)$$

where ΔGv is the phase change driving energy; ΔH is the latent heat of solidification; Tm is the equilibrium solidification temperature; and ΔT is the degree of subcooling.

According to the formula, when the subcooling degree becomes larger, the solidification driving force ΔGv also becomes larger. The enrichment of Er element will hinder the growth of the Si phase and cause the component to be too cold, preventing the Si phase from growing. As a result,
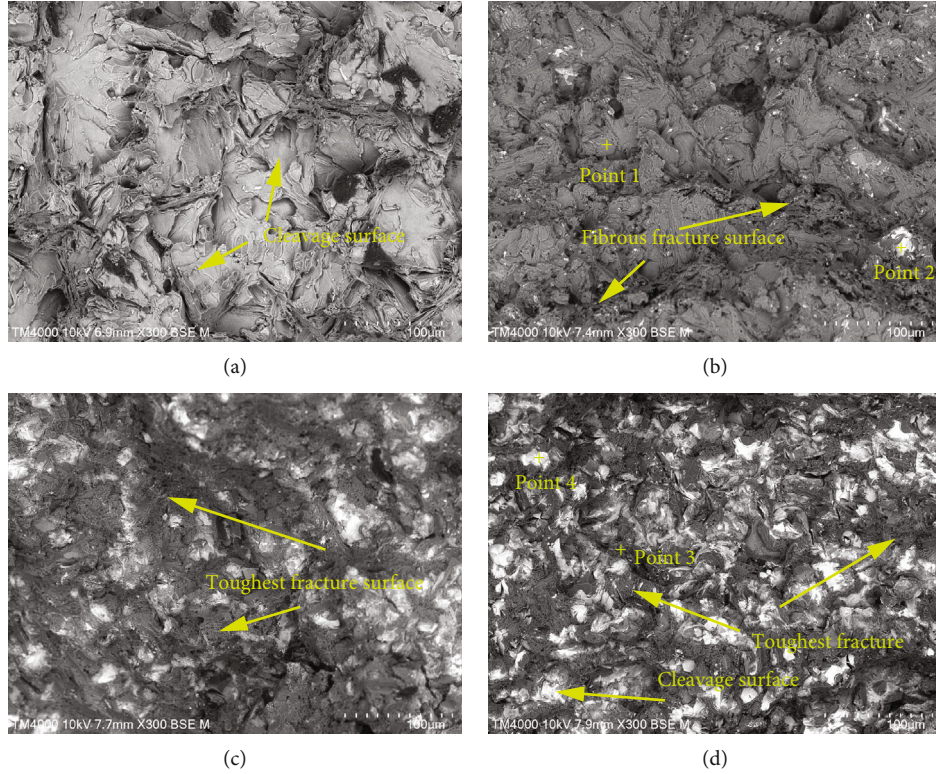
FIGURE 4: Fracture patterns of the Al-10Si-0.8Fe alloy with different amounts of Er: (a) unmodified, (b) 0.50 wt.%, (c) 0.80 wt.%, and (d) 1.00 wt.%.
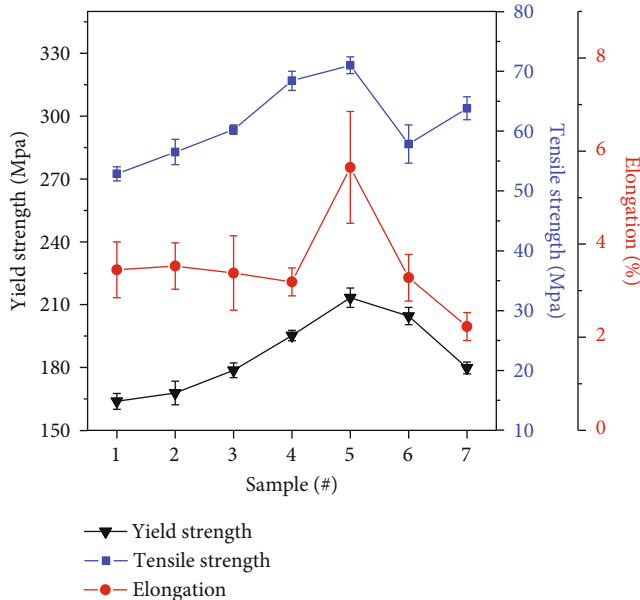
FIGURE 5: The YS, UTS, and %EL of the Al-10Si-0.8Fe alloy as functions of Er concentration.

TABLE 3: Elemental contents determined by EDX for the locations marked in Figure 4.

Point no.	Atomic (Al)%	Atomic (Si)%	Atomic (Fe)%	Atomic (Er)%
1	64.94 ± 1.10	35.06 ± 1.07	—	—
2	32.75 ± 0.74	33.82 ± 0.60	30.48 ± 1.20	2.95 ± 0.10
3	58.18 ± 1.42	4.77 ± 0.13	3.70 ± 0.07	33.35 ± 2.10
4	13.33 ± 0.10	3.78 ± 0.40	5.05 ± 0.30	77.84 ± 1.10

atomic weight, it can be more easily enriched on the surface of eutectic grains. This greatly hindered the directional growth of eutectic silicon, resulting in grain refinement [25, 26]. Obviously, according to the experimental results, the aluminum alloy grains are refined. We believe that maybe there are some strengthened mechanisms in the composites, which we have not considered.

5. Conclusions

(1) In Al-10Si-1.5Fe-XEr alloys, Er can significantly modify the second phases (include primary silicon, eutectic silicon, and iron-rich phases) of the Al-10Si-0.8Fe alloy that the morphology transfers from the coarse needle to fine granular and its size decreases to $1.87\,\mu$m when the addition of Er is 0.8%. However, a further increase in the amount of

the morphology of the Si phase has changed from a bar shape to a short rod shape [24]. At the same time, some literatures pointed out that when Al and Si in the melt undergo eutectic transformation, a small amount of Er atoms are still present. And because Er atom has a smaller atomic radius and a larger

addition of Er more than 0.8% leads to coarsening of the second phases

(2) Adding the Er element can improve the mechanical properties of the Al-Si-Fe alloy. Compare with the Al-10Si-1.5Fe alloy, when the Er addition is 0.8 wt. %, the YS, UTS, and %EL increase from 52.86 MPa, 163.84 MPa, and 3.45% to 71.01 MPa, 163.84 MPa, and 5.65%, respectively. However, excess Er can lead to a decrease in the strength and toughness of these alloys

(3) Adding an appropriate amount of element Er to the iron-rich Al-Si alloy can precipitate the Er_2Si phase in the structure and finely refine the eutectic silicon phase in the alloy structure

Data Availability

The [Manuscript.doc] data used to support the findings of this study have been deposited in the [Investigation on Microstructures and Mechanical Properties of the Hypoeutectic Al-10Si-0.8Fe-xEr Alloy] repository (9147871). The datasets used or analyzed during the current study are available from the corresponding author on reasonable request. Actually, all data generated or analyzed during this study are included in this published article.

Conflicts of Interest

The authors declare that they have no conflicts of interest.

Acknowledgments

References

[1] K. Wang, P. Tang, Y. Huang, Y. Zhao, W. Li, and J. Tian, "Characterization of Microstructures and Tensile Properties of Recycled Al-Si- Cu-Fe-Mn Alloys with Individual and Combined Addition of Titanium and Cerium," *Scanning*, vol. 2018, no. 1, Article ID 3472743, 14 pages, 2018.

[2] H. Jian, F. Jiang, Z. Xu, and D. Guan, "Study progress of high strength and tenacity Al-Zn-Mg-Cu aluminum alloy for aviation," *Hot Working Technology*, vol. 6, no. 35, pp. 66–71, 2006.

[3] J. Hirsch, "Recent development in aluminium for automotive applications," *Transactions of Nonferrous Metals Society of China*, vol. 24, no. 7, pp. 1995–2002, 2014.

[4] M. A. Easton, M. Qian, A. Prasad, and D. H. StJohn, "Recent advances in grain refinement of light metals and alloys," *Current Opinion in Solid State and Materials Science*, vol. 20, no. 1, pp. 13–24, 2016.

[5] P. Tang, Z. Hu, Y. Zhao, and Q. Huang, "Investigation on the solidification course of Al-Si alloys by using a numerical Newtonian thermal analysis method," *Materials Research Express*, vol. 4, no. 12, 2017.

[6] E. M. Elgallad, H. W. Doty, S. A. Alkahtani, and F. H. Samuel, "Effects of La and Ce addition on the modification of Al-Si based alloys," *Advances in Materials Science and Engineering*, vol. 2016, Article ID 5027243, 13 pages, 2016.

[7] S. C. Wang, N. Zhou, D. F. Song, and D. Nong, "Effects of La and Ce mixed rare earth on microstructure and properties of Al-Mg-Si aluminum Alloy," *Materials Science Forum*, vol. 898, pp. 367–371, 2017.

[8] S. K. Shaha, F. Czerwinski, W. Kasprzak, J. Friedman, and D. L. Chen, "Effect of Mn and heat treatment on improvements in static strength and low- cycle fatigue life of an Al–Si–Cu–Mg alloy," *Materials Science and Engineering: A*, vol. 657, pp. 441–452, 2016.

[9] P. TANG, W. LI, Y. ZHAO, K. WANG, W. LI, and F. ZHAN, "Influence of strontium and lanthanum simultaneous addition on microstructure and mechanical properties of the secondary Al-Si-Cu-Fe alloy," *Journal of Rare Earths*, vol. 35, no. 5, pp. 485–493, 2017.

[10] Q. Li, Y. Zhu, B. Li et al., "Effect of iron addition on the microstructures and properties of hypereutectic Al-20% Si alloys," *Materials Research Express*, vol. 6, no. 1, p. 016506, 2018.

[11] O. Elsebaie, A. M. Samuel, H. W. Doty, S. Valtierra, and F. H. Samuel, "On the impact properties and fractography of Al–11% Si casting alloy," *International Journal of Metalcasting*, vol. 12, no. 1, pp. 36–54, 2018.

[12] M. M. Haque, N. I. Syahriah, and A. F. Ismail, "Effect of silicon on strength and fracture surfaces of aluminium–silicon casting and Heat Treated Alloys," *Fracture and Strength of Solids VI*, vol. 306 - 308, pp. 893–898, 2006.

[13] Y. Wang, R. Guan, D. Hou, Y. Zhang, W. Jiang, and H. Liu, "The effects of eutectic silicon on grain refinement in an Al–Si alloy processed by accumulative continuous extrusion forming," *Journal of Materials Science*, vol. 52, no. 2, pp. 1137–1148, 2017.

[14] M. F. Ibrahim, *Effects of Be, Sr, Fe and Mg interactions on the microstructure and mechanical properties of aluminum based aeronautical alloys, [Ph.D. thesis]*, Université du Québec à Chicoutimi, Chicoutimi, QC, Canada, 2015.

[15] H. Qian, D. Zhu, C. Hu, and X. Jiang, "Effects of Zr additive on microstructure, mechanical properties, and fractography of Al-Si alloy," *Metals*, vol. 8, no. 2, p. 124, 2018.

[16] T. Tantiwaitayaphan, P. Pandee, and C. Limmaneevichitr, "Modification of eutectic si in hypoeutectic al-si alloys with erbium addition," *Key Engineering Materials*, vol. 718, pp. 139–142, 2016.

[17] M. Colombo, E. Gariboldi, and A. Morri, "Influences of different Zr additions on the microstructure, room and high temperature mechanical properties of an Al-7Si-0.4Mg alloy modified with 0.25%Er," *Materials Science and Engineering: A*, vol. 713, pp. 151–160, 2018.

[18] R. Ahmad, N. A. Wahab, S. Hasan, Z. Harun, M. M. Rahman, and N. R. Shahizan, "Effect of erbium addition on the microstructure and mechanical properties of aluminium alloy," *Key Engineering Materials*, vol. 796, pp. 62–66, 2019.

[19] S. Seetharaman, C. Blawert, B. M. Ng et al., "Effect of erbium modification on the microstructure, mechanical and corrosion characteristics of binary Mg–Al alloys," *Journal of Alloys and Compounds*, vol. 648, pp. 759–770, 2015.

[20] B. He, M. Qin, and B. Huang, "Effect of trace element Er on the mechanical properties of A356 aluminum alloy," *Light Alloy Fabrication Technology*, vol. 6, p. 4, 2017.

[21] W. J. Lv, B. L. Li, P. Qi, and Z. R. Nie, "The effect of the erbium content on the microstructure and mechanical property of 6061 aluminum Alloys," *Materials Science Forum*, vol. 898, pp. 35–40, 2017.

[22] Z. M. Shi, Q. Wang, G. Zhao, and R. Y. Zhang, "Effects of erbium modification on the microstructure and mechanical properties of A356 aluminum alloys," *Materials Science and Engineering: A*, vol. 626, pp. 102–107, 2015.

[23] Y. Hong, Z. Jingqi, and S. Zhang, "Research progress on rare earth aluminium alloy modification," *Materials Reports*, vol. 27, no. S2, pp. 285–287, 2013.

[24] S.-Z. Lu and A. Hellawell, "Growth mechanisms of silicon in Al-Si alloys," *Journal of Crystal Growth*, vol. 73, no. 2, pp. 316–328, 1985.

[25] C. Booth-Morrison, D. N. Seidman, and D. C. Dunand, "Effect of Er additions on ambient and high-temperature strength of precipitation-strengthened Al–Zr–Sc–Si alloys," *Acta Materialia*, vol. 60, no. 8, pp. 3643–3654, 2012.

[26] P. Tang, W. Li, K. Wang et al., "Effect of Al-Ti-C master alloy addition on microstructures and mechanical properties of cast eutectic Al-Si-Fe-Cu alloy," *Materials & Design*, vol. 115, pp. 147–157, 2017.

WILEY | Hindawi

Research Article
Correlation between Fracture Morphology and Microstructural Evolution during Long-Term Aging of EK61 Superalloy

Jin Huang,[1,2] **Guohua Xu,**[2] **Heyong Qin,**[2] **and Lei Zheng** ⓘ[1]

[1]*School of Materials Science and Engineering, University of Science and Technology Beijing, Beijing 100083, China*
[2]*High-Temperature Materials Department, China Iron & Steel Research Institute Group, Beijing 100081, China*

Correspondence should be addressed to Lei Zheng; zhenglei_ustb@sina.com

Microstructural evolutions of EK61 superalloy during long-term aging until 1000 h at 700°C and 750°C, respectively, are studied by combination of Scanning Electron Microscope (SEM) and Transmission Electron Microscope (TEM). Impact fracture morphologies after aging for different time are observed by the SEM. The microstructure is found to be relatively stable during aging at 700°C, and the fracture morphologies are characterized by transgranular fracture. At 750°C, the coarsening of γ' phase leads the reduction of the quantity of dimples, the chainization of carbides on grain boundaries leads to intergranular fracture, and the netting of η phases within grains leads to the formation of lamellar cleavage steps. It is obvious that the destabilization of precipitated phases affects fracture morphology significantly. The relationship between fracture morphology and the microstructure promotes the evaluation of service reliability of EK61 superalloy.

1. Introduction

Nickel-based superalloy EK61 can maintain good stability and excellent mechanical properties in the range of -253°C to 750°C. At present, EK61 superalloy is mainly used in rocket engine turbine disk [1–6]. As well known, the service conditions of the engine turbine disk are quite harsh. The disk often works in the oxygen-enriched gas environment of high pressure and large flow rate and also needs to bear high stress cycle load. In order to ensure the reliability of the engine turbine disk for a long time in such an environment, the EK61 alloy must have excellent comprehensive mechanical properties. Impact toughness is one of the important properties [7], which can be used to evaluate the toughness and brittleness of the alloy and to reveal the brittle fracture tendency of the material [8].

Impact fracture morphology can show the fracture mechanism intuitively, which is very helpful to the failure analysis [9]. It is obvious that fracture morphology is related directly to microstructure [10]. From the point of the growth of η phase and the coarsening of γ' phase during aging, Zhao and Xie [11] analyze the formation process of brittle impact

fracture of a new nickel-based superalloy. Claudio Gennaria et al. [12] found that the precipitation of a small quantity of phases with different morphologies in UNS S32205 steel decreased the impact properties of the alloy.

On the basis of previous studies, the nickel-based superalloy EK61 is aged for a long time at different temperatures. The microstructure and impact fracture morphology during aging are observed and analyzed. The effect of microstructure degradation on ductile-brittle transition of EK61 superalloy during long-term aging is studied, which provides a basis for failure analysis and safety evaluation.

2. Materials and Methods

The experimental material used in this paper is the forged EK61 alloy. The chemical composition is shown in Table 1.

The alloy is first heat-treated at 980°C × 1 h/water quench + 730°C × 15 h/water quench + 650°C × 10 h/water quench. Then the aging is carried out at 700°C and 750°C for 30 h, 100 h, 200 h, 500 h, and 1000 h, respectively. After aging, the samples are polished and corroded. The erosion regime is 20%H_2SO_4 + 80%CH_3OH, 20-25 V voltage, 20-25 s erosion

TABLE 1: Chemical composition of EK61 superalloy, wt. %.

Element	C	Cu	Al	Fe	Cr	Ti	Mo	Nb	Si	Mn	S	P
Content	0.05	0.5	1	14	16	0.5	4	4.5	≤0.2	≤0.1	≤0.004	≤0.009

time, and $150\,ml\,H_3PO_4 + 10\,ml\,H_2SO_4 + 15\,gCrO_3$, voltage 3-4 V, 5-7 s erosion time.

The precipitated phases are observed by Field-Emission Scanning Electron Microscope (FE-SEM) and identified by Scanning Electron Microscope-Energy Dispersive Spectrometer (SEM-EDS) and TEM. The impact test is carried out at room temperature, using a JB-30B Charpy impact machine with impact energy of 0~300 J, and the pendulum falling speed is $5.2\,m\cdot s^{-1}$. The dimension of the specimens is 55 mm $\times$ 10 mm $\times$ 10 mm. There is a V-groove in the middle of the specimen with 2 mm depth. The fracture surface is protected and then cut by wire cutting machine. The fracture samples are cleaned ultrasonically for 15 minutes and then observed by the SEM after drying.

3. Results and Discussion

3.1. Evolution of Impact Property after Long-Term Aging at Different Temperature.
Table 2 lists the impact property at room temperature of EK61 superalloy after long-term aging at 700°C and 750°C. It can be seen that the impact property gradually decreases with increased aging time.

3.2. Evolution of Microstructure during Long-Term Aging.
Figure 1 shows the microstructure evolution of EK61 superalloy during aging at 700°C. The average sizes of γ' phases in bulk after aging for different time are obtained and listed in Table 3, which displays that γ' phase grows gradually during aging for 30-200 h. At the same time, it can be seen that the morphologies of γ' phases and carbides at grain boundaries keep almost unchanged. In addition, a needle-like phase starts to appear after aging for 30 h and becomes more obvious as time extends. During aging from 500 h to 1000 h, the average sizes of γ' phases in bulk increase still gradually. The size of carbides at grain boundaries becomes larger, and the shape changes from short slice to short bar. The needle-like phase becomes longer and thicker. It is noteworthy that there are obvious γ' phase-depleted zones around the needle-like phases and carbides, as indicated by the arrows in Figure 2, which proves the precipitating of needle-like phases to be at the expense of γ' phases. During long-term aging, thermodynamically, the γ' phases became metastable, and therefore transform to the more stable needle-like phases [13]. From Figure 1, it can be concluded that the main precipitates are γ' phases, needle-like phases, and carbides. During aging, the microstructure degenerates gradually.

Figure 3 shows the microstructure evolution of EK61 superalloy during aging at 750°C. The average sizes of γ' phases in bulk after aging for different time are also obtained and listed in Table 3, which displays that γ' phase grows continuously during aging until 1000 h, and the average size is larger than that at 700°C for a certain aging time. During

TABLE 2: Impact property at room temperature of EK61 superalloy after long-term aging.

Aging time (h)	Aged at 700°C		Aged at 750°C	
	Akv (J)	Error	Akv (J)	Error
30	49.0	±7.08	47.0	±7.37
100	37.0	±3.06	37.5	±9.09
200	38.5	±2.75	32.0	±10.04
500	27.5	±1.89	30.0	±8.01
1000	16.5	±3.21	26.0	±2.25

aging, the carbides at grain boundaries change from discontinuous short rod and block to continuous chains. The long needle-like phases are small, scattered, and short at the beginning. They evolve form the larger dendritic shape gradually and form a net after 500 h aging that covers the entire grain. EDS measurements listed in Table 4 show that the long needle-like phases are $Ni_6(Al, Ti, Nb)$ after 500 h aging and determined to be η phases by TEM lattice calibration (as indicated by the arrows in Figure 4). The orientation relation between η phase and bulk is also shown in Figure 4. It can be concluded from Figure 3 that the main precipitates are γ' phases, η phases, and carbides either. Besides, the microstructure degenerates during aging as well. The higher the aging temperature is, the more serious the degradation is.

3.3. Impact Fracture Morphology.
Figure 5 shows the impact fracture morphology after aging at 700°C for different time. When aged for 30-200 h, the fracture surface morphology shows dimples mainly and broken carbides can be seen at the bottom of several dimples (as indicated by the arrows). With the extension of aging time to 500 h, dimples become shallow and small. Moreover, tearing edges appear and the quantity of dimples on the fracture surface decreases. When aging for 1000 h, dimples become even shallower and smaller. At the same time, the amount of tearing edges increases. It is clear that the main feature of fracture morphology is dimple and tearing edge even after aging of 1000 h, and the fracture is still transgranular ductile mode.

Figure 6 shows the impact fracture morphology after aging at 750°C for different time. During aging for 30-200 h, the fracture morphology shows dimples mainly, and the fracture mode is transgranular. The dimples are small and shallow. Broken carbides can also be seen at the bottom of several dimples (as indicated by the arrows). After aging for 500 h, the fracture morphology changes significantly. The dimples on the fracture surface are seldom observed while short and bending tearing appears obviously. Furthermore, the fracture surface begins to show the characteristics of intergranular fracture (as indicated by the arrows), and lamellar cleavage steps appear within the grains (as indicated

(a)

(b)

(c)

(d)

(e)

Figure 1: Microstructure after aging at 700°C for different time: (a) 30 h, (b) 100 h, (c) 200 h, (d) 500 h, and (e) 1000 h.

Table 3: Diameter of γ' phases after long-term aging.

Temperature (°C)			700					750		
Time (h)	30	100	200	500	1000	30	100	200	500	1000
Diameter (nm)	21.66	25.93	31.93	36.86	44.12	27.02	38.84	41.95	55.24	72.60
Error (nm)	0.129	0.301	0.082	0.186	0.132	0.047	0.091	0.143	0.218	0.094

FIGURE 2: γ' phase depletion zones around needle-like phases aging for 1000 h at 700°C.
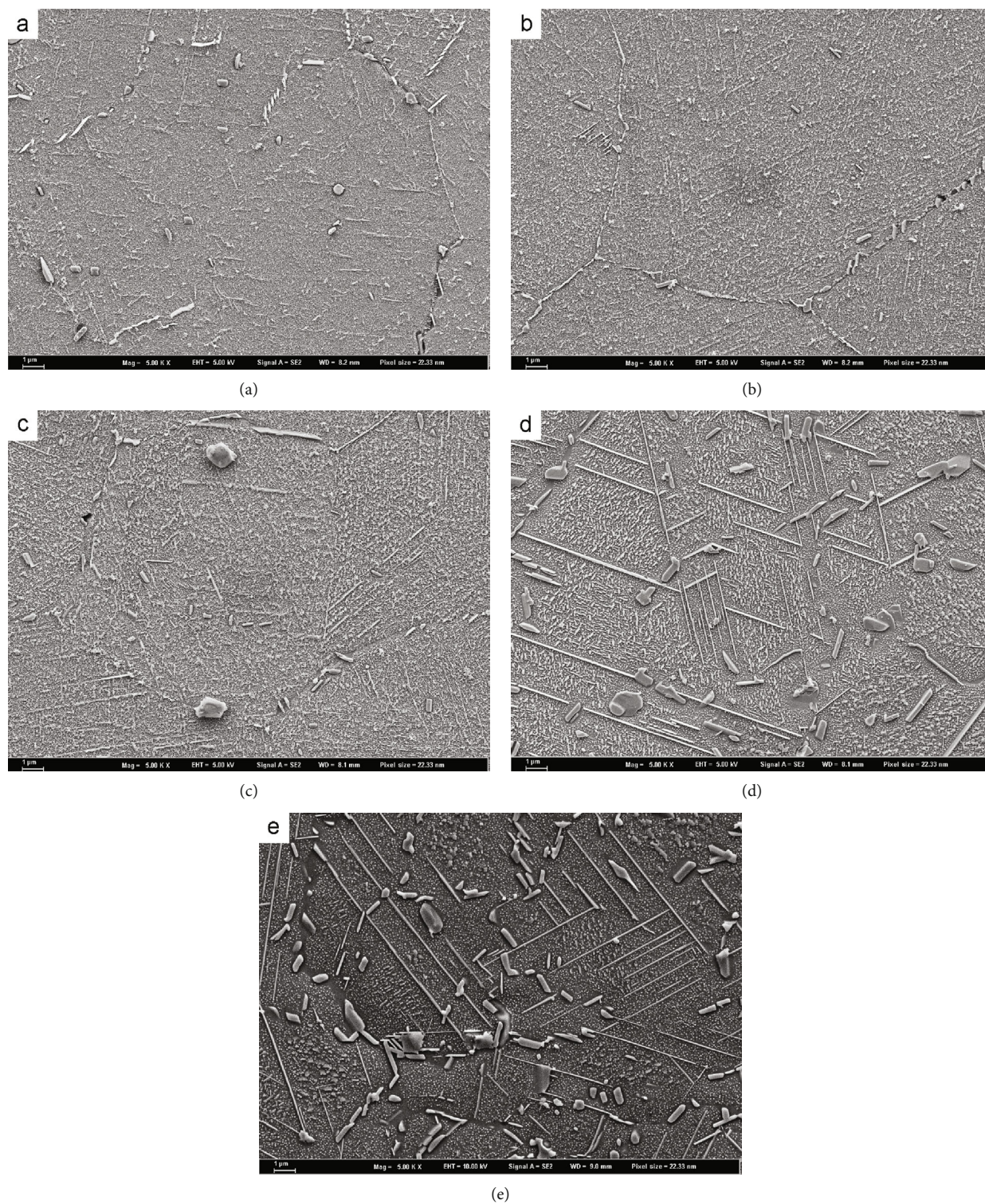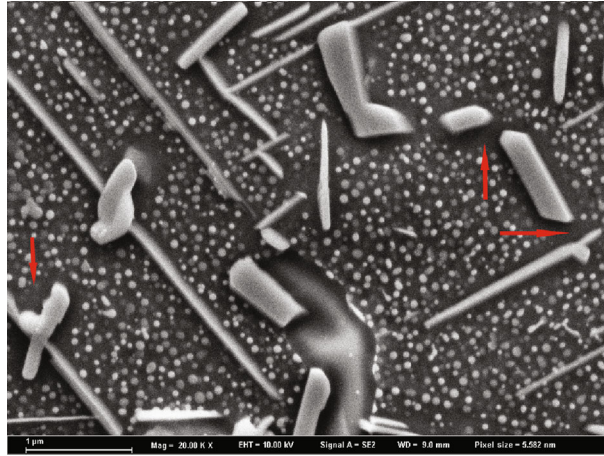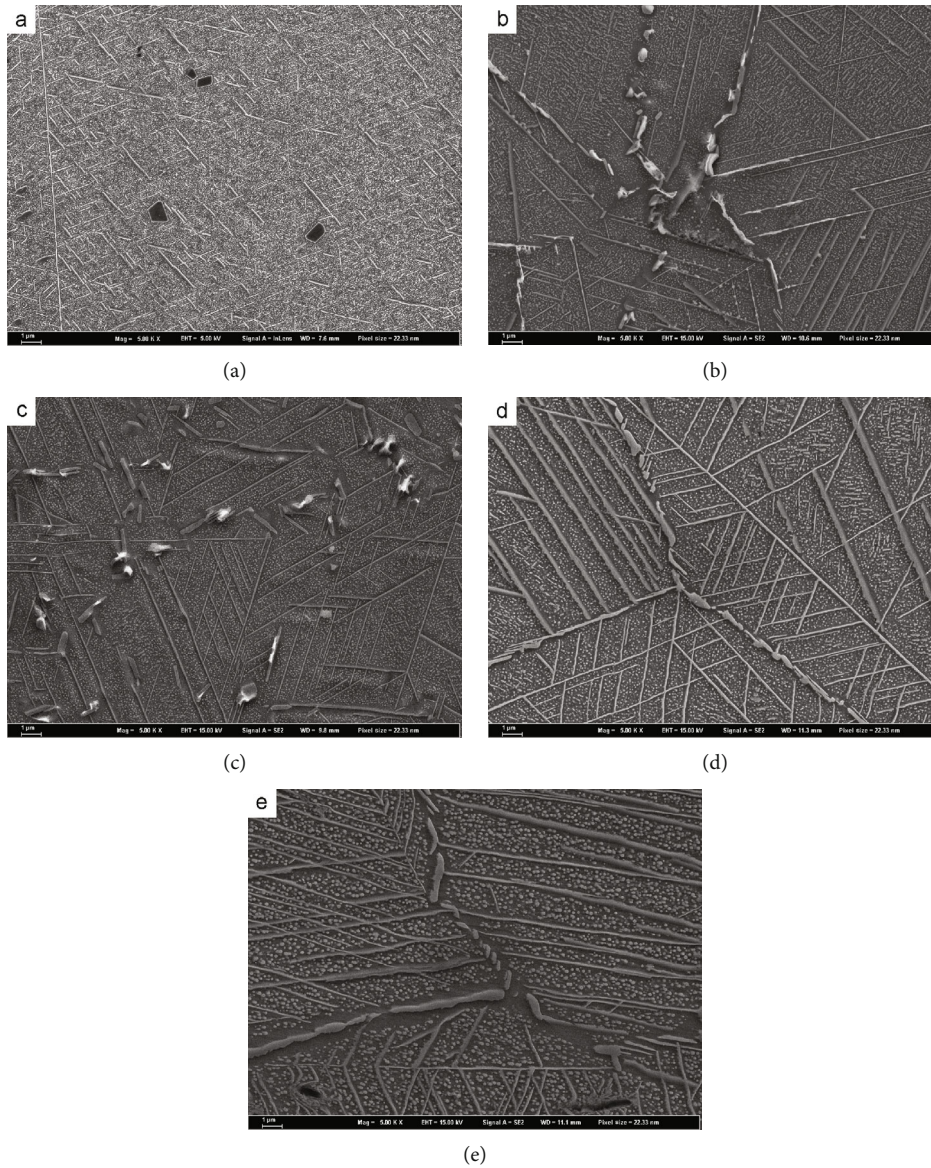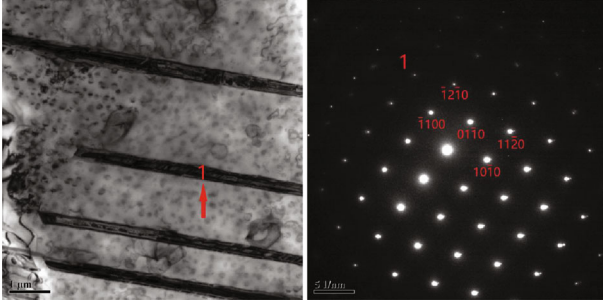

(a)

(b)

(c)

(d)

(e)

FIGURE 3: Microstructure after aging at 750°C for different time: (a) 30 h, (b) 100 h, (c) 200 h, (d) 500 h, and (e) 1000 h.

TABLE 4: EDS results of needle-like phases after aging 1000 h at 750°C.

Element	Al	Ti	Cr	Fe	Ni	Nb	Mo
Wt. %	1.70	1.04	11.42	8.66	60.75	12.64	3.80
At. %	3.78	1.30	13.15	9.29	61.97	8.15	2.37

FIGURE 4: TEM morphology and calibration of SADPs of η phase aging for 1000 h at 750°C. $[2\bar{1}\bar{1}0]\eta//[1\bar{1}0]\gamma$.

by the stars). After aging for 1000 h, the fracture surface exhibits evident intergranular fracture characteristics (as indicated by the arrows) and is full of lamellar cleavage steps within the grains, which demonstrates the fracture to be significantly brittle.

4. Discussion and Analysis

It can be seen that both the aged microstructure and the fracture morphology take significant changes at 750°C while they are relatively stable at 700°C, indicating that the change of aged microstructure influences the fracture morphology directly [14–16].

It is well known that γ' phase is harder than the matrix. In the process of deformation, γ' phase is difficult to deform, which leads to the formation of a weak zone interface between γ' phase and matrix. In this case, microcracks are easily initiated at the γ/γ' interface [17]. At the crack tip, the stress state is basically triaxial. Thus, the microcrack will form a small plastic pit with γ' phase in the grain as the core. Afterwards, it forms dimples representing the morphology of the ductile fracture. Therefore, the density, depth, and distribution of dimples depend on the number, size, and distribution of γ' phases, respectively [15]. During the long-term aging at 700°C and 750°C, γ' phases only coarsen and the morphology keeps granular. Since the size of γ' phase increases and the volume fraction decreases, the size and the quantity of dimples on the fracture surface decrease.

Carbides within the bulk will also induce dimples when the local stress is over the strength of carbides. Similarly, a microcrack initiates and thus a small plastic pit will develop into a dimple after fracture. However, because the amount of carbides within the bulk is much less than that of γ' phases, the density, depth, and distribution of the dimples are seldom affected by carbides within the bulk. As for the carbides at grain boundaries, they play two roles affecting

mechanical properties of superalloy according to different morphologies [18]. When the carbides are dispersed in grain boundaries, they can not only strengthen the grain boundary by increasing the difficulty of grain boundary slipping but also pin the grain boundaries to inhibit the grain coarsening under high temperature. In this case, the effect of carbides is positive [19]. Whereas when carbides are distributed at grain boundaries in the form of continuous flakes, dislocations are blocked at the interface between carbides and matrix γ, resulting in stress concentration. In addition, the coarsening of grain boundary carbides will consume strengthening elements (Ti, Mo, Nb, etc.) and leads to the formation of weak areas at near grain boundaries. Under this circumstance, the stress concentration occurs easily at the carbides when the alloy is impacted and thus causes microcrack initiation. Subsequently, microcracks connect continuously and bring out intergranular fracture finally. As a result, the chainization of carbides at grain boundaries leads to intergranular fracture and grain boundary embrittlement during impact. During the aging process at 700°C (see Figure 2), the carbides do not form a chain and thus the impact fracture mode is always transgranular. From Figure 3, it is seen that aging at 750°C for 30 h, the carbides precipitate discontinuously at grain boundaries. After 500 h aging, carbides form a chain nearly and the fracture surface begins to show intergranular fracture characteristics. After aging for 1000 h, the carbides at grain boundaries form obvious chains, and the impact fracture morphology is mainly intergranular fracture.

It is obvious that η-Ni_6(Al, Nb, Ti) phases [20] grow in a way of needle expansion and present the distribution of array arrangement during aging. The growth of η phase consumes elements of Al, Ti, and Nb that form γ' phases and thus results in γ' phase depletion zone around the η phase. The strength of this depletion zone is thus low due to the lack of γ' hardening. During deformation, dislocations are obstructed by η phases and accumulated in front of η phases. Since the depletion zone is relatively weak, the microcrack will emerge. From Figure 3, it is known that short rod η phases precipitate visibly within grains after aging at 750°C for 30 h, and the distribution of array arrangement can be observed. However, the fracture morphology shows obvious lamellar cleavage only after aging for 500 h (see Figure 6). It is notable that the thick η phases form a network structure after aging for 500 h and covering the whole grains with the aging time up to 1000 h. Therefore, it is the netting of η phases that leads to the formation of intergranular lamellar cleavage steps. After aging at 700°C for 1000 h, the degree of growth of η phase is similar to that aged at 750°C for 200 h. There is no cleavage step on the fracture surface during aging at 700°C, which further indicates that the netting of η phases induces the cleavage fracture morphology.

(a)

(b)

(c)

(d)

(e)
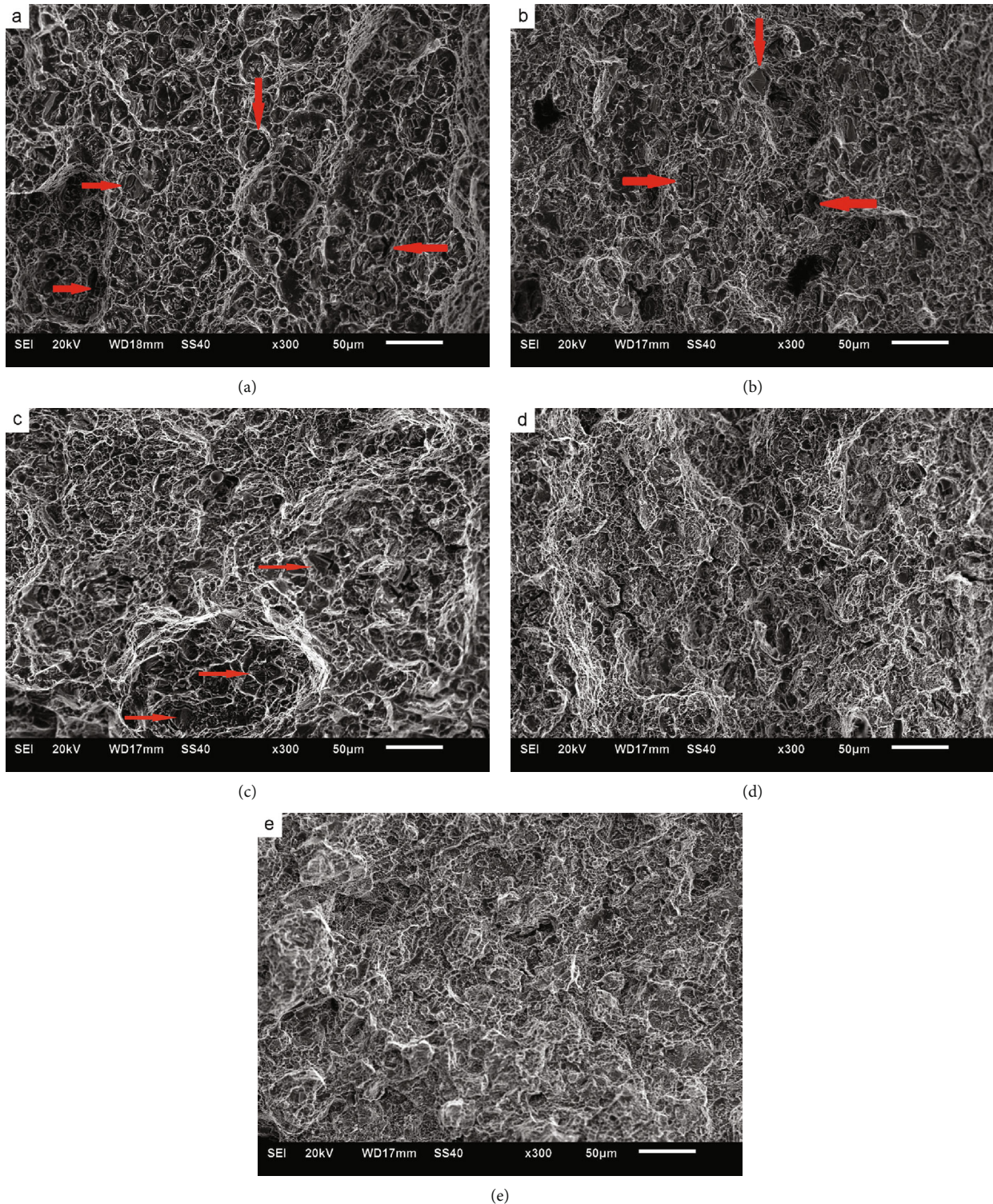
Figure 5: Impact fracture after aging at 700°C for different time: (a) 30 h, (b) 100 h, (c) 200 h, (d) 500 h, and (e) 1000 h.

5. Conclusions

Microstructure degenerated clearly during aging at 750°C, which is indicated by the coarsening of γ' phases, the chainization of carbides at grain boundaries, and the netting of η phases. while the microstructure during aging at 700°C is relatively stable, which is indicated by the less size of γ' phases, the less amount of η

(a)

(b)

(c)

(d)

(e)
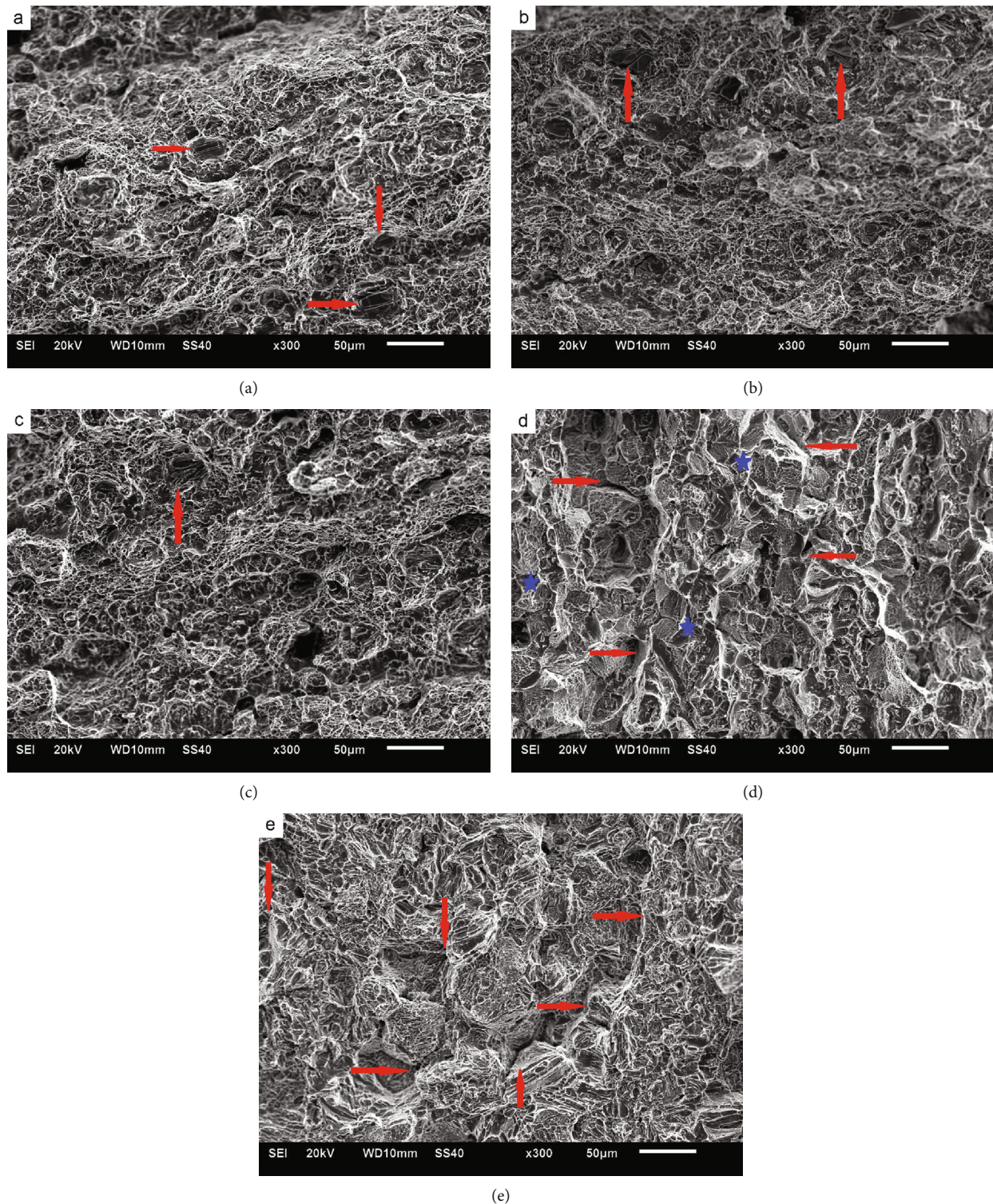
Figure 6: Impact fracture after aging at 750°C for different time: (a) 30 h, (b) 100 h, (c) 200 h, (d) 500 h, and (e) 1000 h.

phases, and the unchained distribution of carbides at grain boundaries.

Microstructure degradation is the main reason for the change of fracture morphology. The coarsening of γ' phases leads to the decrease in the quantity of dimples, the chainization of carbides at grain boundaries leads to the intergranular fracture, and the netting of η phases leads to the formation of lamellar cleavage steps.

Data Availability

All the data used to support the findings of this study are included within the article.

Conflicts of Interest

The authors declare that they have no conflicts of interests.

Acknowledgments

References

[1] A. M. Polyanskii and V. M. Polyanskii, "Structural changes in alloy ÉK61 due to cyclic deformation at elevated temperature," *Metal Science and Heat Treatment*, vol. 52, no. 5-6, pp. 279–283, 2010.

[2] V. N. Semenov, N. V. Akimov, and V. P. Glushko, "Formation of cracks in EP202 and EK61 alloys in welding of structures of liquid rocket engines," *Welding International*, vol. 27, no. 2, pp. 159–162, 2013.

[3] K. I. Nedashkovskii, O. N. Zheleznyak, B. M. Gromyko, B. A. Kozykov, and I. A. Mikhalev, "Effect of low temperatures on mechanical and physical properties of high-strength nickel alloy ÉK61ID and stainless maraging steel ÉK49VD," *Metal Science and Heat Treatment*, vol. 45, no. 5-6, pp. 233–236, 2003.

[4] E. Galieva, V. Valitov, R. Lutfullin, and A. Bikmukhametova, "Low-temperature superplasticity of the Ni-based EK61 superalloy and application of this effect to obtain Sound solid phase joints," *Defect and Diffusion Forum*, vol. 385, pp. 150–154, 2018.

[5] M. Jouiad, E. Marin, R. S. Devarapalli et al., "Microstructure and mechanical properties evolutions of alloy 718 during isothermal and thermal cycling over-aging," *Materials and Design*, vol. 102, pp. 284–296, 2016.

[6] K. B. Povarova, V. A. Valitov, S. V. Obsepyan, A. A. Drozdov, O. A. Bazyleva, and E. V. Valitova, "Study of the properties and the choice of alloys for bladed disks (blisks) and a method for their joining," *Russian Metallurgy (Metally)*, vol. 2014, no. 9, pp. 733–741, 2014.

[7] F. Gao, L. Wang, Y. Liu, and J. Zhang, "Effects of long-term aging on fracture toughness of GH4586 alloy," *Heat Treatment of Metals*, vol. 35, no. 5, pp. 15–19, 2010.

[8] Y. P. Solntsev, M. M. Zamyatnin, A. A. Ezhov et al., "Evaluating the tendency toward brittle fracture of structural steels intended for use in large cross section parts," *Soviet Materials Science*, vol. 16, no. 5, pp. 428–429, 1981.

[9] Z. X. Shi and S. Z. Liu, "Study of impact rupture mechanism of a single crystal superalloy," *Foundry*, vol. 65, no. 3, pp. 276–283, 2016.

[10] A. Sukumaran, R. K. Gupta, and V. Anil Kumar, "Effect of heat treatment parameters on the microstructure and properties of Inconel-625 superalloy," *Journal of Materials Engineering and Performance*, vol. 26, no. 7, pp. 3048–3057, 2017.

[11] S. Q. Zhao and X. S. Xie, "Properties and microstructure after long term aging at different temperatures for a new nickel based superalloy," *Acta Metallrugica Sinica(China)*, vol. 39, no. 4, pp. 399–404, 2003.

[12] C. Gennari, L. Pezzato, E. Piva, R. Gobbo, and I. Calliari, "Influence of small amount and different morphology of secondary phases on impact toughness of UNS S32205 duplex stainless steel," *Materials Science and Engineering: A*, vol. 729, pp. 149–156, 2018.

[13] M. Wang, J. Du, Q. Deng, Z. Tian, and J. Zhu, "Effect of the precipitation of the η-Ni$_3$Al$_{0.5}$Nb$_{0.5}$ phase on the microstructure and mechanical properties of ATI 718Plus," *Journal of Alloys and Compounds*, vol. 701, pp. 635–644, 2017.

[14] H. Somekawa and T. Mukai, "High strength and fracture toughness balance on the extruded Mg-Ca-Zn alloy," *Materials Science and Engineering: A*, vol. 459, no. 1-2, pp. 366–370, 2007.

[15] S. Shanmugam, R. D. K. Misra, T. Mannering, D. Panda, and S. G. Jansto, "Impact toughness and microstructure relationship in niobium- and vanadium- microalloyed steels processed with varied cooling rates to similar yield strength," *Materials Science and Engineering: A*, vol. 437, no. 2, pp. 436–445, 2006.

[16] A. A. Kudrin, D. S. Zuev, L. L. Ponomareva, T. L. Baeva, and L. F. Dvoryashina, "Influence of microalloying on the plasticity of KhN58MBYuD-VI nickel alloy," *Steel in Translation*, vol. 38, no. 3, pp. 252–253, 2008.

[17] E. T. McDevitt, S. M. Oppenheimer, R. M. Kearsey, and J. Tsang, "Crack growth behavior in ATI 718Plus® alloy," *Materials Science Forum*, vol. 706-709, pp. 2428–2433, 2012.

[18] T. Cui, J. Y. Lv, L. Wang, H. C. Yang, and G. P. Zhao, "Effect of grain boundary carbide on impact ductility of superalloy GH586," *Journal of Iron Andsteel Research*, vol. 15, no. 7, pp. 24–28, 2003.

[19] L. Wang, S. Wang, X. Song, Y. Liu, and G. Xu, "Effects of precipitated phases on the crack propagation behaviour of a Ni-based superalloy," *International Journal of Fatigue*, vol. 62, no. 7, pp. 210–216, 2014.

[20] J. C. Zhao, V. Ravikumar, and A. M. Beltran, "Phase precipitation and phase stability in Nimonic 263," *Metallurgical and Materials Transactions A*, vol. 32, no. 6, pp. 1271–1282, 2001.

WILEY | Hindawi

Research Article

Residual Stress and Microstructure Characterization of 34CrMo4 Steel Modified by Shot Peening

Kejian Li [iD],[1] **Xu Wu,**[1] **Liping Chen,**[1] **Dengming Chen** [iD],[1] **Gungjun Zhu,**[1] **Qian Shen,**[2] **and Jae Hong Yoon**[1,3]

[1]*School of Metallurgy and Materials Engineering, Chongqing University of Science & Technology, Chongqing 401331, China*
[2]*College of Material Science and Engineering, Chongqing University of Technology, Chongqing 400054, China*
[3]*School of Nano & Advanced Materials Engineering, Changwon National University, Changwon 51140, Republic of Korea*

Correspondence should be addressed to Kejian Li; likejiann@gmail.com and Dengming Chen; cdming62@126.com

34CrMo4 steel is widely used for drill stem in oil exploration, because of its excellent properties, such as favorable hardenability, shock absorption, less tendency of temper brittleness, and eminent wear resistance. In this study, the main works are residual stress test and microstructure characterization of 34CrMo4 steel upon various shot peening treatments. The residual stress distribution with effect depth was studied upon the shot peening. Face-to-face paste sample preparation method is required for continuous observation for microstructure evolution of shot-peened specimen from the treat surface to matrix. Grain refinement, lath structure, and precipitates are clearly observed in the gradient deformation layer.

1. Introduction

34CrMo4 steel is one of the representative medium-carbon and low-alloy steels, due to its good balance of strength, toughness, and wear resistance in an extreme working environment. Hence, 34CrMo4 steel is widely used for drill stem in oil exploration, because of its excellent properties, such as favorable hardenability, shock absorption, less tendency of temper brittleness, and good corrosion resistance [1].

Surface treatment is widely used in increasing the performance of materials, such as elements coating to protect the material from severe environments [2]. The effect of hot deformation parameters such as temperature and strain rate on dynamic restoration processes of 34CrMo4 steel was studied in previous research [3].

Severe plastic deformation (SPD), such as shot peening [4, 5], is a generic term describing a group of metalworking techniques. It includes very large strains and typically involves a complex stress state or high shear, resulting in a high defect density and equiaxed ultrafine grain size (diameter less than 500 nm), even nanocrystalline structure (diameter less than 100 nm). The inference depth is about 200~600 μm after shot peening surface treatment. The microstructure will deform to include cracks, laths, lattice distortion, disordered structures, and deformation grains [6–8]. For the 34CrMo4 steel tools, after a long period of service, the purpose of this experiment is try to remove the rust and repair the 34CrMo4 steel tools by shot peening treatment. Shot peening is a well-known cold surface treatment that consists in bombarding the surface of the component with a stream of shots. As a result, the compressive residual stress and microstructure modification are induced within the near surface, which can improve the fatigue performance and surface properties of the material [9–11]. Therefore, the microstructure evolution analysis of the deformation layer from the top surface to matrix is very important.

Electron microscopy (EM) comprises a wide range of different methods that use various signals arising from the interaction of an electron beam with the sample to obtain information about the structure, morphology, and composition. Along with the development of materials science research on the basis of EM, scanning electron microscopy (SEM) and transmission electron microscopy (TEM) are widely used in the characterization of metals, ceramics,
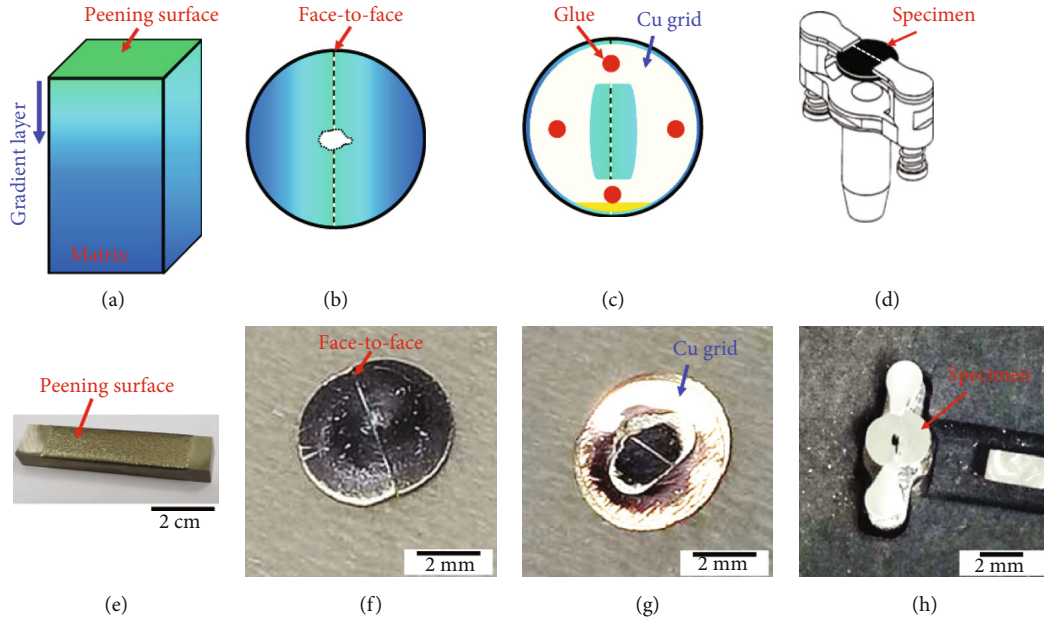
FIGURE 1: Topmost layer TEM sample preparation of (a–d) schematic diagrams and (e–h) corresponding real sample images. (a, e) Shot-peened specimen, face-to-face pasted sample of (b, f) specimen side and (c, g) Cu grid side, and (d) schematic diagram of TEM specimen in the ion milling holder and (h) final TEM specimen with a hole in the center.

powder, biology, and composites [12, 13]. With high-resolution electron microscopy (HREM) analysis technology, a resolution below 0.2 nm can reveal to us the essence of material at the atomic level. At the same time, ultra-high resolution microscopic analysis techniques for TEM sample preparation are becoming increasingly necessary to meet a higher quality. The traditional metallographic polishing, double ion milling, electrolytic polishing, and electrolytic jet are becoming increasingly unsuitable to meet the standards of scientific research methods [14, 15]. In recent years, because of the advent and development of focused ion beam (FIB) instruments, it is now possible to directly prepare specimens for the TEM from powder particles using the lift out method. The FIB sample preparation technique of thinning and processing is becoming more mature [16]. However, the excavation depth was limited to approximately 100 μm. The deeper matrix of 100 μm to several hundred micrometers cannot be prepared by FIB upon surface dig and take-off method.

Therefore, surface deformed layers urgently need microstructure characterization, especially on the topmost layer and several hundred micrometers in depth. The sample preparation was the most important part for microstructure study. Some preparation methods for cross-sectional TEM specimen are reported earlier [17, 18]. This study introduced a special sample preparation method—the face-to-face paste method—for the requirements of EM analysis. The feasibility was verified by those samples of the face-to-face paste method for EM observation.

2. Experimental Method

Figures 1(a)–1(d) show the schematic diagram of the topmost layer TEM sample preparation after shot peening. Diagrammatic drawing of the shot-peened specimen with a
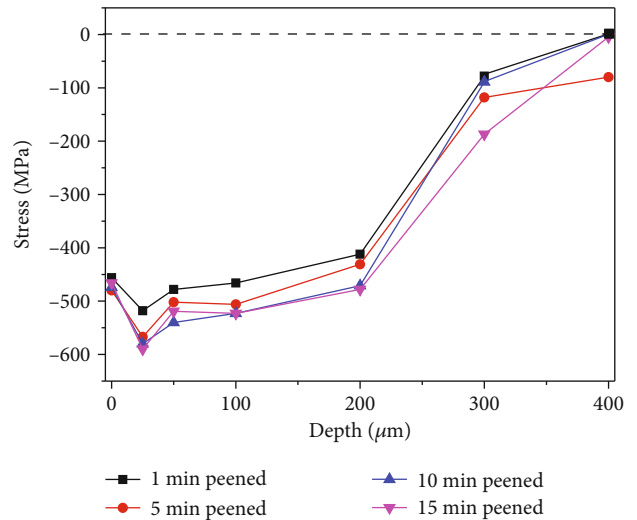
FIGURE 2: Residual stress analysis of 1~15 min shot-peened specimens.

gradient deformation layer is shown (Figure 1(a)). Owing to the fact that the diameter of TEM specimen is limited in 3 mm, the face-to-face paste method was implemented to piece together a circle with 3 mm diameter. A face-to-face paste method (Figure 1(b)) specimen side and (Figure 1(c)) Cu grid side were well required for electron microscope analysis. Final thinning was used by ion milling; the TEM specimen was fixed in the strut (Figure 1(d)), and finally the center will be thinned out. Corresponding real sample images are shown in Figures 1(e)–1(h).

The pasted glue was G1 glue bought from Gatan official website; detail steps of specimen preparation were through the following:
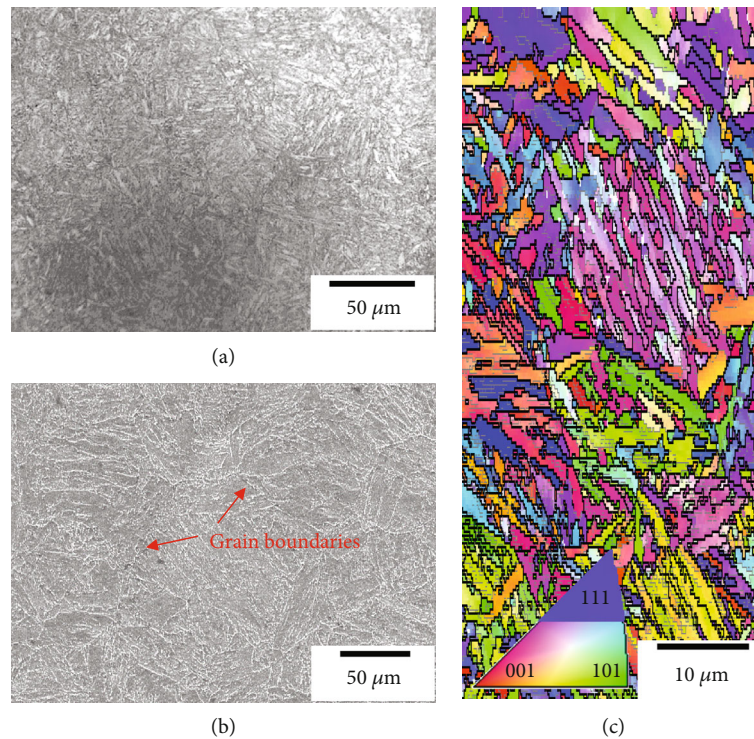
Figure 3: Microstructure characterization of 34CrMo4 Steel (a) OM, (b) SEM, and (c) EBSD mapping.

(i) Pour the epoxy liquid on the slide glass with the resin to have a harden ratio of 1 : 10

(ii) Use a toothpick to mix them

(iii) Paste it on a standard Cu TEM grid (Figures 1(c) and 1(g) and cure the resin at about 100°C during pasting

(iv) Fix the specimen on the milling holder as shown in Figure 1(d)

(v) Proceed with grinding, polishing, dimpling, and ion milling

(vi) Figure 1(h) shows the specimen after ion milling

At the final ion milling step, the energy was 3 kV and the milling angle was 4°.

The residual stress was measured by X-ray stress analyzer (LXRD, Proto, Canada) using $\sin2\psi$ method. The Cr Kα radiation with a wavelength $\lambda = 2.2897$ Å was used to determine ferrite (211) diffraction peak. Successive steps of material removal from the impacted surface to ~400 μm depth through electrochemical polishing were conducted in order to perform residual stress measurements in depth. The cross-sectional specimens for the electron back-scattered diffraction (EBSD) analysis were prepared via electrolytic polishing. The top treated surface specimens were thinned via polishing to 90 μm. EBSD specimens were electropolished (Struers TenuPol-5) at room temperature with an electrolyte of 10% perchloric and 90% acetic acid. EBSD measurements were performed with FESEM, JSM-7800F system installed in an oxford scan mode, with a beam step size of 400 nm.

The 34CrMo4 martensitic stainless steel was commercial, which is always used as a drill stem in oil exploration. The chemical composition was consistent with the nominal material element and mainly consisted of weight percent of 0.3-0.37 of C, 0.9-1.2 of Cr, 0.15-0.3 of Mo, 0.6-0.9 of Mn, ≤0.035 of S, ≤0.4 of Si, ≤0.025 of P, and balanced by Fe. Before the shot peening, the specimens are heat treated by quenching from 870°C and annealing in 560°C for 2 h. The description of the shot peening equipment has been reported elsewhere. Prior to the treatment, the plate surface was ground to 2000 grit with SiC metallographic paper. The shot peening processing was carried out for 1, 5, 10, and 15 min, and cast steel shots 0.6 mm in diameter. All thickness and depth in this study are not strictly accurate. It allows for an error of 5%.

3. Results and Discussion

Figure 2 shows the depth distributions of residual stress after shot peening. With increasing of shot peening intensities, the residual stress will increase from 1 to 5 min. However, it does not increase anymore during peening time from 5 to 15 min. They attain a peak value of -600 MPa at the depth of around 25 μm. The residual stresses return to zero as depth increases to around 400 μm. Therefore, a stronger processing is considered ineffective because of the residual stress of 34CrMo4 steel was considered saturated at 5 min peened.

Microstructure analysis of 1~15 min peened specimens was compared; the details and analysis method will be mainly exhibited by 5 min peened specimen. Figure 3 shows the
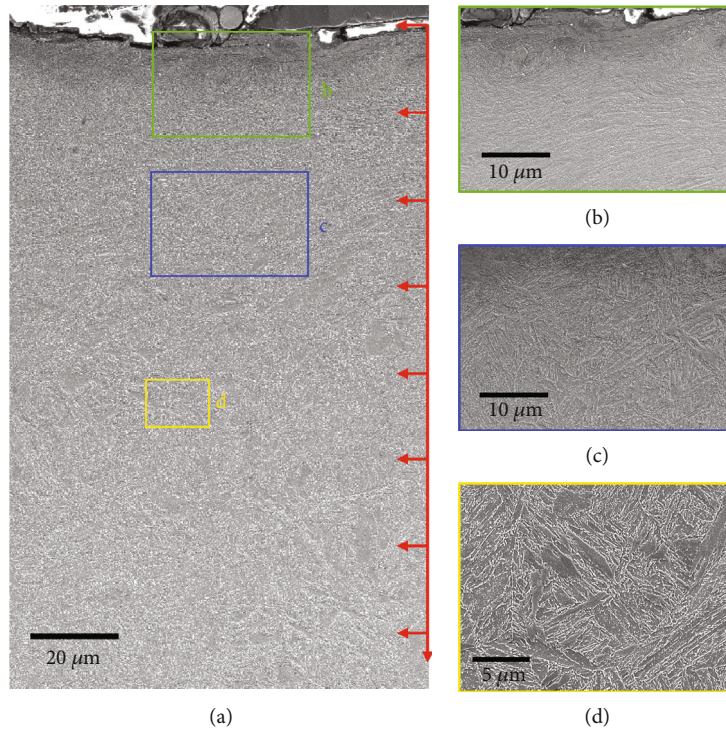
Figure 4: SEM images of the cross-sectional view of martensite steel after shot peening for 5 min (a) and high-magnification images of (b–d) corresponding region marked in (a).

microstructure of 34CrMo4 steel matrix: optical microscope (OM) in a wide range view (Figure 3(a)). SEM image shows large grain boundaries, and grain size is ~30 μm (Figure 3(b)). EBSD inverse pole figure mapping shows the lath structures of martensitic steel (Figure 3(c)). The microstructure of the specimen was a typically tempered martensite, with a relatively homogeneous ferrite grain structure.

Figure 4 shows SEM images of the 34CrMo4 martensite steel after shot peening for 5 min: cross-sectional view (Figure 4(a)), high magnification images of the deformed structure in the top layer (Figure 4(b)), the gradients structure (Figure 4(c)), and matrix of the steel (Figure 4(d)). The effect depth of deformed structure was 100 μm; grain refinement and deformation were the main features in the layer.

Figure 5 shows the EBSD analysis of image quality (IQ) image (Figure 5(a)), inverse pole figure (IPF) (Figure 5(b)), and phase mapping (Figure 5(c)). The residual stress was rich in the deformation layer after shot peening, which has influenced the EBSD recognition rate. The colors in Figure 5(b) represent different orientations as shown by the standard triangle (inset in Figure 5(b)). The presence of all colors at similar frequencies indicates that the shot-peened specimens fail to exhibit a strong texture. Phase mapping shows that the main phase was α'-martensite in body-centered cube (BCC) and bits of austenite and Fe_3C precipitate. As an additional strategy, the precipitated phase must be Fe_3C from the study of iron-carbon phase diagram [19].

Figure 6 is TEM characterization of the topmost layer on the deformed layers. At the topmost layer (Figure 6(a)), the nanosized grains were obvious by high-density dislocation entanglement, which corresponds to the SADP showing a ring pattern taken on this area. At the depth of 50 μm (Figure 6(b)), high-density nanothickness lath structure was obvious. Some dislocation cell and new grain boundaries are visible in the 100 μm depth region, as shown in Figure 6(c). In the 200 μm depth region (Figure 6(d)), the dislocation and subgrains had sharp boundaries. At the 400 μm depth (Figure 6(e)), original grains are seen the same as in the matrix (Figure 6(f)) typically tempered martensite. The microstructural evolution from original grains to nanograins was apparent in the TEM analysis by the decreasing of depth.

Figure 7 shows the TEM analysis of precipitates; the TEM sample preparation is by carbon extraction replica technology [20]. High-magnification TEM images in Figure 7(b), iFFT image (Figure 7(c)), measurement of the distance of atom plans (Figures 7(d) and 7(e)), and index of electron diffraction pattern (Figure 7(f)) form the yellow square in Figure 7(b). Compared to standard PCPDF, card # 030411 [21] was well matched.

Figure 8 shows the TEM and high-resolution TEM (HRTEM) analysis of the TEM analysis of the martensite steel after shot peening: TEM image on the topmost layer (Figure 8(a)) and HRTEM images (Figure 8(b)) taken in the red dotted box in Figure 8(a). In the software of digital micrograph, selected squares marked in Figure 8(b) can get the fast Fourier transformation (FFT) image see in Figure 8(c). Apply mask and then get inverse FFT image in Figures 8(d)–8(f) measurement of the distance of atom plans. Compared to standard PCPDF, card # 882324 [22] was well
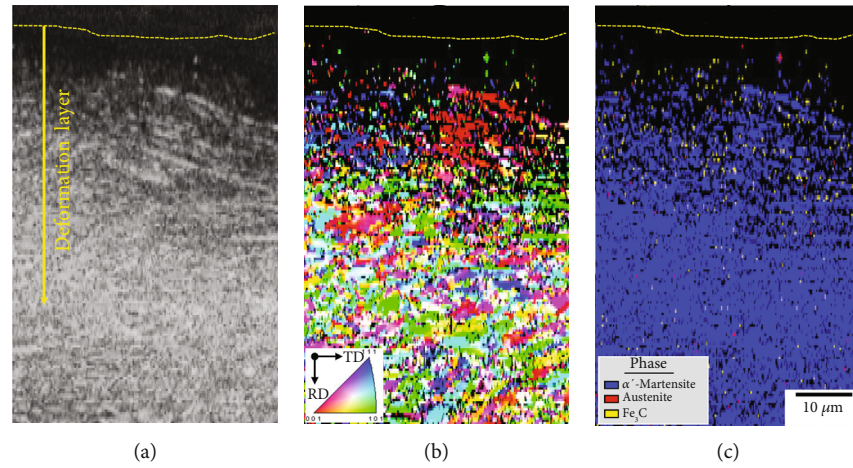
FIGURE 5: EBSD images of the cross-sectional view of martensite steel after shot peening for 5 min: (a) image quality, (b) inverse pole figure, and (c) phase mapping.
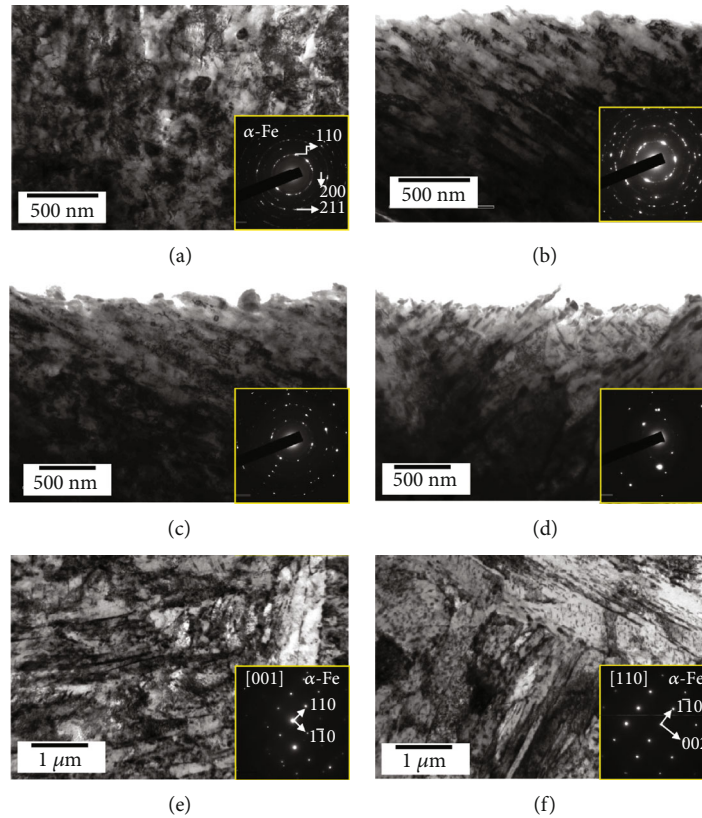
FIGURE 6: TEM analysis of the 34CrMo4 martensite steel after shot peening for 5 min: (a) topmost layer, (b) 50 μm depth, (c) 100 μm depth, (d) 200 μm depth, (e) 400 μm depth form top surface, and (f) matrix before shot peening. Corresponding SADPs are inside.

matched. The lattice of FCC, space group of Fm$\bar{3}$m(225), $a = 0.343$ nm, $d_{111} = 0.1980$ nm, $d_{200} = 0.1715$ nm, and $d = 0.3952$ nm were twice as the distance of the d_{111}, and zone axis was [0,1,1] in Figure 8(g). The FCC crystal was discovered in the topmost layer of martensite steel (BCC) after shot peening. In the phase mapping by EBSD (Figure 5(c)), FCC crystal was identified in red color near the topmost layer.

Phase transformation from FCC to BCC was reported in the study of 301 austenite stainless steel upon ultrasonic shot peening in preliminary [5]. The reverse phase transformation from BCC to FCC was discovered in this study. However, the dynamic phase transformation between FCC and BCC upon severe plastic deformation needs substantial evidence in further research.

(a)

(b)

(c)

(d)

(e)

Zone axis: [1,1,0]

(f)
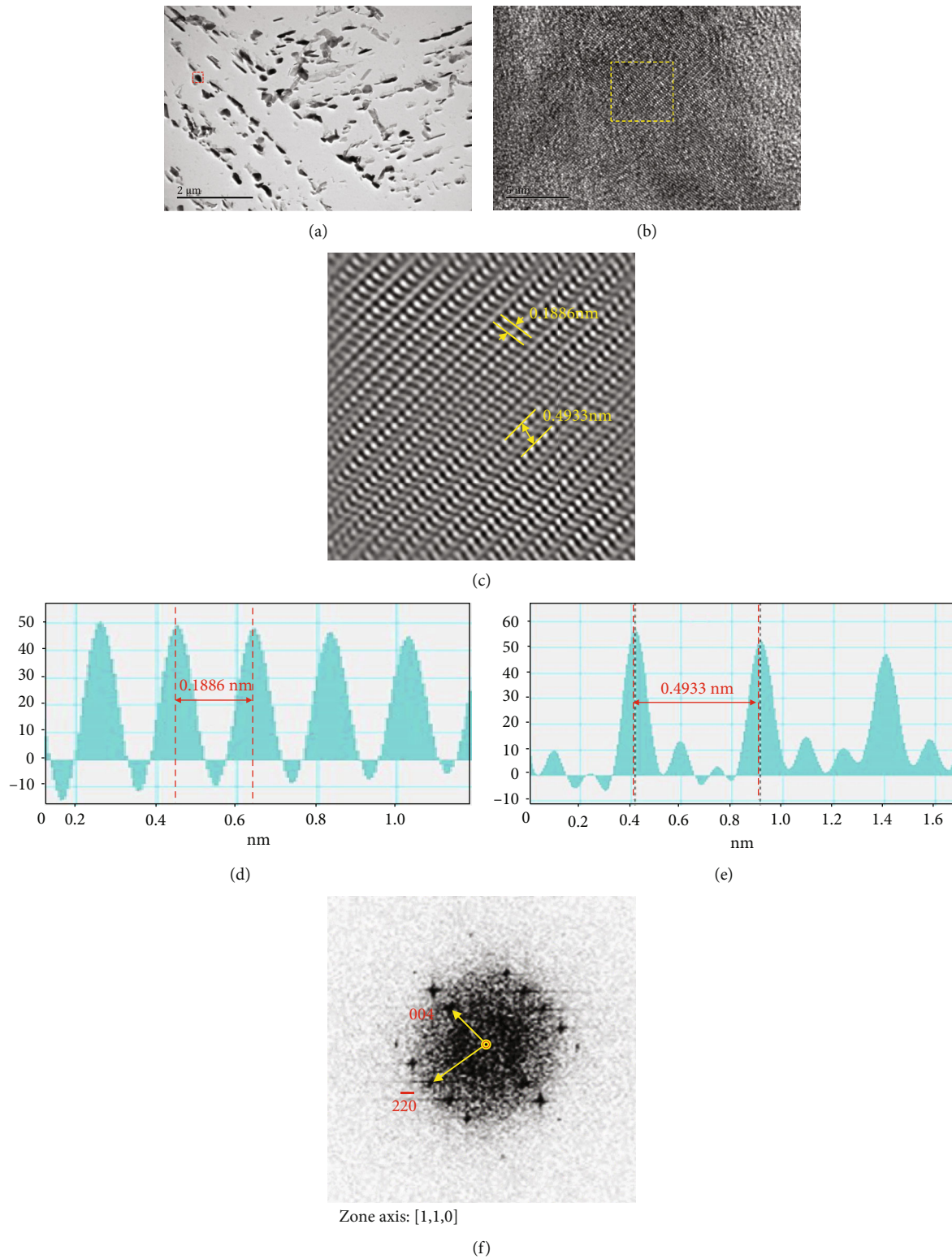
Figure 7: TEM analysis of the martensite steel: (a) TEM image on precipitates, (b) high-magnification TEM images, (c) iFFT image, (d, e) measurement of the distance of atom plans, and (f) index of electron diffraction pattern form the yellow square in (b).
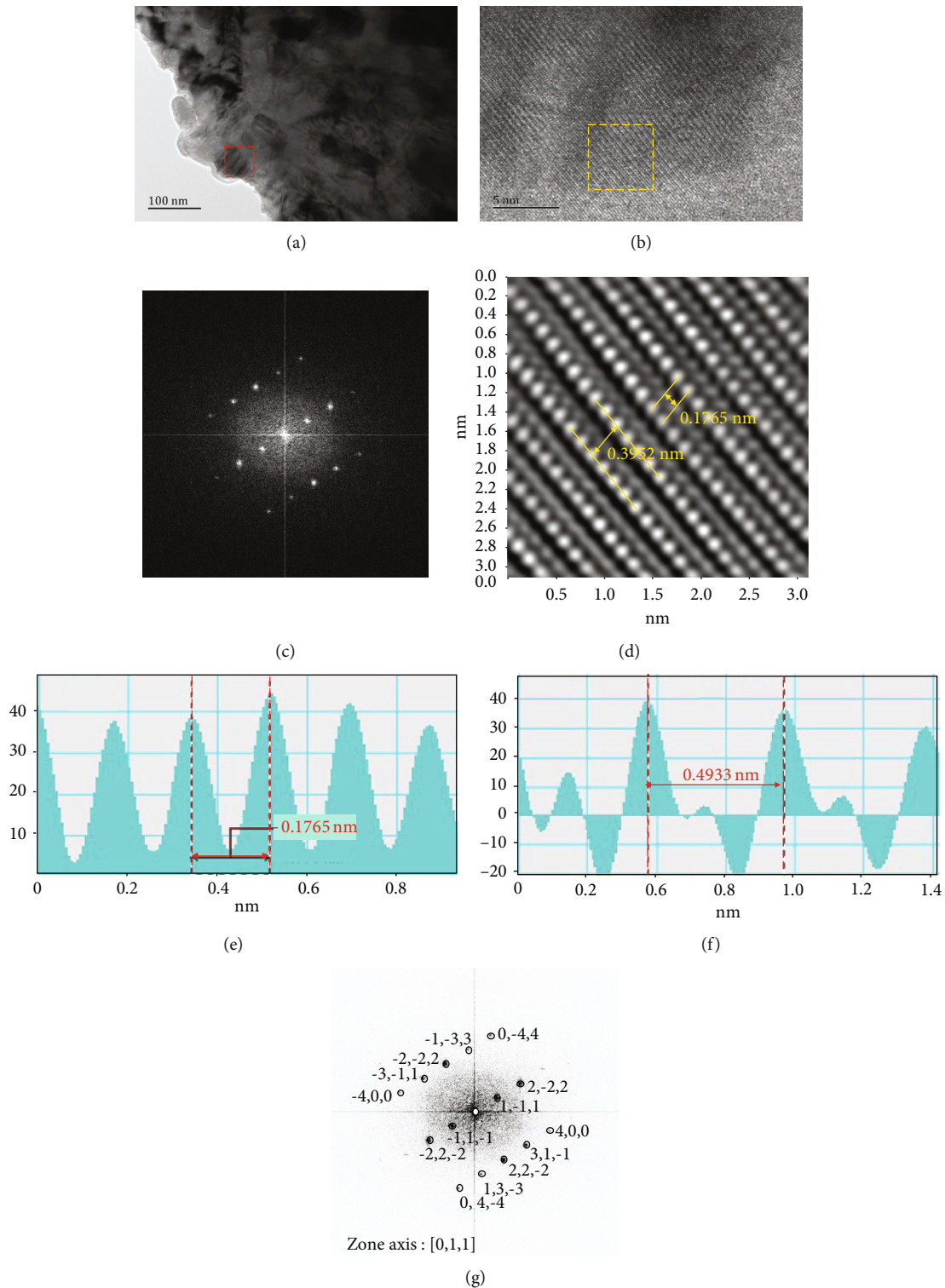
FIGURE 8: TEM analysis of the martensite steel after shot peening: (a) TEM image on the topmost layer, (b) high-magnification TEM images, (c) FFT and (d) iFFT images, (e) and (f) measurement of the distance of atom plans, and (g) index of electron diffraction pattern in (c).

4. Summary and Conclusion

The main works are residual stress test and microstructure characterization of 34CrMo4 steel upon various shot peening treatments. Following are the findings:

(1) The residual stress distribution with effect depth was found increasing upon the shot peening. The residual stress of 5 min shot-peened specimen was saturated. The maximum compressive stress value is -600 MPa at the depth of 25 μm

(2) Microstructure evolution characterization was analyzed by various electron microscope technologies. Nanograins were observed on the top most peening layer. In nanothickness lath structure and nanosized grains, precipitates were in gradient deformation layer. Grain refinement was clearly observed in the gradient deformation layer

(3) The FCC crystal was discovered in the topmost layer of BCC after shot peening. The dynamic phase transformation between FCC and BCC upon shot peening needs substantial evidence in further research

Data Availability

No data were used to support this study.

Conflicts of Interest

The authors declare that they have no conflicts of interest.

Acknowledgments

References

[1] Q. Zheng, K. Li, X. Yin et al., "Corrosion Properties of 34CrMo4 Steel Modified by Shot Peening," *Scanning*, vol. 2017, Article ID 1928198, 8 pages, 2017.

[2] M. Donald, "Mattox. Chapter 1 - introduction," in *Handbook of Physical Vapor Deposition (PVD) Processing (Second Edition)*, D. M. Mattox, Ed., pp. 1–24, William Andrew Publishing, Boston, 2010.

[3] S. V. S. Far, M. Ketabchi, and M. R. Nourani, "Hot deformation characteristics of 34CrMo4 steel," *Journal of Iron and Steel Research International*, vol. 17, no. 12, pp. 65–69, 2010.

[4] H. W. Huang, Z. B. Wang, J. Lu, and K. Lu, "Fatigue behaviors of AISI 316L stainless steel with a gradient nanostructured surface layer," *Acta Materialia*, vol. 87, Supplement C, pp. 150–160, 2015.

[5] K. Li, K. Shin, and P. Cao, "Strain-induced phase transformation and nanocrystallization of 301 metastable stainless steel upon ultrasonic shot peening," *Metallurgical and Materials Transactions A*, vol. 49, no. 10, pp. 4435–4440, 2018.

[6] Y. Pi, J. Faure, G. Agoda-Tandjawa et al., "Microstructural characterization of Ti-6Al-4V alloy subjected to the duplex SMAT/plasma nitriding," *Microscopy Research and Technique*, vol. 76, no. 9, pp. 897–903, 2013.

[7] K. Li, D. Chen, P. Cao, X. Cao, and K. Shin, "Effect of plastic deformation on microstructure and properties of 347 austenite steel," *Journal of Nanoscience and Nanotechnology*, vol. 19, no. 7, pp. 4078–4082, 2019.

[8] K. Li, G. Spartacus, J. Dong, P. Cao, and K. Shin, "Effect of ultrasonic shot peening on microstructure and properties of 301SS," *Materials and Manufacturing Processes*, vol. 32, no. 16, pp. 1851–1855, 2017.

[9] P. Fu, C. Jiang, Z. Zhang, and V. Ji, "Residual stress and microstructure of GCr15 steel after multistep shot peening," *Surface Engineering*, vol. 30, no. 11, pp. 847–851, 2014.

[10] M. Chen, H. Liu, L. Wang et al., "Evaluation of the residual stress and microstructure character in SAF 2507 duplex stainless steel after multiple shot peening process," *Surface and Coatings Technology*, vol. 344, pp. 132–140, 2018.

[11] L. Rongbin, X. Wang, S. Hailong, and Z. Yong, "Effect of composite shot peening on residual stress and microstructure of S30432 steel," *Material & Heat Treatment*, vol. 41, no. 4, pp. 148–152, 2012.

[12] D. A. Muller, "Structure and bonding at the atomic scale by scanning transmission electron microscopy," *Nature Materials*, vol. 8, no. 4, pp. 263–270, 2009.

[13] I. Sulima, S. Boczkal, and L. Jaworska, "SEM and TEM characterization of microstructure of stainless steel composites reinforced with TiB$_2$," *Materials Characterization*, vol. 118, pp. 560–569, 2016.

[14] F. Phillipp, R. Höschen, M. Osaki, G. Möbus, and M. Rühle, "New high-voltage atomic resolution microscope approaching 1 Å point resolution installed in Stuttgart," *Ultramicroscopy*, vol. 56, no. 1-3, pp. 1–10, 1994.

[15] K. W. Urban, C.-L. Jia, L. Houben, M. Lentzen, S.-B. Mi, and K. Tillmann, "Negative spherical aberration ultrahigh-resolution imaging in corrected transmission electron microscopy," *Philosophical Transactions of the Royal Society A: Mathematical, Physical and Engineering Sciences*, vol. 367, no. 1903, pp. 3735–3753, 2009.

[16] K. Dawson and G. J. Tatlock, "Preparation of micro-foils for TEM/STEM analysis from metallic powders," *Micron*, vol. 74, pp. 54–58, 2015.

[17] H.-J. Klaar and F.-Y. Hsu, "A new preparation method for cross-sectional TEM specimens," *Materials Characterization*, vol. 36, no. 4-5, pp. 365–369, 1996.

[18] K. Li, Y. He, H. Ma et al., "Surface nanocrystallization of pure Ni induced by ultrasonic shot peening," *Science of Advanced Materials*, vol. 9, no. 2, pp. 188–192, 2017.

[19] H. K. D. H. Bhadeshia and S. R. Honeycombe, *Steels (Third Edition)*, pp. 39–70, Elsevier Ltd., 2006.

[20] K. Li, Y. He, H. Ma et al., "Grain growth and precipitation in nanostructured 304SS after heat treatment," *Journal of Nanoscience and Nanotechnology*, vol. 17, no. 10, pp. 7436–7441, 2017.

[21] W. Eitel, *Zeitschrift für Kristallographie, Kristallgeometrie, Kristallphysik, Kristallchemie*, vol. 72, Akademische Verlagsgesellschaft Athenaion, 1929.

[22] J. Häglund, A. Fernández Guillermet, G. Grimvall, and M. Körling, "Theory of bonding in transition-metal carbides and nitrides," *Physical Review B: Condensed Matter*, vol. 48, no. 16, pp. 11685–11691, 1993.

Research Article

Effect of Different Isothermal Time on Microstructure and Mechanical Property of the Low-Carbon Steel Treated by Dual-Stable C-Mn Partitioning Process

Cainian Jing [ID], Xiaoyun Ding [ID], Daomin Ye, Jingrui Zhao [ID], Tao Lin, and Shubo Xu

School of Materials Science and Engineering, Shandong Jianzhu University, Jinan 250101, China

Correspondence should be addressed to Cainian Jing; jcn@sdjzu.edu.cn and Jingrui Zhao; zhaojingrui19@sdjzu.edu.cn

The stability of retained austenite was improved by the dual-stable C-Mn partitioning process. The phase transformation and element diffusion of dual-stable C-Mn partitioning process of tested steel were investigated by means of EPMA, SEM, OM, tensile testing machine, and other analysis methods. The effects of the first and second austenite stabilization time on the microstructure and mechanical properties of low-C-Si-Mn steel were studied, respectively. The enrichment of C and Mn elements is obvious after the dual-stable C-Mn partitioning process, and the microstructure of the tested steel is constituted of martensite, ferrite, and retained austenite. Compared with the conventional Q&P steel, the tensile strength of the steel treated by the dual-stable C-Mn partitioning process is slightly lower, but the plasticity is improved significantly. The tensile strength is 875-910 MPa, the elongation is 20-24%, and the product of strength and elongation can reach 21 GPa·%.

1. Introduction

In recent years, with the continuous development of the automotive industry, resources and environmental issues have become increasingly prominent, which puts higher demands on the energy efficiency of automobiles. Automobile lightweight is an inevitable trend in the development of the automotive industry, and the application of high-strength steel is an effective technical mean for lightweight vehicles [1]. In 2003, Speer et al. [2] of the US State School of Mines proposed the Q&P (Quenching & Partitioning) process and established a thermodynamic model to study the problem of the C element partitioning of the experimental steel between the temperature of M_s and M_f. In the following ten years, the third generation of high-strength steel represented by Q&P steel and medium manganese steel were rapidly developed [3, 4]. The room temperature microstructure of Q&P steel is martensite and retained austenite [5, 6]. Martensite as matrix ensures high strength, and the TRIP (Transformation Induced Plasticity) effect of retained austenite makes Q&P steel have good plasticity [7]. Studies have shown that the regulation of retained austenite is an

extremely important factor among many factors affecting the mechanical properties of high-strength steel [5, 8]. The tested steel is heated to the two-phase zone for heat preservation, and the coordination of elements such as Mn and Cu can increase the stability of austenite to a certain extent, and at the same time, a part of ferrite can be introduced to further improve the plasticity to obtain the comprehensive mechanics of the experimental steel [9, 10].

The dual-stable C-Mn partitioning process is to improve the stability of austenite by two austenite stabilization processes. First, annealing in the two-phase region promotes the partitioning of C and Mn elements from ferrite to austenite [11], that is, the high-temperature austenite stabilization process; the second process is the use of low-temperature carbon distribution similar to the traditional "one-step" Q&P process. During the second process, after annealing in the two-phase region, the experimental steel is quenched to a temperature between M_s and M_f to maintain the C element partitioning from martensite to austenite [12]. In this study, the low-carbon-silicon-manganese steel was selected as the raw material. The low-carbon steel distribution effect was improved by two austenite stabilization processes, and the

TABLE 1: Main chemical composition of sample steel (wt. %).

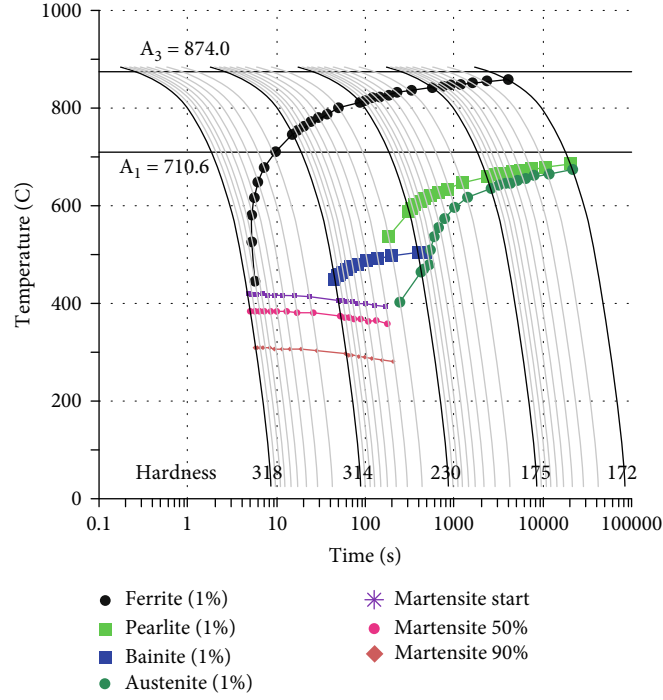| Element	C	Mn	Si	Al	Cr	Ti	S	P	B
Content	0.11	1.50	1.16	0.043	0.024	0.01	0.001	0.008	0.003

FIGURE 1: The CCT diagram of tested steel.

problem of low-residual austenite amount and poor plasticity after quenching was solved. The effect of different austenite stabilization time on the microstructure and mechanical properties of the tested steel was studied.

2. Experimental Materials and Methods

The material used in the test was a cold-rolled low-carbon-silicon-manganese steel having a thickness of 1.5 mm, and a standard tensile specimen having a gauge length of 25 mm was prepared by wire cutting according to the ASTM E8 standard. The initial structure of the tested steel consists of ferrite and pearlite. The main chemical composition thereof is shown in Table 1. The phase transition point of the tested steel was calculated by the empirical formula and JMatPro 7.0 software: 710°C for the austenite transformation starting temperature (A_{c1}), 874°C for the austenite transformation end temperature (A_{c3}), and 410°C for the martensite transformation starting temperature (M_s). Figure 1 is the CCT diagram of tested steel. The traditional Q&P process and dual-stable C-Mn partitioning process are applied to the experimental steel to study the influence of process parameters on microstructure and mechanical properties.

Figure 2 illustrates the Q&P process and the dual-stable C-Mn partitioning process. The heating process was carried out in the vacuum heat treatment furnace. The dual-stable C-Mn partitioning process was to rapidly heat the tested steel

at 10°C/min to the two-phase region of ferrite and austenite at 820°C for 3 min, 5 min, 7 min, and 9 min, respectively, for the first austenite stabilization process. Then, the tested steel was quenched to 240°C, holding for 10 sec, 20 sec, 30 sec, 40 sec, and 50 sec, respectively, for the second stabilization process of austenite. Finally, the sample steel was quenched with water to room temperature. As the control group, the experimental steel was kept at 930°C for 5 min to make sure the completion of austenitic transformation, then quenched to 240°C for carbon distribution, and finally quenched to room temperature with water.

3. Results and Analysis

3.1. Effect of Dual-Stable C-Mn Partitioning Process on Microstructure of Tested Steel

3.1.1. Effect of Dual-Stable C-Mn Partitioning Process on Elemental Partitioning Behavior. Electron microprobe analysis (EPMA) was performed on the tested steel after the dual-stable C-Mn partitioning process and the traditional Q&P process, respectively. Figure 3 shows the distribution of C and Mn elements in the tested steel after treatment of the traditional Q&P process. Figure 4 shows the distribution of C and Mn elements after the dual-stable C-Mn partitioning process. Comparing Figures 3 and 4, C and Mn elements are obviously enriched between the lath of martensite in both the two processes. However, the enrichment of the elements
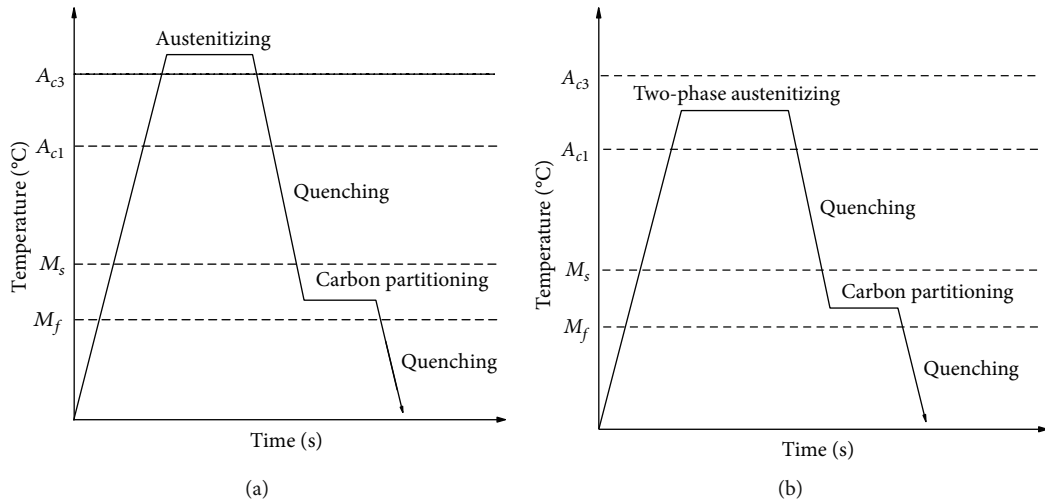
FIGURE 2: Schematic of heat treatment: (a) Q&P process and (b) dual-stable C-Mn partitioning process.
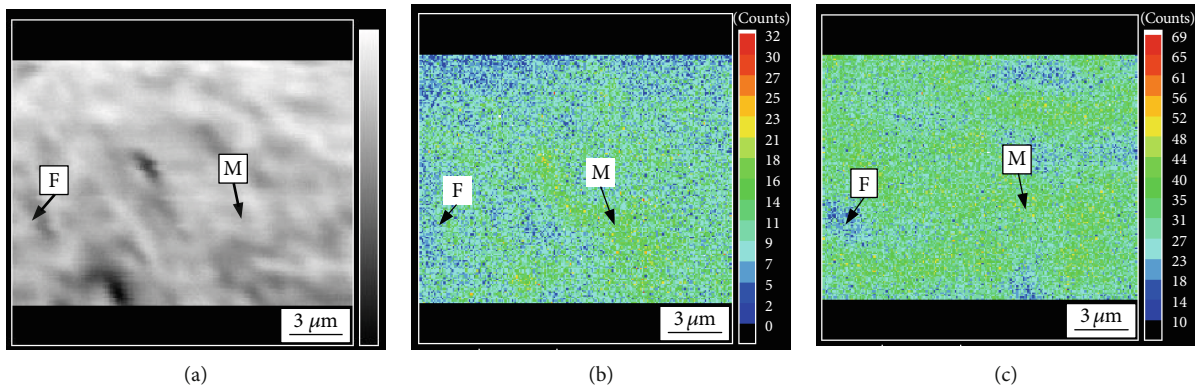
FIGURE 3: (a) The microstructure image, the EPMA images of (b) C, and (c) Mn element distribution of tested steel after Q&P process.
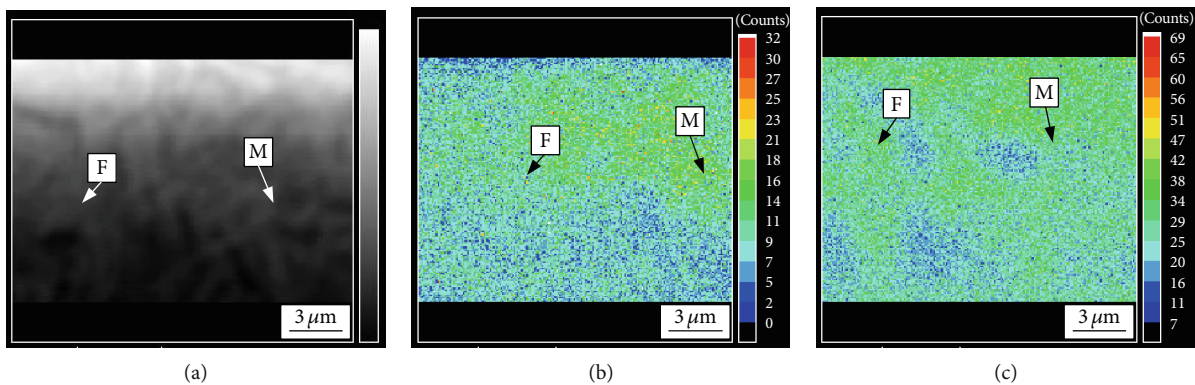
FIGURE 4: (a) The microstructure image, the EPMA images of (b) C, and (c) Mn element distribution of tested steel at 820°C for 5 min and then at 240°C for 30 s.

in the dual-stable C-Mn partitioning process is more obvious. It can be seen from Figures 3 and 4 that the distribution position of C element is basically consistent with that of Mn element. The reason is that the distribution process of Mn element causes the originally distributed Mn atoms to migrate and generate after obtaining sufficient diffusion activation energy. Because the radius of Mn atom is slightly larger than that of iron atom and much larger than that of carbon atom, the migration of Mn causes lattice distortion. As an interstitial atom, C atom is more easily retained in the lattice gap caused by the migration of Mn atoms, resulting in the accumulation of more C atoms near the Mn atoms and the phenomenon of the same distribution position of Mn and C. In this process, the Mn content of

(a)

(b)

(c)

(d)
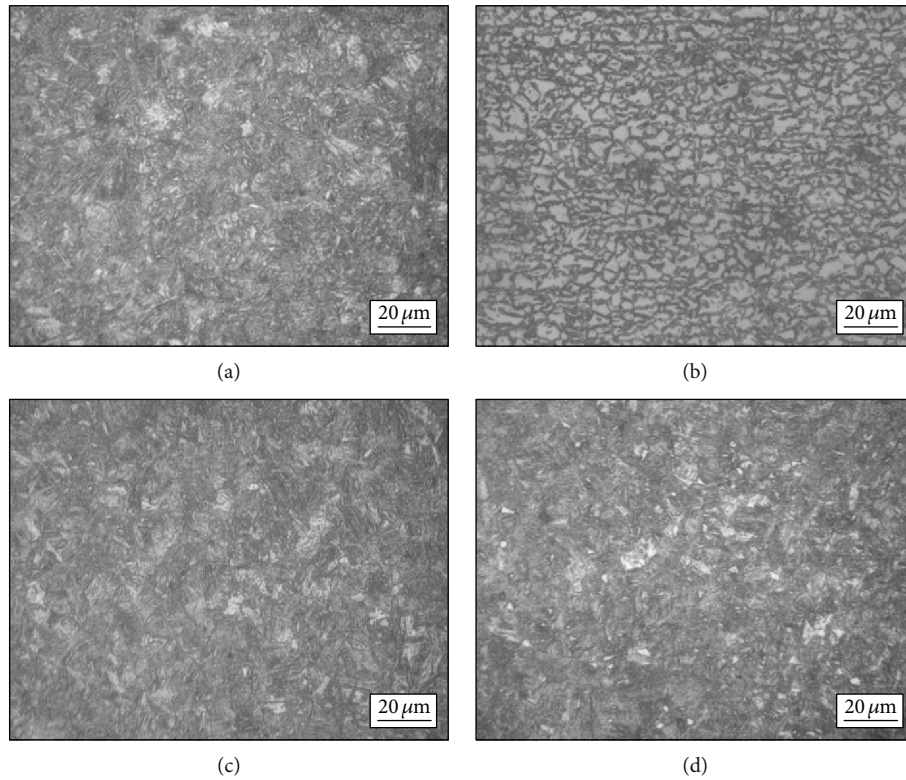
Figure 5: The OM micrographs of the first austenite stabilization for (a) 3 min, (b) 5 min, (c) 7 min, and (d) 9 min.

austenite also decreased gradually. In this process, the martensite transformed from austenite after quenching retains the distribution characteristics of Mn elements in austenite, i.e., the Mn content in the central region is higher than that in the surrounding area [13]. The C element partition after quenching between M_s and M_f can stabilize the retention of more retained austenite to room temperature [14]. Compared with the traditional Q&P process, the dual-stable C-Mn partitioning process improves the austenite stability by the two austenite stabilization processes of C, Mn elemental partitioning at high temperature, and C elemental partitioning at low temperature. The tested steel has both sufficient strength and excellent plasticity so that it has good comprehensive mechanical properties.

3.1.2. Effect of the First Austenite Stabilization Time on Microstructure.

The effect of the first austenite stabilization time on the microstructure of the tested steel during the dual-stable C-Mn partitioning process was investigated. The metallographic structures of the tested steel at 820°C for different austenite stabilization time (3, 5, 7, and 9 min) then at 240°C for 30 s are shown in Figure 5. The metallographic structure of the tested steel is a composite structure of lath martensite and ferrite. With the extension of the first austenite stabilization time, the ferrite volume fraction first increases and then decreases, and the morphology also changes. The volume fraction of ferrite in the tested steel annealing at 820°C for 3 min is low. When the annealing time increases to 5 min, the ferrite is mainly in bulk shape and the volume fraction of ferrite increases, which may be due to the
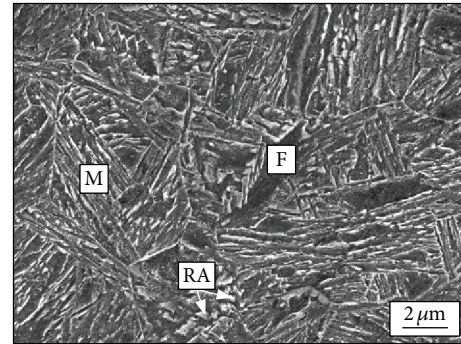
Figure 6: The SEM micrographs of tested steel of dual-stable C-Mn partitioning process test.

partial growth of ferrite grains with the increase of the first austenite stabilization time [15]. As the austenite stabilization time continues to prolong, the austenite interface gradually grows into the ferrite and the nearby ferrite is annexed, which results in a decrease in the ferrite volume fraction in the microstructure at room temperature. Figure 6 is an SEM image of the dual-stable C-Mn partitioning process annealed at 820°C for 5 min. The microstructure of the tested steel is austenite, ferrite, and a small amount of retained austenite. The martensite is lath-like, and the slats of the martensite group have different beam positions.

3.1.3. Effect of the Second Austenite Stabilization Time on Microstructure.

In order to explore the influence of the

(a)

(b)

(c)

(d)

(e)
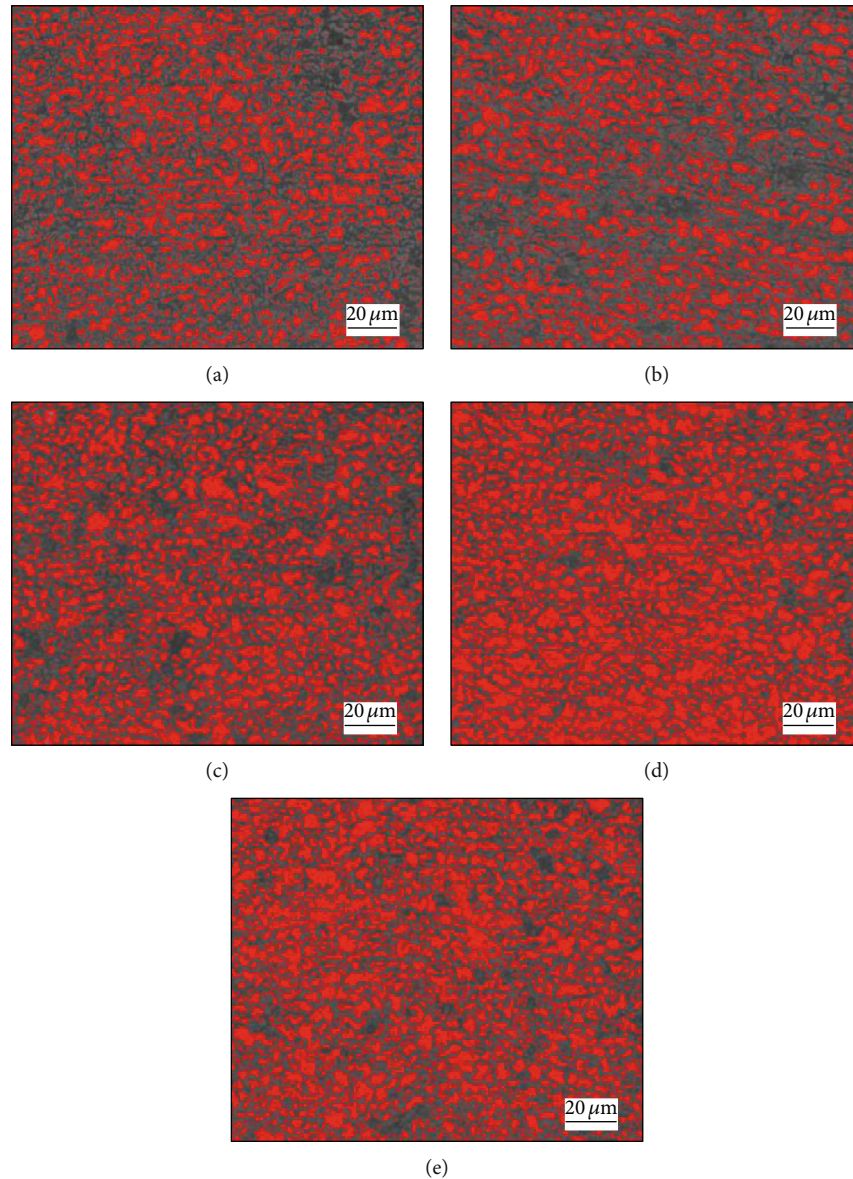
Figure 7: The morphology of martensite and ferrite (red) after partitioning for (a) 10 sec, (b) 20 sec, (c) 30 sec, (d) 40 sec, and (e) 50 sec.

Table 2: The fractions of ferrite for 10~50 sec.

Time (s)	10	20	30	40	50
Fraction (%)	46	36	49	62	56

second austenite stabilization time on the tested steel structure, the tested steel was quenched to 240°C (between the temperature of M_s and M_f) and kept in this temperature for 10-60 sec after 5 min of first austenite stabilization process. Figure 7 shows the metallographic structure of the experimental steel for different second austenite stabilization time, where the red parts represent ferrite. We calculated the fractions of ferrite by the Photoshop CC software, and the results are shown in Table 2. It was found that the microstructure of the dual-stable C-Mn partitioning steel consists of martens-

ite, ferrite, and retained austenite from the SEM analysis. It can be seen from Figure 7 that a granular or flake-like ferrite structure is uniformly and distributed scatteredly in the lath martensite gap. When the second austenite stabilization time is 10 sec, the amount of martensite is relatively high and decreases gradually with the time prolonging. By analyzing the SEM photograph of the tested steel, it is known that the residual austenite is distributed in a film form at the boundary between the interlaced lath martensite and the bulk ferrite due to the low carbon content of the sample steel. When the steel plate is subjected to external force, the strip martensite of the plate provides high strength to resist the deformation of the steel plate. The TRIP effect of retained austenite impacted by external force induces martensite and retards necking, and the external impact work is absorbed with the relatively soft ferrite. The uniform distribution of

Mn
Fe
C
Austenite
Ferrite
Grain boundary

FIGURE 8: The schematic representation of the first austenite stabilization process.

FIGURE 9: The schematic representation of the dual-stable C-Mn partitioning process.

the three phases makes the steel possess the comprehensive mechanical property of high strength and high plasticity.

3.2. Analysis of Phase Transition Process of Dual-Stable C-Mn Partitioning Process. According to the EPMA image of the microstructure and element distribution of the dual-stable C-Mn partitioning process, the hypothesis of the phas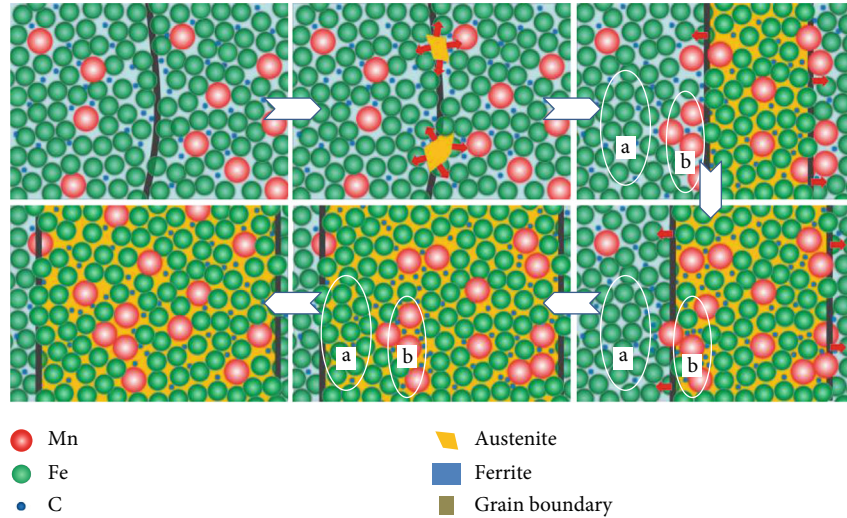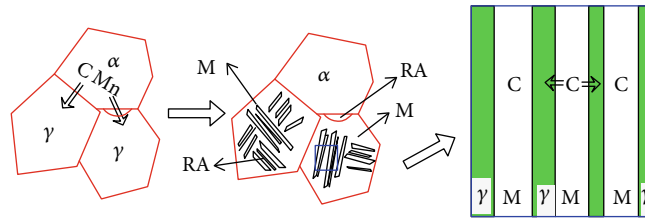e transformation process is proposed, and the first austenite stabilization process is analyzed in combination with Figure 8. The solid solubility of C and Mn in ferrite is low. When the first austenite stabilization process is maintained, the austenite begins to nucleate after reaching the phase transition point. The diffusion of C element from ferrite to austenite is completed first [16]. The diffusion rate of Mn element is higher in ferrite than in austenite. Mn undergoes short-range diffusion after obtaining activation energy. It migrates from ferrite to ferrite/austenite boundary and aggregates there. The Mn element is distributed at the ferrite/austenite interface, and its diffusion rate in the ferrite is much higher than that in the austenite, resulting in a difference in the concentration of Mn elements at the two sides of the interface. With the diffusion of Mn element, Mn-rich region b and Mn-depleted region a were formed at the grain boundary and central region of ferrite, respectively. The Mn content in the grain boundary is relatively high, and the austenite grains are small right now. Although this process is accompanied by the migration of austenite grain boundaries to ferrite, the grain boundary growth is not obvious since Mn has the effect of

stabilizing austenite and inhibiting grain growth. With the increase of the first austenite stabilization time, the Mn atoms originally gathered at the boundary gradually migrate into the austenite, and the grain boundaries migrate to the ferrite side. As the Mn-poor ferrite area is gradually "engulfed" by the grain boundaries, the austenite grows gradually, and the content of Mn element in the transformed austenite gradually decreases. After quenching, martensite retains the distribution characteristics of Mn in austenite, and the Mn content in the central region is higher than that in the surrounding area. As the first austenite stabilization time increases, the grain size of austenite and ferrite changes, and the C and Mn elements uniformly diffuse in the austenite. With the increase of time, Mn element diffuses from the interface to the austenite grain. At the austenite grain boundary, the content of Mn is continuously decreasing, and the grain growth resistance decreases. As the grain grows, the internal average Mn content is decreased, and the first austenite stabilization effect is reduced. When the time further increases, the growth of austenite grain is dominant, the austenite grains become larger, the residual retained austenite content gradually decreases after quenching, and the martensite lath spacing becomes wider, which deteriorates the mechanical properties of the tested steel. Therefore, the first austenite stabilization time has an essential influence on the microstructure and mechanical properties of the tested steel.

A schematic diagram of the dual-stable C-Mn partitioning process is analyzed in conjunction with Figure 9. When
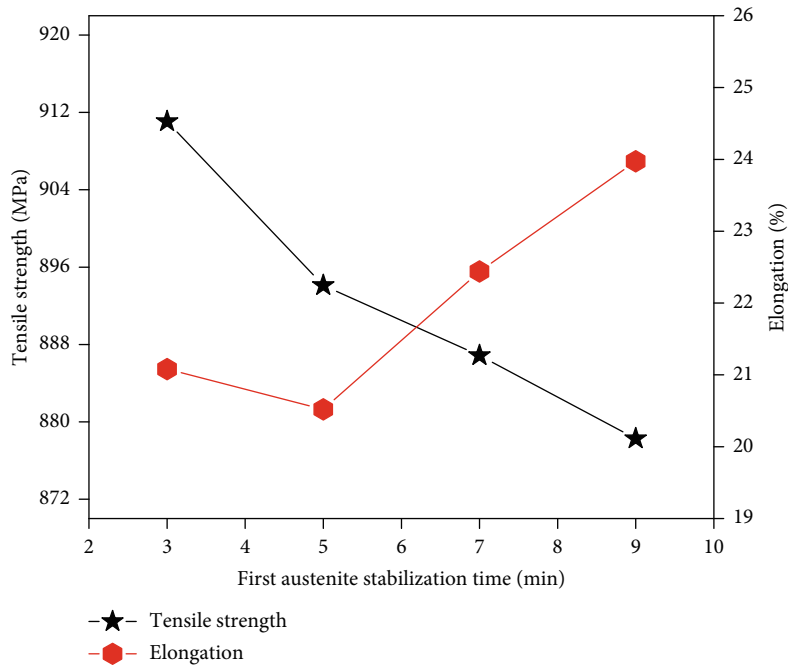
(a)
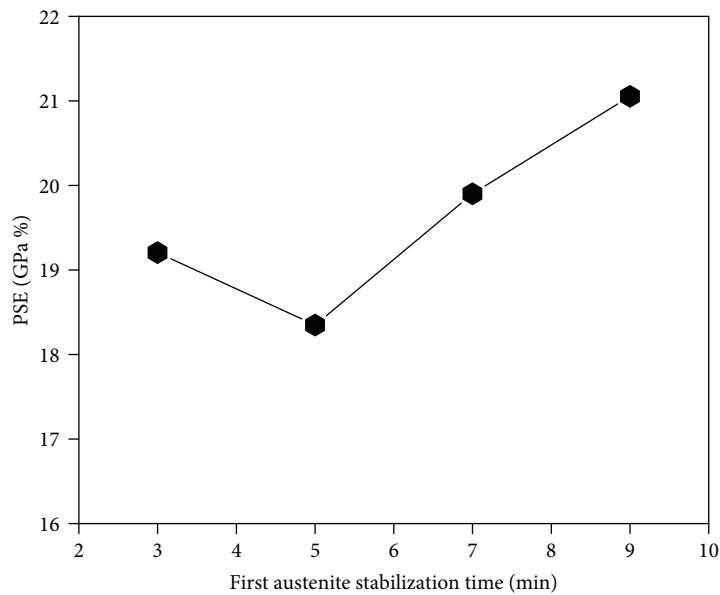
(b)

Figure 10: Mechanical properties of these steels after first austenite stabilization for 3 min, 5 min, 7 min, and 9 min: (a) strength and elongation and (b) product of strength and elongation.

the tested steel is heated to the temperature above the starting transformation temperature of austenite at a suitable heating rate and maintained, C and Mn elements are enriched in austenite, increasing the high-temperature stability of austenite [17]. After the first quenching, a composite structure of martensite, ferrite, and retained austenite is obtained [18]. The saturated solid solubility of C and Mn in ferrite is extremely low, and the first quenching temperature is 240°C. Therefore, the influence of C and Mn diffusion in ferrite can be ignored [19]. In the carbon distribution process, i.e., the second austenite stabilization

process for the tested steel, similar to the traditional one-step Q&P process, C element diffuses from martensitic lath to the adjacent thin film austenite or sheet austenite, increasing the stability of austenite at room temperature [20]. At the same time, part of the ferrite increases the grain boundary density and prolongs the time of the dynamic equilibrium of the C element. The optimal second austenite stabilization time is extended to suppress the precipitation of carbides in this process. Finally, more retained austenite is obtained at room temperature, thereby improving the overall mechanical properties.

3.3. Influence of Dual-Stable C-Mn Partitioning Process on Mechanical Properties

3.3.1. Effect of the First Austenite Stabilization Time on Mechanical Properties.
In the first austenite stabilization process, the stability of austenite is increased by the distribution of C and Mn elements, which has an effect on the mechanical properties. The tested steel was incubated at an austempering temperature of 820°C for 3-9 min and then subjected to the same dual-stable C-Mn partitioning process. The tensile strength and elongation at break of the tested steel change with the first austenite stabilization time, as shown in Figure 10(a). The change of the product of strength and elongation with the first austenite stabilization is shown in Figure 10(b). With the increase of the first austenite stabilization holding time, the tensile strength gradually decreases, while the elongation after breaking first decreases and then increases and reaches a minimum value at 5 min. The change rule of the product of strength and elongation is basically the same as that of elongation after fracture. The product of strength and elongation of the tested steel showed a minimum at 5 min, and the comprehensive mechanical properties were relatively poor. After the dual-stable C-Mn partitioning process, the tensile strength of the tested steel is between 875 MPa and 910 MPa, and the elongation after fracture is up to 24%. The product of strength and elongation is between 18.3-21 GPa·%. Under the dual-stable C-Mn partitioning process, the mechanical properties may be changed. The tested steel is insulated in the two-phase zone, and the austenite gradually grows. When holding for 3 minutes, the austenite and ferrite grains are fine, which can be observed from the microstructure observation. According to the Holpeci formula, the tested steel has a good match of strength and plasticity due to the effect of fine-grain strengthening. With the prolonged holding time, the grain growth has a major influence on the mechanical properties of the tested steel [21]. In the range of 5-7 min, the nucleation rate of austenite increases, and the volume fraction of ferrite decreases. The first austenite stabilization is sufficient, and the C and Mn elements diffuse into the high-solubility austenite, which increases the high-temperature stability of austenite. In addition, the Mn element has an effect of hindering the growth of crystal grains, so that the grain boundary growth rate is relatively reduced after the austenite/ferrite interface is rich in Mn [22, 23]. More retained austenite is obtained during the dual-stable C-Mn partitioning process, which increases the elongation of the tested steel after fracture. However, the ferrite content continues to increase, resulting in a slight decrease in the tensile strength of the experimental steel. At 5-9 min, the distribution of C and Mn elements in the stabilization process of austenite has a major influence on the mechanical properties.

3.3.2. Effect of Dual-Stable C-Mn Partitioning Process Time on Mechanical Properties.
In order to study the influence of the dual-stable C-Mn partitioning process time on the mechanical properties, after the first austenite stabilization

of the tested steel is completed, it is quenched to 240°C and kept for 10-50 sec. The traditional Q&P process is carried out, that is, the tested steel is kept at 930°C for 5 min, then quenched to 240°C and kept for 10-50 sec. Figure 11(a) shows the change of tensile strength and elongation with time in two processes. The tensile strength of dual-stable C-Mn partitioning process steel is lower than that of traditional Q&P process steel, and the elongation after fracture is obviously higher than Q&P process steel. The microstructure of the dual-stable C-Mn partitioning process steel is martensite, ferrite, and retained austenite. The ferrite produced by the first austenite stabilization process is a soft phase, and the volume fraction of the primary martensite of the tested steel is low [12, 23]. At the same time, during the first stabilization of the tested steel, C and Mn elements diffused from ferrite to austenite, the stability of austenite is increased, and finally, more retained austenite is obtained. In addition, the martensite formed first occurs self-tempering at the time of partition, and its plasticity is improved.

The tested steel under the Q&P process is kept at 930°C for 5 min, completely austenitized, and the C and Mn elements are evenly distributed in the austenite. The stability of austenite can only be enhanced by the C element at low temperature. During the partitioning process, carbon diffuses from martensite to untransformed austenite. Due to the low partition temperature, the carbon content of most untransformed austenite is less than the minimum carbon content required for no phase transition when cooling to room temperature. This is also the reason why the comprehensive mechanical properties of the double-stabilized C-Mn partitioning process are better than that of the traditional Q&P steel. The difference between the two products of strength and elongation is also less than 3.7GPa·%. The product of strength and elongation changes with time in the two processes. It can be seen from Figure 10(b) that after the dual-stable C-Mn partitioning process time is 30 sec, the product of strength and elongation of the dual-stable C-Mn partitioning process steel continues to increase with the increase of the holding time. The max product of strength and elongation is 20.42GPa·% after partitioning for 50 s. And the product of strength and elongation of traditional Q&P steel decreased sharply after the distribution time exceeded 30 s. This is due to the dynamic competition between the partitioning of C from martensite to retained austenite and the diffusion of C in austenite [12, 24]. At the same time, if the partitioning time is too long, some carbides will form, which will deteriorate the properties of steel. On the other hand, more austenite is retained in the partitioning of carbon and manganese. More austenite further enhances the product of strength and elongation. After the partitioning time exceeds 30 s, the product of strength and elongation begins to decrease. The reason for the decrease of the product of strength and elongation is the interface migration from martensite to austenite. The fine ferrite in the microstructure of the dual-stable C-Mn process steel increases the grain boundary density, hinders the diffusion of C element, and prolongs the time of C element dynamic balance. Macroscopically, the peak value of the product of strength and elongation is delayed.

(a)

(b)
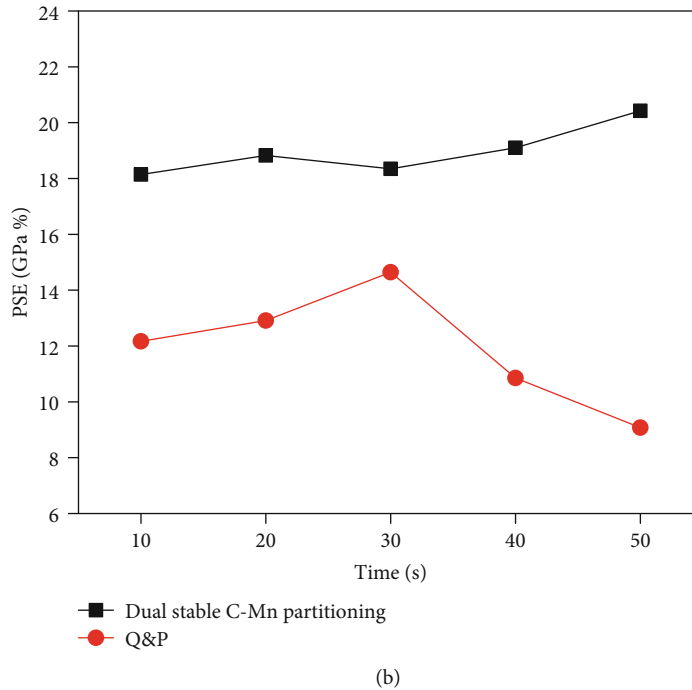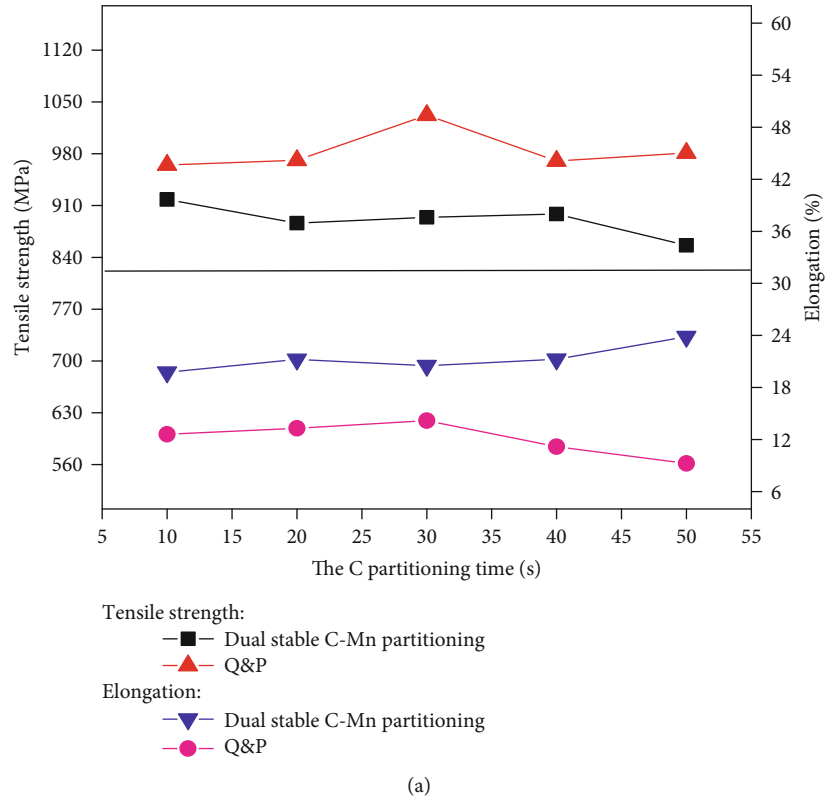
FIGURE 11: Mechanical properties of these steels after the dual-stable C-Mn partitioning process and Q&P process for 10 sec, 20 sec, 30 sec, 40 sec, and 50 sec: (a) strength and elongation and (b) product of strength and elongation.

4. Conclusion

(1) The microstructure of the tested steel after the dual-stable C-Mn partitioning process is a multiphase structure of martensite, ferrite, and retained austenite. The martensite is lath-like shape, and the ferrite is flake-like shape. In this process, the C and Mn elements are enriched in austenite, and the stability of austenite is increased

(2) With the increase of the first austenite stabilization time, the grain size of ferrite increases and the grain shape gradually changes from granular to flake, and

the volume fraction increases; the tensile strength decreases gradually, and the elongation after fracture decreases first and then increases. The change rule of the product of strength and elongation is consistent with that of the elongation after fracture

(3) As the second austenite stabilization time increases, the martensite volume fraction gradually decreases. After the second austenite stabilization time of 30 sec, the product of strength and elongation of the dual-stable C-Mn partitioning process steel continued to increase, while that of the traditional Q&P steel decreases, showing a delay of the peak value of the product of strength and elongation. Compared with traditional Q&P steel, the tensile strength of steel under the dual-stable C-Mn partitioning process is slightly lower, but the plasticity is obviously improved. The tensile strength is 875-910 MPa, the elongation after fracture is 20-24%, and the product of strength and elongation can reach 21 GPa. %.

Data Availability

The all data used to support the findings of this study are included within the article.

Conflicts of Interest

The authors declare that there is no conflict of interest regarding the publication of this paper.

Acknowledgments

References

[1] Y. M. Tu and C. N. Jing, "Research status and development trend of high strength quenching and partitioning steel," *Heat Treatment of Metals*, vol. 9, pp. 132–137, 2017.

[2] J. Speer, D. K. Matlock, B. C. De Cooman, and J. G. Schroth, "Carbon partitioning into austenite after martensite transformation," *Acta Materialia*, vol. 51, no. 9, pp. 2611–2622, 2003.

[3] B. Hu, H. Luo, F. Yang, and H. Dong, "Recent progress in medium-Mn steels made with new designing strategies, a review," *Journal of Materials Science & Technology*, vol. 33, no. 12, pp. 1457–1464, 2017.

[4] H. Li, J. Y. Chen, X. G. Duan, and H. T. Jiang, "Stability and TRIP effect of retained austenite of medium manganese Q&P steel," *Materials Review*, vol. 4, pp. 611–615, 2018.

[5] E. J. Seo, L. Cho, Y. Estrin, and B. C. de Cooman, "Microstructure-mechanical properties relationships for quenching and partitioning (Q&P) processed steel," *Acta Materialia*, vol. 113, pp. 124–139, 2016.

[6] M. J. Santofimia, L. Zhao, R. Petrov, and J. Sietsma, "Characterization of the microstructure obtained by the quenching and partitioning process in a low-carbon steel," *Materials Characterization*, vol. 59, no. 12, pp. 1758–1764, 2008.

[7] M. K. El-Fawkhry, M. Eissa, A. Fathy, and T. Mattar, "Development of maraging steel with retained austenite in martensite matrix," *Materials Today: Proceedings*, vol. 2, pp. S711–S714, 2015.

[8] X. C. Xiong, B. Chen, M. X. Huang, J. F. Wang, and L. Wang, "The effect of morphology on the stability of retained austenite in a quenched and partitioned steel," *Scripta Materialia*, vol. 68, no. 5, pp. 321–324, 2013.

[9] Y. Q. Tian, H. J. Zhang, L. S. Chen, J. Song, Y. Xu, and S. Zhang, "Effect of alloy elements partitioning behavior on retained austenite and mechanical property in low carbon high strength steel," *Acta Metallurgica Sinica*, vol. 5, pp. 531–539, 2014.

[10] Z. Q. Ren, Y. Q. Tian, R. Li et al., "Microstructure and properties of low carbon silicon manganese steel treated by Mn pre-partitioning I&Q&P process," *Heat Treatment of Metals*, vol. 9, pp. 132–137, 2017.

[11] Y. L. Wei, R. Li, J. Y. Song, H. J. Zhang, Y. Q. Tian, and L. S. Chen, "Study on microstructure evolution of dual phase region and thermodynamics of C, Mn partitioning of low carbon Si-Mn steel," *Hot Working Technology*, vol. 16, pp. 154–156, 2016.

[12] S. Kim, J. Lee, F. Barlat, and M. G. Lee, "Transformation kinetics and density models of quenching and partitioning (Q&P) steels," *Acta Materialia*, vol. 109, pp. 394–404, 2016.

[13] C. Song, H. Yu, L. Li, T. Zhou, J. Lu, and X. Liu, "The stability of retained austenite at different locations during straining of I&Q&P steel," *Materials Science and Engineering: A*, vol. 670, pp. 326–334, 2016.

[14] J. Y. Song, H. J. Zhang, Y. L. Wei, Y. Q. Tian, and L. S. Chen, "Mn partitioning behavior of low carbon Si-Mn steel during I & P & Q process," *Heat Treatment of Metals*, vol. 41, no. 4, pp. 110–114, 2016.

[15] M. J. Santofimia, T. Nguyen, L. Zhao, R. Petrov, I. Sabirov, and J. Sietsma, "New low carbon Q&P steels containing film-like intercritical ferrite," *Materials Science and Engineering: A*, vol. 527, no. 23, pp. 6429–6439, 2010.

[16] L. S. Chen, J. Y. Zhang, Y. Q. Tian, J. Y. Song, Y. Xu, and S. H. Zhang, "Effect of pretreated microstructure on the morphology and mechanical properties of low-carbon steel with IQ&P treatment," *Journal of University of Science and Technology Beijing*, vol. 38, no. 2, pp. 223–229, 2016.

[17] F. Yang, H. W. Luo, and H. Dong, "Effects of intercritical annealing temperature on the tensile behavior of cold rolled 7Mn steel and the constitutive modeling," *Acta Metallurgica Sinica*, vol. 6, pp. 859–867, 2018.

[18] C. Song, H. Yu, J. Lu, T. Zhou, and S. Yang, "Stress partitioning among ferrite, martensite and retained austenite of a TRIP-assisted multiphase steel: an in-situ high-energy X-ray diffraction study," *Materials Science and Engineering: A*, vol. 726, pp. 1–9, 2018.

[19] Z. P. Qin, H. H. Wang, Z. Tong, F. Hu, L. Li, and K. M. Wu, "Influence of lamellarizing process on microstructure and properties of low carbon low alloy high-strength steel," *Transactions of Materials and Heat Treatment*, vol. 9, pp. 142–147, 2017.

[20] A. Arlazarov, M. Ollat, J. P. Masse, and M. Bouzat, "Influence of partitioning on mechanical behavior of Q&P steels," *Materials Science and Engineering: A*, vol. 661, pp. 79–86, 2016.

[21] L. S. Chen, J. Y. Zhang, Y. Q. Tian, J. Y. Song, and X. Y. Qi, "Study on morphology feature and mechanism in transformation

process of austenite during intercritical annealing of low-carbon steel," *Hot Working Technology*, vol. 16, pp. 223–226, 2015.

[22] Z. Y. Liu, Z. G. Yang, Z. D. Li, Z. Liu, and C. Zhang, "Simulation of ledgewise growth kinetics of proeutectiod ferrite under interfacial reaction-diffusion mixed control model," *Acta Metallurgica Sinica*, vol. 4, pp. 390–395, 2010.

[23] H. C. Li, S. Y. Chen, and X. D. Yue, "Effect of Mn on growth of proeutectoid ferrite in low-carton steel," *Hot Working Technology*, vol. 6, pp. 23–25, 2014.

[24] A. K. Behera and G. B. Olson, "Nonequilibrium thermodynamic modeling of carbon partitioning in quench and partition (Q&P) steel," *Scripta Materialia*, vol. 147, pp. 6–10, 2018.

WILEY | Hindawi

Research Article

Precipitation Behavior of the Topologically Close-Packed Phase in the DD5 Superalloy during Long-Term Aging

Guiqun Liu [ID],[1] Xiaoli Zhang [ID],[1] Xinyi Wang,[2] and Yanxin Qiao [ID][2]

[1]*College of Material Science and Engineering, North Minzu University, Yinchuan 750021, China*
[2]*School of Materials Science and Engineering, Jiangsu University of Science and Technology, Zhenjiang 212003, China*

Correspondence should be addressed to Xiaoli Zhang; xlzhang@alum.imr.ac.cn and Yanxin Qiao; yxqiao@just.edu.cn

The precipitation behaviors of the topologically close-packed (TCP) phases in the bicrystal DD5 superalloy have been investigated. The results showed that the [001] crystallographic orientations are consistent with that of adjacent grains; however, the direction of the needle-like TCP phases is not consistent with that of the γ phase channels. The angle between needle-like TCP phases and γ phase channels is $45°$, but the angle between the needle-like TCP phases of the adjacent grains is equal to the misorientation of the adjacent grains. Furthermore, during long-term aging, the needle-like TCP phases gradually decompose and transform into globular and short rod-like phases. The TCP phases precipitate preferentially in the dendrite. It is difficult to precipitate at the interdendrite/grain boundary, which is caused by the segregation of the constituent elements of the TCP phase to the dendrite.

1. Introduction

Superalloy is a kind of high-alloying iron-based, nickel-based, or cobalt-based metal material, which can withstand large complex stress above 600°C and has certain surface stability [1]. Nickel-based single-crystal superalloys have been widely used as jet engines and industrial gas turbine blades. In order to continuously improve its high temperature creep resistance, more and more refractory elements have been added to the superalloy. Presently, the known refractory elements such as Cr, Mo, W, and Re are good creep-strengthening elements. In particular, Re is recognized as the alloy element with outstanding strengthening effect. However, the addition of excessive refractory elements will significantly reduce the stability of the alloy structure.

The addition of excessive alloy elements such as Cr, Mo, W, and Re to the superalloy will cause the precipitation of intermetallic phases which have complex crystal structures rich in these refractory elements during long-term heat exposure or service. Because of their special dense structures, these phases are generally referred to as the topologically close-packed (TCP) phase [2]. The TCP phases of Ni-based single-crystal superalloys are σ, μ, P, and R [3, 4]. It is gener-ally accepted that the TCP phase will deteriorate the creep properties of the alloy. So how to avoid the precipitation of the TCP phase is an important aspect of alloy design. Only by knowing more about the precipitation rules and characteristics of the TCP phase, we can avoid the precipitation of the TCP phase reasonably and effectively, so as to better optimize the design of the alloy.

Frank and Kasper [5, 6] first investigated the crystal structure characteristics of TCP phases and characterized the TCP phase by coordination polyhedron. These so-called Kasper polyhedrons have equilateral triangle surfaces and four atomic coordination numbers of 12, 14, 15, and 16, but in practice, polyhedron surfaces often deviate from equilateral triangles [2]. The structure of the TCP phase is composed of pentagonal or hexagonal antiprism arranged side by side. The antiprism can usually be regarded as some simple structural units, and using these structural units to characterize the structure of the TCP phase will greatly simplify the process of analysis [7–9].

In the past few decades, the precipitation behavior of the μ phase has been extensively studied [10–15]. Many structural defects have been found in the μ phase in some superalloys or intermetallic compounds, such as stacking

Table 1: The chemical compositions of the DD5 superalloy (wt%).

Cr	Co	Mo	W	Al	Ta	Re	Hf	C	Ni
7.15	7.8	1.5	5.05	6.3	6.6	3	0.15	0.022	Bal.

faults, twin bands, microtwins, and second-phase symbiosis [11–13, 16–18]. However, there is little work on the detailed precipitation behavior of the P phase and R phase [3, 18–21].

In this paper, the TCP phase in the second-generation Ni-based superalloy DD5 is studied and the precipitation and evolution of the TCP phase are found and summarized. It provides evidence for further understanding the precipitation behavior and characteristics of the TCP phase in Ni-based single-crystal superalloys.

2. Materials and Methods

A second-generation single-crystal DD5 superalloy was used in this work. The chemical composition of the DD5 superalloy is listed in Table 1. The DD5 superalloy was produced by directional solidification and seeding so as to eliminate the effects of the grain boundary and crystallographic orientation on the TCP phase. In order to assure the directions of dendritic growth and thermal gradient to be accordant, the [001] direction of two seeds was aligned to the growth direction. The misorientation of the [010]/[100] direction of two seeds was about 20°. Since the [001] direction of the seed is parallel to the primary dendrites of the seed and the [010]/[100] direction of the seed is parallel to the secondary dendrites of the seed, the primary dendrites of two seeds are parallel to each other and parallel to the sample axis. The angle between the secondary dendrite arms of two seeds is about 20°. The dimension of the specimen was in size of $10 \times 10 \times 300$ mm.

A Bridgman high-rate solidification (HRS) furnace [22, 23], modified with two hot zones (upper zone and lower zone), was used in this study. The ceramic model was mounted on the water-cooled copper chill plate. The temperatures of the upper zone and lower zone were 1480°C and 1580°C, respectively. The master alloy ingot was heated to 1580°C and kept at the temperature for 5 min. Subsequently, the molten alloy was poured into the preheated mold. To ensure the system to attain a thermal equilibrium, casting samples were directionally solidified after 10 min of the pouring and pulled down in a withdrawal speed of 6 mm/min. When the temperature of the casting samples dropped to room temperature, the ceramic shell was broken and the bicrystal DD5 samples were taken out.

To determine the location of the grain boundary of the bicrystal DD5, all samples were macroetched with a mixture of HCl and H_2O_2 (volume ratio 5 : 1). Subsequently, the misorientation of the bicrystal DD5 superalloy was examined by the Electron Back Scattered Diffraction (EBSD) technique in a Scanning Electron Microscope (SEM). After microetching in a mixture of 100 ml HCl, 100 ml H_2O, 5 ml H_2SO_4, and 2 g $CuSO_4$, the dendrite structure was observed using an optical microscope (OM). Finally, the TCP phase was observed by a SEM. The angle of γ (needle-like TCP)
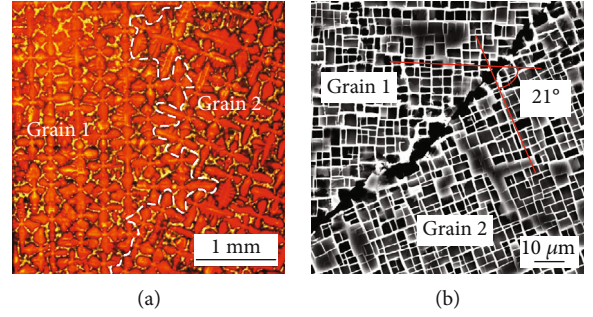

Figure 1: (a) Metallographic micrograph of as-cast bicrystal specimen and (b) SEM micrograph of the microstructure after standard heat treatment.

phases between two grains was measured by the analysis software of Image-Pro Plus.

To study the element segregation of as-cast DD5, the concentrations of each chemical element in dendrite and interdendrite were measured three times by the Electron Probe Micro Analyzer (EPMA). Then, the average value of the three measurements was taken. The segregation ratio was the average concentration of every element at dendrite divided by that at interdendrite.

The vacuum heat treatment of the bicrystal DD5 was as follows: 1310°C/2 h, air cooling; 1130°C/4 h, air cooling; and 900°C/16 h, air cooling. The long-term aging was 950°C for 100 h, 500 h, 1000 h, and 2000 h.

3. Results and Discussions

The cross-sectional microstructure of as-cast bicrystal DD5 is shown in Figure 1(a). It is the typical dendritic structure of the <001> direction in grains 1 and 2, and the "white phase" of the interdendritic region is γ/γ' eutectic. The white dotted line between the two grains is the grain boundary. The angle between the secondary dendritic arms of both sides against the grain boundary is about 21°.

The cross-sectional microstructure of as-cast DD5 after vacuum heat treatment is shown in Figure 1(b). In grains 1 and 2, the white channel is the γ phase and the black cube phase is the γ' phase. The γ/γ' eutectic at the grain boundary has completely disappeared, and the irregular block-like black γ' phases appear. It is worth noting that the direction of the white γ phase in each grain is consistent with that of the secondary dendrite arm in Figure 1(a), and the angle between the two grains is about 21°. In other words, under the condition that the [001] crystallographic orientation of the adjacent grains is the same, the angle between the phase channels of the adjacent grains is consistent with that between the secondary dendritic arms of the adjacent grains.

The precise misorientation of the two grains in Figure 1 is shown in Figure 2. The precise misorientation of the two grains is 21°. This is in good agreement with the conclusion obtained from Figure 1. When the [001] crystallographic orientation of the adjacent grains is the same, the misorientation of two adjacent grains is equal to the angle between the γ
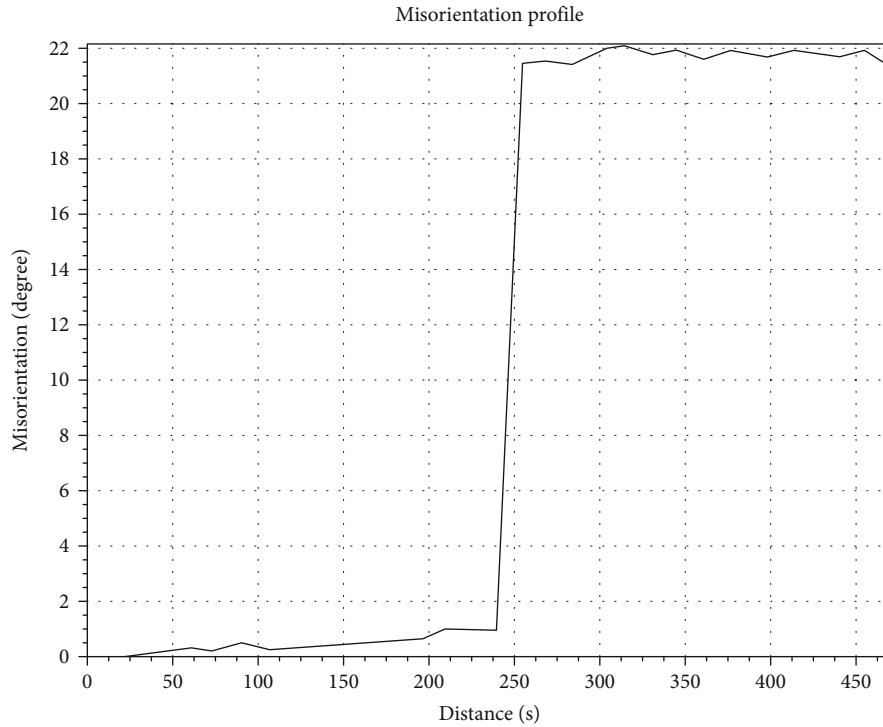
FIGURE 2: Misorientation of the as-cast bicrystal DD5 specimen measured by the line scanning of EBSD.
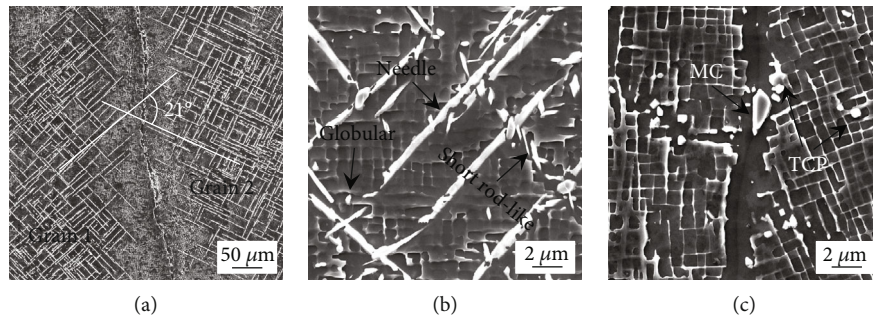

(a)   (b)   (c)

FIGURE 3: (a) SEM observation of the needle-like TCP phase in the bicrystal DD5 superalloy annealed at 950°C for 1000 h. (b) SEM micrograph of three TCP morphologies (needle-like, short rod-like, and globular). (c) SEM micrograph of the globular TCP phase and MC carbide at the grain boundary.

phase channels of two adjacent grains and the angle between the secondary dendritic arms of two adjacent grains.

Figure 3 presents the morphologies of the TCP phase that precipitated in the bicrystal superalloy during long-term aging at 950°C for 1000 h. As is shown in Figure 3(a), there was almost no TCP phase at the grain boundary, and a large number of needle-like TCP phases are parallel or perpendicular to each other precipitate on the dendrite. The needle-like TCP phases precipitate along the <110> crystal direction on the {111} crystal plane, and they are parallel or perpendicular to each other on the {001} crystal plane. In addition, the angle between the needle-like TCP phases of two adjacent grains is about 21°. This is consistent with the results in Figure 2. However, the direction of the needle-like TCP phase is not consistent with that of the γ phase channel, but at an angle

of 45°, as shown in Figure 3(b). The TCP phase is needle-like, short rod-like, and granular, as is shown in Figure 3(b). There are bigger MC carbides and small globular TCP phases at the grain boundary.

Figure 4 presents the morphologies of the TCP phase that precipitated near the grain boundaries during long-term aging at 950°C. After aging for 100 h, there is no any TCP phase that precipitated at the dendrites and grain boundary, and there is a large piece of the irregular γ' phase at the grain boundary, as shown in Figure 4(a). After aging for 500 h, there is a small amount of needle-like TCP phases parallel or perpendicular to each other and small granular TCP at the dendrite, and there is no TCP phase that precipitated at the grain boundary, as shown in Figure 4(b). After aging for 1000 h, a large number of needle-like TCP phases
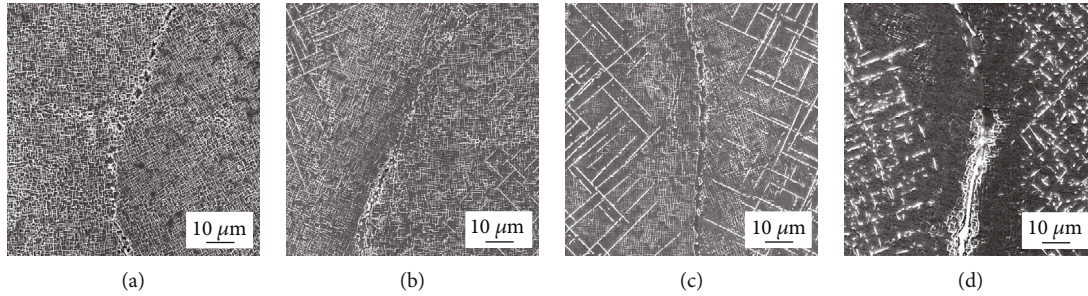
FIGURE 4: SEM micrographs of TCP phases in the grain boundaries annealed at 950°C for different hours: (a) 100 h, (b) 500 h, (c) 1000 h, and (d) 2000 h.
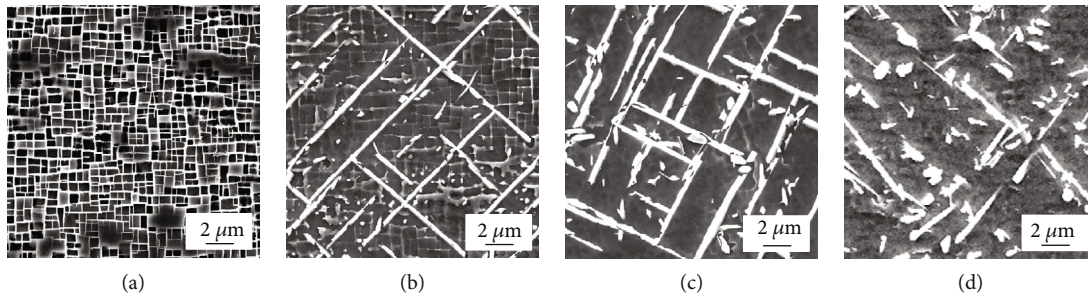

FIGURE 5: SEM micrographs of TCP phases in the dendrite trunks annealed at 950°C for different hours: (a) 100 h, (b) 500 h, (c) 1000 h, and (d) 2000 h.

perpendicular to each other and big granular TCP appear at the dendrite and massive carbides begin to precipitate on the grain boundaries, as shown in Figure 4(c). After aging for 2000 h, the needle-like TCP phase at the dendrite decomposes into granular and short rod-like phases, as shown in Figure 4(d).

Figure 5 shows the morphologies of the TCP phase that precipitated on the dendrite during long-term aging at 950°C. After aging for 100 h, there is no TCP phase that precipitated in the dendrite trunk, only the black γ' phase and white γ phase, as shown in Figure 5(a), which is consistent with that of the low magnification of Figure 4(a). After aging for 500 h, needle-like, granular, and short rod-like TCP phases precipitate at the dendrite trunk as shown in Figure 5(b). However, granular and short rod-like TCP phases are too small to be seen clearly; only the needle-like TCP phase can be seen in Figure 4(b). After aging for 1000 h, the needle-like TCP phases begin to decompose and transform into granular and short rod-like ones, as shown in Figure 5(c). However, at low magnification (Figure 4(c)), granular and short rod-like TCP phases are too small to be seen clearly; only the needle-like TCP phase can be seen. After aging for 2000 h, as shown in Figure 5(d), almost all needle-like TCP phases decompose into granular and short rod-like ones, which is consistent with that of the low magnification of Figure 4(d).

It can be derived from Figures 4 and 5 that with increasing aging time, the TCP phase gets coarser. This phenomenon is similar to the previous investigations [24, 25]. The needle-like TCP phases first coarsened and then decomposed. The granular TCP coarsened first and then branched.
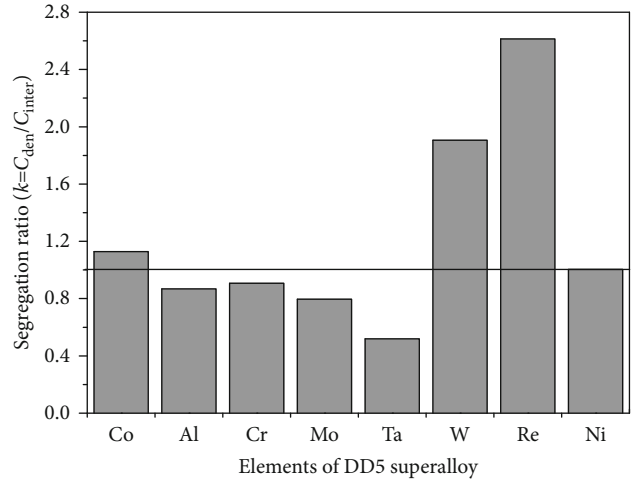
FIGURE 6: The element segregation of the as-cast DD5 superalloy.

It can be inferred from Figure 4 that TCP phases preferentially precipitate at the dendritic trunk, but it is difficult to precipitate at the interdendrite/grain boundary. This is caused by the segregation of the constituent elements of the TCP phase. The chemical composition of the TCP phase is made up of Cr, Mo, W, and Re. For superalloy containing Re, the TCP phase usually has a high content of Re. The element segregation of the as-cast DD5 superalloy is shown in Figure 6. The segregation ratio of Re and W is 2.6 and 1.9, respectively. The segregation ratio of Cr and Mo is 0.9 and 0.8, respectively, which is close to 1. The dendritic

segregation of W and Re is serious, while the interdendritic segregation of Cr and Mo is not as intense as that for W and Re. In addition, the TCP phase contains more Re, so the TCP phase preferentially precipitates at the dendrite trunk.

4. Conclusions

(1) When the [001] crystallographic orientation of two adjacent grains is the same, the misorientation of the adjacent grains is not only the angle between the γ phase channel of two adjacent grains but also the angle between the secondary dendrite arms of two adjacent grains. Although the direction of the needle-like TCP phase is not consistent with that of the γ phase channel, but at an angle of 45°, the angle of the needle-like TCP phase of two adjacent grains is equal to the misorientation of two adjacent grains

(2) In the process of long-term aging, the needle-like TCP phase gradually decomposes and transforms into granular and short rod-like ones

(3) The TCP phases precipitate preferentially at the dendrite, but it is difficult to precipitate at the interdendrite/grain boundary, which is caused by the segregation of the constituent elements of the TCP phase to the dendrite

Data Availability

The data used to support the findings of this study are available from the corresponding author upon request.

Conflicts of Interest

The authors declare that they have no competing interests.

Acknowledgments

References

[1] J. T. Guo, *Superalloy Materials*, Science Press, Beijing, China, 2008.

[2] A. K. Sinha, "Topologically Close-Packed Structures of Transition Metal Alloys," *Progress in Materials Science*, vol. 15, no. 2, pp. 81–185, 1972.

[3] R. Darolia, D. F. Lahrman, R. D. Field, and R. Sisson, "Formation of topologically closed packed phases in nickle base single crystal superalloys," in *Superalloys 1988*, pp. 255–264, TMS, Warrendale, 1988.

[4] C. M. F. Rae and R. C. Reed, "The precipitation of topologically close-packed phases in rhenium-containing superalloys," *Acta Materialia*, vol. 49, no. 19, pp. 4113–4125, 2001.

[5] F. C. Frank and J. S. Kasper, "Complex alloy structures regarded as sphere packings. I. Definitions and basic principles," *Acta Crystallographica*, vol. 11, no. 3, pp. 184–190, 1958.

[6] F. C. Frank and J. S. Kasper, "Complex alloy structures regarded as sphere packings. II. Analysis and classification of representative structures," *Acta Crystallographica*, vol. 12, no. 7, pp. 483–499, 1959.

[7] C. B. Shoemaker and D. Shoemaker, *Developments in the Structural Chemistry of Alloy Phases*, Plenum Press, 1969.

[8] S. Andersson, "Structures related to the β-tungsten or Cr_3Si structure type," *Journal of Solid State Chemistry*, vol. 23, no. 1-2, pp. 191–204, 1978.

[9] K. H. Kuo, H. Q. Ye, and D. X. Li, "Tetrahedrally close-packed phases in superalloys: new phases and domain structures observed by high-resolution electron microscopy," *Journal of Materials Science*, vol. 21, no. 8, pp. 2597–2622, 1986.

[10] M. Simonetti and P. Caron, "Role and behaviour of μ phase during deformation of a nickel-based single crystal superalloy," *Materials Science and Engineering: A*, vol. 254, no. 1-2, pp. 1–12, 1998.

[11] J. Zhu and H. Q. Ye, "On the microstructure and its diffraction anomaly of the μ phase in superalloys," *Scripta Metallurgica et Materialia*, vol. 24, no. 10, pp. 1861–1866, 1990.

[12] H. M. Tawancy, "Precipitation characteristics of μ-phase in wrought nickel-base alloys and its effect on their properties," *Journal of Materials Science*, vol. 31, no. 15, pp. 3929–3936, 1996.

[13] X. Z. Qin, J. T. Guo, C. Yuan, G. X. Yang, L. Z. Zhou, and H. Q. Ye, "μ-Phase behavior in a cast Ni-base superalloy," *Journal of Materials Science*, vol. 44, no. 18, pp. 4840–4847, 2009.

[14] K. Y. Cheng, C. Y. Jo, T. Jin, and Z. Q. Hu, "Precipitation behavior of μ phase and creep rupture in single crystal superalloy CMSX-4," *Journal of Alloys and Compounds*, vol. 509, no. 25, pp. 7078–7086, 2011.

[15] K. Zhao, L. H. Lou, Y. Wen, H. Li, and Z. Q. Hu, "Nucleation and growth of μ phase," *Journal of Materials Science*, vol. 39, no. 1, pp. 369–371, 2004.

[16] P. A. Carvalho, H. S. D. Haarsma, B. J. Kooi, P. M. Bronsveld, and J. T. M. De Hosson, "HRTEM study of Co_7W_6 and its typical defect structure," *Acta Materialia*, vol. 48, no. 10, pp. 2703–2712, 2000.

[17] P. A. Carvalho and J. T. M. De Hosson, "Stacking faults in the Co_7W_6 isomorph of the μ phase," *Scripta Materialia*, vol. 45, no. 3, pp. 333–340, 2001.

[18] K. Hiraga, T. Yamamoto, and M. Hirabayashi, "Intermetallic compounds of the μ- and P-phases of Co_7Mo_6 studied by 1 MV electron microscopy," *Transactions of the Japan Institute of Metals*, vol. 24, no. 6, pp. 421–428, 1983.

[19] Y. Qiao, D. Xu, S. Wang et al., "Corrosion and tensile behaviors of Ti–4Al–2V–1Mo-1Fe and Ti–6Al–4V titanium alloys," *Metals*, vol. 9, no. 11, p. 1213, 2019.

[20] A. Sato, H. Harada, T. Yokokawa et al., "The effects of ruthenium on the phase stability of fourth generation Ni-base single crystal superalloys," *Scripta Materialia*, vol. 54, no. 9, pp. 1679–1684, 2006.

[21] Y. Qiao, J. Chen, H. Zhou et al., "Effect of solution treatment on cavitation erosion behavior of high-nitrogen austenitic stainless steel," *Wear*, vol. 424-425, pp. 70–77, 2019.

[22] L. Wang, J. Shen, Y. Zhang, and H. Fu, "Microstructure, fracture toughness and compressive property of as-cast and

directionally solidified NiAl-based eutectic composite," *Materials Science and Engineering A*, vol. 664, pp. 188–194, 2016.

[23] L. Wang and J. Shen, "Effect of withdrawal rate on the microstructure and room temperature mechanical properties of directionally solidified NiAl-Cr(Mo)-(Hf, Dy)-4Fe alloy," *Journal of Alloys and Compounds*, vol. 663, pp. 187–195, 2016.

[24] L. Wang, J. Shen, G. Zhang et al., "Stability of lamellar structure of directionally solidified NiAl-28Cr-6Mo eutectic alloy at different withdrawal rates and temperatures," *Intermetallics*, vol. 94, pp. 83–91, 2018.

[25] L. Wang, G. Zhang, J. Shen et al., "A true change of NiAl-Cr(Mo) eutectic lamellar structure during high temperature treatment," *Journal of Alloys and Compounds*, vol. 732, pp. 124–128, 2018.

Research Article

Atmospheric Corrosion Analysis and Rust Evolution Research of Q235 Carbon Steel at Different Exposure Stages in Chengdu Atmospheric Environment of China

Zhigao Wang [iD],[1] **Mei Wang,**[2] **Jie Jiang,**[3,4] **Xinsheng Lan,**[1] **Fangqiang Wang,**[1] **Zhi Geng,**[1] **and Qianqian Tian**[1]

[1]*State Grid Sichuan Electric Power Research Institute, Chengdu 610041, China*
[2]*School of Mechanical Engineering, Sichuan University, Chengdu 610065, China*
[3]*State Key Laboratory of Geohazard Prevention and Geoenvironment Protection (Chengdu University of Technology), Chengdu 610059, China*
[4]*College of Environment and Civil Engineering, Chengdu University of Technology, Chengdu 610059, China*

Correspondence should be addressed to Zhigao Wang; wzg33@163.com

In order to effectively reduce and retard corrosion of the power transmission and transformation equipment in Chengdu power grid and to improve power supply reliability, Q235 carbon steel material which is the most widely used metal material in power grid was selected as the targeted research object in this article. Exposure experiments were performed in urban atmospheric environment of Chengdu city in the southwest region of China. The corrosion behavior of Q235 carbon steel material was investigated at different seasons. The macro- and micromorphologies after corrosion were observed using a digital camera and scanning electron microscopy (SEM), respectively. Element distribution of the rust layer and the corrosion products was characterized by energy-dispersive spectroscopy (EDS), X-ray diffraction (XRD), and Fourier transform infrared spectroscopy (FTIR); the corrosion mechanism was also briefly analyzed.

1. Introduction

In recent decades, with the construction scale of China's power transmission and transformation project becoming larger and larger, the corrosion problem of power transmission and transformation equipment is increasingly prominent, which has seriously affected safe operation of the power grid system [1–7]. With long-term operation outdoor, the metal components of the power transmission and transformation equipment are subject to erosion and damage due to various harsh environments and are prone to corrosion and failure, reducing the reliability of the power transmission and transformation equipment and generating potential safety hazards [8–10]. For instance, the transformer radiator in a 500 kV substation suffered corrosion perforation, resulting in oil leakage malfunction, which had to be replaced after

power failure. In another 220 kV substation, corrosion of the outdoor terminal cabinet caused bad sealing and moisture in the cabinet, which easily caused component fault and equipment misoperation. Corrosion of the high-voltage disconnecting switch at the connecting rod and gear plate parts in a 110 kV substation caused the operating mechanism to be jammed, and the switch could not reach the designated position. In a 220 kV transmission line, corrosion failure of the electric power fitting led to the conductor disconnecting or falling, causing power outage accidents.

Chengdu is a megacity in the southwest region of China with a population of 16.04 million and an area of 14,600 square kilometers. For Chengdu power grid, there are 410 substations above 35 kV with a total substation capacity of 61.76 million kVA, and there are 8808 km of transmission lines above 35 kV. Chengdu has a humid and rainy climate

TABLE 1: Chemical composition of Q235 carbon steel.

Chemical composition (wt%)						
Element	C	Si	Mn	S	P	Fe
wt%	0.16	0.20	0.61	0.023	0.0019	Balance

with the annual average temperature of 16.6°C and the annual average relative humidity of 81%; also, its annual average rainfall is 966.9 mm [11]. In addition, the air environment in Chengdu has been seriously polluted in recent years; the major pollutants include SO_2, NO_2, O_3, CO, PM_{10}, and $PM_{2.5}$ [12]. Both the climatic and environmental factors will accelerate the corrosion rate of the metal materials. The interaction of various factors influencing corrosion is complex, reflecting dynamic and evolutive characteristics for the corrosion of the metal materials. The diversity of the atmospheric pollutants also leads to difference in the corrosion layer. However, corrosion studies concerning the metal materials used in power grid in the specific atmospheric environment of Chengdu city are very scarce. Thus, it is essential to investigate the corrosion behavior of the metal materials in Chengdu atmospheric environment, which is very important to guarantee safe operation of the power transmission and transformation equipment in Chengdu power grid.

In this study, on the basis of rainy, high-humidity, and high-acidic pollution characteristics of the atmospheric corrosion environment in Chengdu, the corrosion behavior and regularity of Q235 carbon steel material which has been widely used in power transmission and transformation projects were evaluated after long-term exposure to ambient air. In particular, formation and evolution mechanism of the corrosion layer of Q235 carbon steel at different exposure stages were researched. The findings obtained in this study will be helpful to develop targeted corrosion protection strategy for urban atmospheric environment in Chengdu, for the purpose of effectively controlling corrosion and ensuring safe and stable operation of Chengdu power grid.

2. Materials and Methods

2.1. Materials and Sample Preparation.
Q235 carbon steel material was selected for corrosion tests in this study. Q235 carbon steel material was one of the most widely used metallic materials in power transmission and transformation projects. The chemical composition of Q235 carbon steel is shown in Table 1.

All the Q235 carbon steel samples used in atmospheric exposure experiments were cut to 100 mm × 50 mm × 3 mm by wire electrode cutting. Then, they were ground by machinery grinding to 800-grit smooth surface. The surface oil was cleaned by an ultrasonic cleaner in anhydrous alcohol, and then, the specimens were dried with a blow dryer and stored in a drying vessel.

2.2. Exposure Experiments.
The atmospheric exposure experiments were undertaken at Chengdu atmospheric corrosion station of China. The prepared Q235 carbon steel specimens were installed on a test rack with an inclination angle of 45°

and exposed to ambient air, horizontal to the sky and facing south, where they were exposed for one year (from Nov 2016 to Nov 2017). The environmental parameters such as temperature, relative humidity, rainfall precipitation, pH value of rainfall, SO_2 concentration, and Cl^- settling rate during the atmospheric exposure tests in Chengdu are listed in Table 2.

Q235 carbon steel specimens were collected each time after exposure to ambient air for consecutive 15, 30, 90, 180, and 365 days, respectively. They were used to analyze the corrosion process, corrosion morphology, and rust layer products.

2.3. Macroscopic Corrosion Morphology Observation.
Using a digital camera (Canon, PowerShot SX700 HS) to take macroscopic pictures of the Q235 carbon steel specimens after 15, 30, 90, 180, and 365 days of exposure in Chengdu atmospheric environment, the macroscopic corrosion morphologies were observed.

2.4. Scanning Electron Microscope and Element Analysis.
The microstructures and the cross-section morphologies of the Q235 carbon steel specimens were observed by SEM (Hitachi, SU3500). Energy-dispersive spectroscopy (EDS, Hitachi) was used to determine the elements of the corrosion products.

2.5. Corrosion Product Analysis.
The crystalline phase of the rust layer was identified using a powder X-ray diffractometer (XRD, Empyrean). The rust layer was removed from the specimen and fully ground in an agate mortar body with 5 μm particle size. The 2 theta angle was 10°~90°. The results of XRD were analyzed by Jade 6.0 software.

2.6. FTIR Analysis.
The composition of the rust layer was analyzed by Fourier transform infrared spectroscopy (FTIR) on a Nicolet 6700 FTIR spectrophotometer (Nicolet, USA) between 4000 and 500 cm^{-1} with a resolution of 2 cm^{-1}.

3. Results and Discussion

3.1. Macroscopic Corrosion Morphology.
Q235 carbon steel specimens were exposed in Chengdu atmospheric environment for 15, 30, 90, 180, and 365 days, respectively. The corrosion weight loss after 365 days of exposure was 17.42 μm/a. The retrieval samples were photographed with a digital camera. Figure 1 shows the macroscopic corrosion morphologies of the Q235 carbon steel samples with different exposure time in Chengdu station. Figures 1(a)–1(e) represent the corrosion morphologies on the front sides of the specimens at different exposure time, while Figures 1(a')–1(e') represent the corrosion morphologies on the back sides of the specimens at different exposure time. When the Q235 carbon steel material was exposed for 15 days, most region of the specimen on the front side had been overlaid by a rust layer as shown in Figure 1(a); part of the substrate metal was still bared; the surface appeared to have uneven brown color. Figure 1(a') shows the corrosion morphology of the Q235 carbon steel specimen on the back side; the corrosion degree of the back side was far lower than that of the front side; there

TABLE 2: The environmental parameters during the atmospheric exposure test in Chengdu.

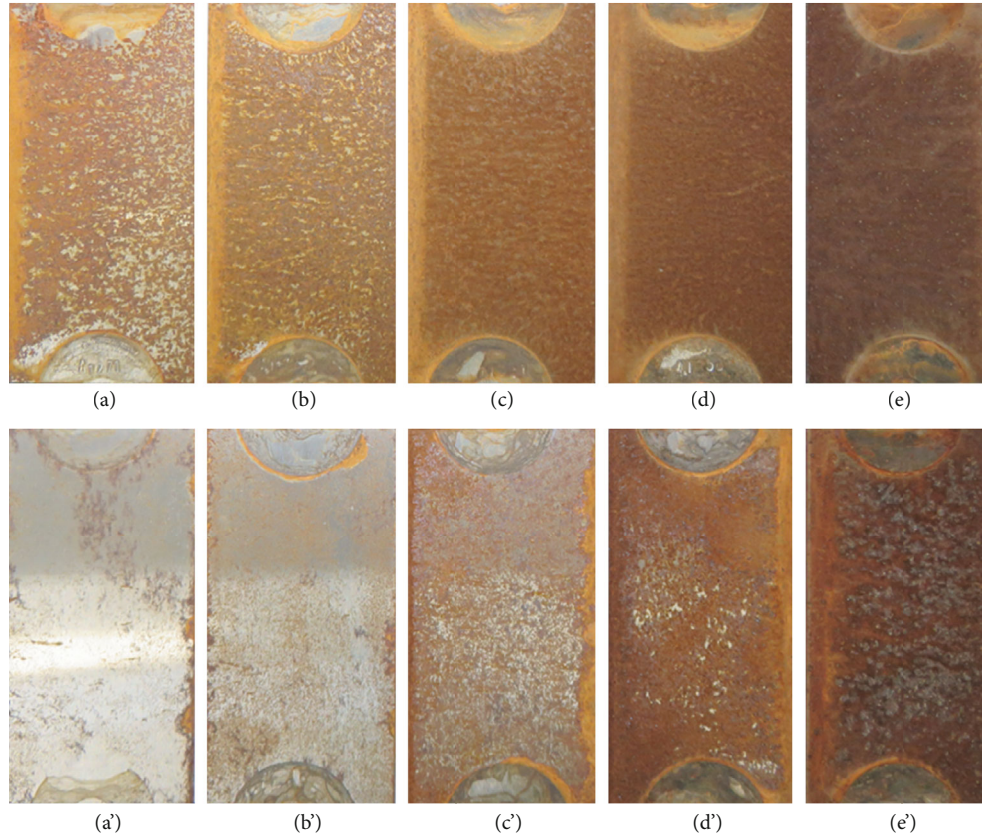| Place	Temperature (˚C)	Relative humidity (%)	Rainfall precipitation (mm/a)	pH value of rainfall	SO_2 concentration ($\mu g/m^3$)	Cl^- settling rate ($mg/m^2/d$)
Chengdu city	16.6	81	966.9	6.4	11.3	0.37

FIGURE 1: Macroscopic corrosion morphologies of the Q235 carbon steel specimens with different exposure time in Chengdu station: (a) 15 days on the front side, (a′) 15 days on the back side, (b) 30 days on the front side, (b′) 30 days on the back side, (c) 90 days on the front side, (c′) 90 days on the back side, (d) 180 days on the front side, (d′) 180 days on the back side, (e) 365 days on the front side, and (e′) 365 days on the back side.

were few rust spots; most region of the substrate metal was still naked. After exposure for 30 days, Figure 1(b) displays the corrosion morphology on the front side of the specimen; the area of the rust layer continued to expand; it could be found that bared substrate metal decreased significantly. At the same time, on the back side of the specimen shown in Figure 1(b′), the number of the rust spots increased and the region of the rust layer was enlarged; however, the corrosion degree of the back side was still much lower than that of the front side. When the Q235 carbon steel specimen was exposed for 90 days, Figure 1(c) exhibits that the front side of the specimen had been completely covered by the brown rust layer and the outer rust layer was loose. Figure 1(c′) shows the back-side morphology of the specimen; the number of the rust spots was obviously increasing and intensive, but they had not completely covered the substrate metal. At the exposure time of 180 days, the front side of the specimen presented a homogeneous brown rust layer, and compared

with the early exposure periods, the rust layer was becoming denser (Figure 1(d)). Figure 1(d′) presents that the corrosion degree of the back side of the specimen continued to grow; the rust layer had almost completely covered the substrate metal; only a small amount of substrate metal remained uncovered. When the Q235 carbon steel specimen was exposed for 365 days, Figure 1(e) shows that the front side of the specimen appeared dark brown color and demonstrated a compact rust layer. In Figure 1(e′), the corrosion degree of the back side of the specimen had been significantly increased compared with that of 180 days, the rust layer presented reddish brown color, and its outer rust layer was more loose than that of the front side. Through the morphological observation from the macroscopic angle, in the earlier exposure periods of 15 days~180 days, the corrosion degree of the Q235 carbon steel specimen on the front side was more serious than that on the back side. This is because the corrosion on the front side of the specimen was mainly caused by rain
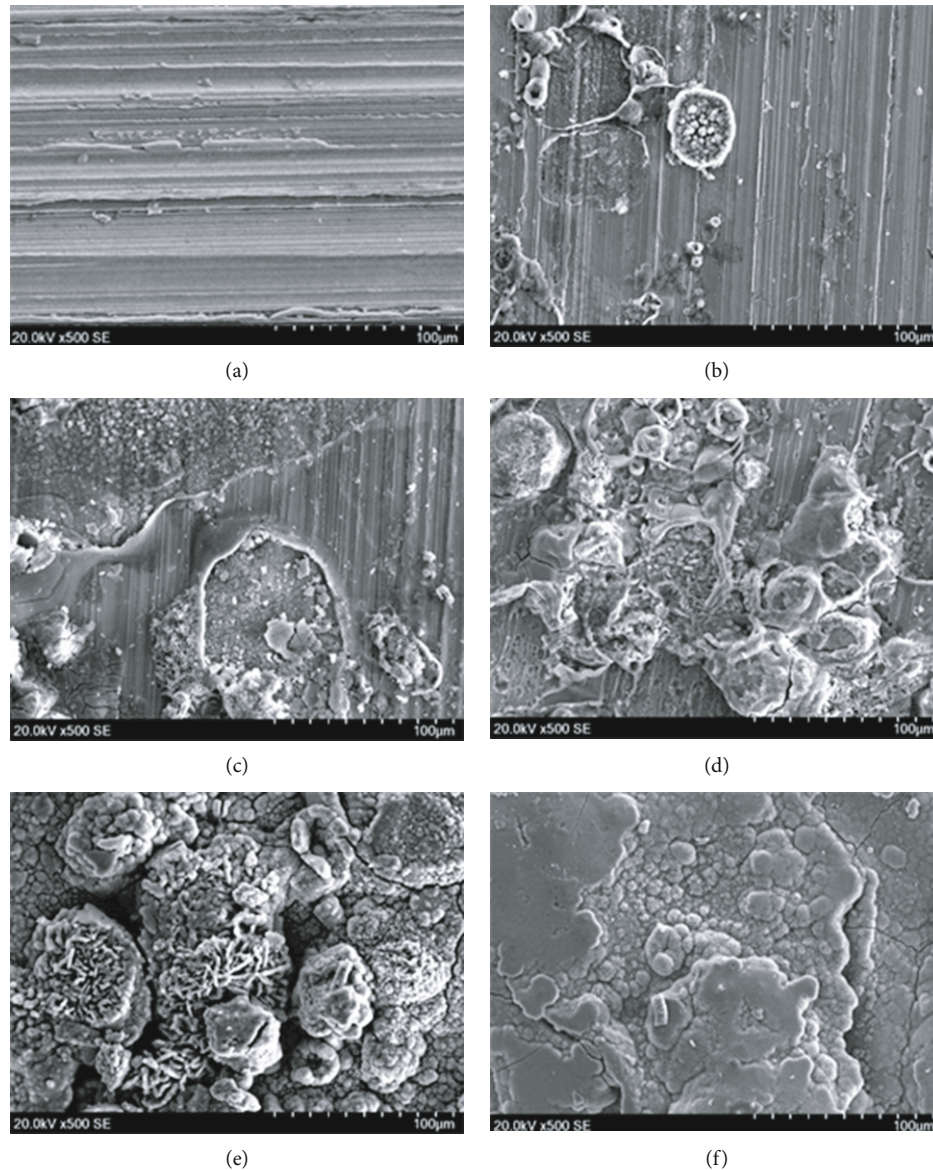
(a)

(b)

(c)

(d)

(e)

(f)

FIGURE 2: Microscopic corrosion morphologies of the Q235 carbon steel specimens with different exposure time in Chengdu station: (a) 0 day, (b) 15 days, (c) 30 days, (d) 90 days, (e) 180 days, and (f) 365 days.

water, condensation, and moist atmosphere. However, on the back side of the specimen, the rain water and condensation were difficult to attach, so its corrosion was principally caused by moist atmosphere. In the later exposure period of 365 days, the front side of the specimen had formed a relatively dense rust layer, moisture was not easily to permeate, so the corrosion growth slowed down. While the back side of the specimen was covered by a relatively loose rust layer, moisture could be easily permeated through the outer rust layer, so the corrosion continued to grow. In addition to exposure time, season also affected the corrosion process. The initial 15 days and 30 days were in winter, with less rainfall and low humidity, and led to low corrosion degree. 90 days of exposure was in spring; the corrosion degree was higher than that in winter. 180~365 days were in summer and autumn, with the most rain and the highest corrosion degree.

3.2. Microscopic Corrosion Morphology. SEM was performed to observe the surface microscopic corrosion morphologies of the Q235 carbon steel samples with different exposure time in Chengdu station; the results are shown in Figure 2. Figures 2(a)–2(f) represent the front-side surface morphologies of the Q235 carbon steel samples exposed for 15, 30, 90, 180, and 365 days, respectively. The SEM magnifications were all set as 500 times.

It can be observed from Figure 2(a) that the Q235 carbon steel specimen before exposure showed a striated surface after magnification, which was due to the surface polishing to the substrate metal. When the Q235 carbon steel sample was exposed for 15 days, several circular areas in Figure 2(b) were local corrosion points, where the corrosion products were composed of spherical particles with different sizes, and the remaining striated region was the uncorroded substrate metal. After 30 days of exposure as reflected in
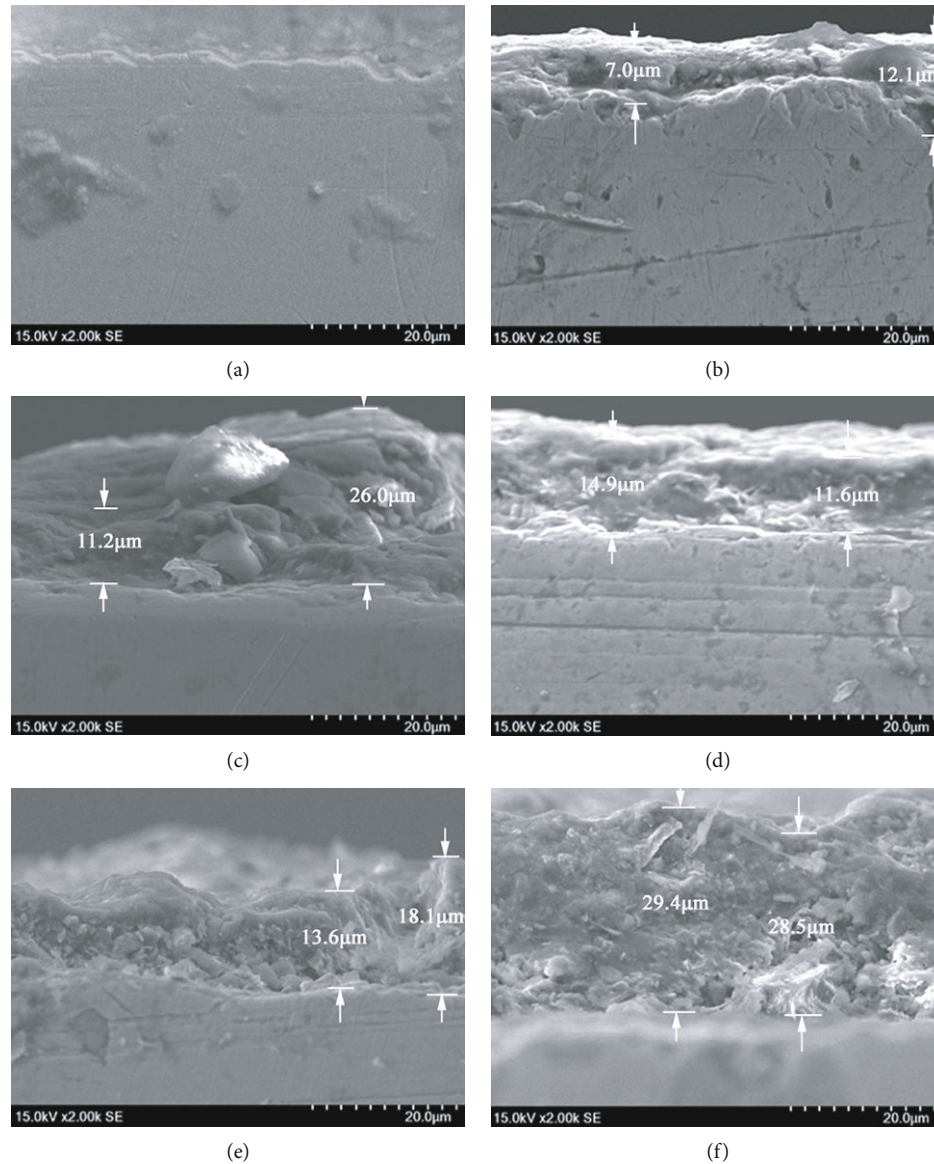
(a)

(b)

(c)

(d)

(e)

(f)

FIGURE 3: Microscopic corrosion morphologies of the Q235 carbon steel specimens in section view with different exposure time in Chengdu station: (a) 0 day, (b) 15 days, (c) 30 days, (d) 90 days, (e) 180 days, and (f) 365 days.

Figure 2(c), the corrosion area continued to increase, and the surface topography was uneven. The corrosion products were dominated by spherical and irregular particles. When the Q235 carbon steel specimen was exposed for 90 days, Figure 2(d) exhibits that most areas of the substrate metal were covered by the corrosion products with further expansion of the corrosion area, and the surface topography was uneven. A number of vesicular structures in different sizes could be observed; part of them were damaged; spherical, rod-like, and needle-like corrosion products could be seen under the damaged surface. At the exposure time of 180 days, Figure 2(e) reveals that the corrosion products of the Q235 carbon steel were composed of a large number of rod-like and spherical particles; rod-like and spherical particles aggregated into clusters; clusters of the corrosion products were loose and porous; also, they were more conducive to water adsorption, which could accelerate the corrosion rate of the carbon steel. When the Q235 carbon steel sample was exposed for 365 days, Figure 2(f) demonstrates that most of the corrosion product particles had joined together to form layered corrosion products; few spherical particles remained closely connected; the surface of the rust layer appeared compact and smooth, but there were still cracks on it.

3.3. Microscopic Corrosion Morphology in the Section View. Figure 3 shows the microscopic corrosion morphologies of the Q235 carbon steel samples in the section view, which were exposed in Chengdu atmospheric environment for 0, 15, 30, 90, 180, and 365 days, respectively. The SEM magnifications were all set as 2000 times. For all the figures, the under part was the carbon steel substrate, and the upper part was the rust layer. As can be seen from Figure 3, the corrosion depth of the Q235 carbon steel specimen increased with the exposure time growth. As shown in Figure 3(b), at the
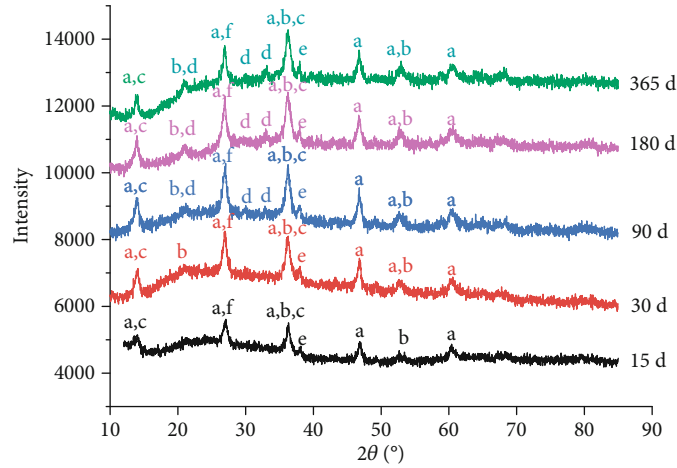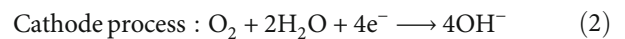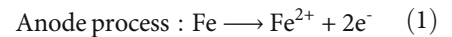
Figure 4: XRD spectra of the corrosion products of the Q235 carbon steel samples exposed at different periods in Chengdu station: (a) γ-FeOOH, (b) α-FeOOH, (c) $Fe(OH)_3$, (d) Fe_3O_4, (e) γ-Fe$_2$O$_3$, and (f) $FeSO_4 \cdot nH_2O$.

early exposure period of 15 days, the rust layer thickness of the Q235 carbon steel specimen was small. Also, the rust layer was uneven, the largest corrosion depth reached 12.1 μm, and the minimum corrosion depth was 7.0 μm. When the Q235 carbon steel material was exposed for 30 days, the rust layer thickness was higher with the exposure days increasing, the corrosion thickness was between 11.2 μm and 26.0 μm, and the rust layer thickness was uneven, as shown in Figure 3(c). There also exist granular corrosion products of different sizes in the rust layer, which were consistent with the results of the uneven surface morphology and granular corrosion products with different sizes observed in Figure 2(c). At the exposure time of 90 days as reflected in Figure 3(d), the rust layer thickness was between 11.6 μm and 14.9 μm, which was smaller than that of 30 days. Also, the fluctuation of the rust layer thickness gradually became smaller. This is because most parts of the substrate metal were covered by the corrosion products, and the loose corrosion products on the surface had gradually fallen off. When the Q235 carbon steel material was exposed for 180 days, Figure 3(e) shows that the thickness of the rust layer was further increased, with a range of 13.6~18.1 μm; also, the corrosion products of spherical and rod-like particles could be observed, which was consistent with the observation of the surface morphology of the rust layer in Figure 2(e). Figure 3(f) exhibits the cross-section morphology of the Q235 carbon steel sample exposed for 365 days. As can be seen, the rust layer was thickening apparently with the depth of 28.5~29.4 μm, which was fairly even. Besides, the surface of the rust layer was relatively dense, and the bottom of the rust layer was relatively loose with granular corrosion products.
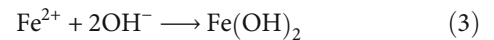
3.4. XRD Analysis. For the samples of Q235 carbon steel exposed after different stages in Chengdu station, the surface rust residue was scraped for XRD analysis; the XRD results can be seen in Figure 4. When the Q235 carbon steel material was exposed in the atmospheric environment of Chengdu city for 15 days, the corrosion products mainly contained γ-FeOOH, α-FeOOH, $Fe(OH)_3$, γ-Fe$_2$O$_3$, and $FeSO_4 \cdot nH_2O$.

At this time, the diffraction peak of α-FeOOH was not obvious, which indicated that there was little corrosion product of α-FeOOH. For the exposure time of 30 days, the corrosion products were the same as those of 15 days; the peak intensities of all the products increased, demonstrating that the content of all the corrosion products increased. In particular, the increasing strengths of the peaks corresponding to γ-FeOOH and α-FeOOH were more obvious, showing that the contents of the corrosion products γ-FeOOH and α-FeOOH increased considerably. For the corrosion products of 90 days of exposure time and 180 days of exposure time, Fe_3O_4 was found in the corrosion products; the peak intensities of α-FeOOH and γ-Fe$_2$O$_3$ were also enhanced. When the Q235 carbon steel specimen was exposed for 365 days, the corrosion products mainly contained γ-FeOOH, α-FeOOH, $Fe(OH)_3$, γ-Fe$_2$O$_3$, Fe_3O_4, and $FeSO_4 \cdot nH_2O$. Compared with the previous corrosion periods, the peak strength of the γ-FeOOH decreased, indicating that the content of the unstable corrosion product γ-FeOOH was reduced. However, the peak strengths of α-FeOOH, γ-Fe$_2$O$_3$, and Fe_3O_4 increased significantly, showing that the contents of the stable corrosion products α-FeOOH, γ-Fe$_2$O$_3$, and Fe_3O_4 became more.

Through analysis on the mechanism of chemical reaction in the process of atmospheric corrosion of carbon steel, at the initial stage of exposure, the corrosion reaction process of carbon steel was as follows:

$$\text{Anode process}: Fe \longrightarrow Fe^{2+} + 2e^- \quad (1)$$

$$\text{Cathode process}: O_2 + 2H_2O + 4e^- \longrightarrow 4OH^- \quad (2)$$

OH^- combined with Fe^{2+} to form $Fe(OH)_2$:

$$Fe^{2+} + 2OH^- \longrightarrow Fe(OH)_2 \quad (3)$$

$Fe(OH)_2$ was not stable and was gradually oxidized to FeOOH by O_2 dissolved in the electrolyte solution:

$$4Fe(OH)_2 + O_2 \longrightarrow 4FeOOH + 2H_2O \quad (4)$$

TABLE 3: EDS component analysis of the element weight percentage (wt%) with different exposure time.

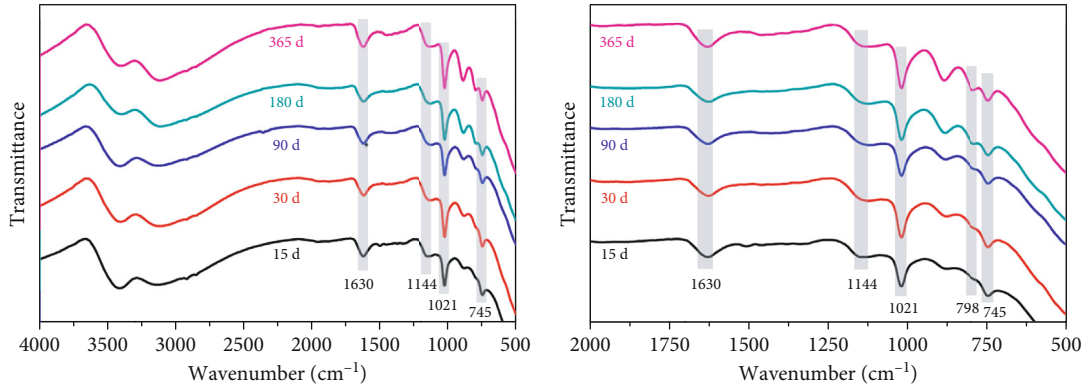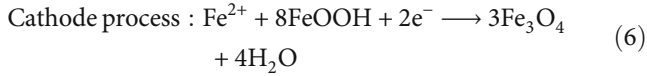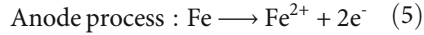| Element (wt%)	15 days	30 days	90 days	180 days	365 days
C	10.01	12.08	10.59	6.43	11.67
N	5.16	5.44	5.57	4.66	5.06
O	37.37	35.1	35	34.96	36.2
S	0.23	0.05	0.12	0.07	0.15
Cl	0.07	0	0.1	0.07	0.1
Fe	47.16	47.33	48.62	53.8	46.83

FIGURE 5: FTIR spectra of the corrosion products of the Q235 carbon steel samples exposed at different periods in Chengdu station.

When the complete rust layer was formed on the surface of carbon steel, the corrosion reaction process was as follows:

$$\text{Anode process}: Fe \longrightarrow Fe^{2+} + 2e^- \quad (5)$$

$$\text{Cathode process}: Fe^{2+} + 8FeOOH + 2e^- \longrightarrow 3Fe_3O_4 + 4H_2O \quad (6)$$

Among the corrosion products through XRD analysis, γ-FeOOH was a kind of volatile corrosion product; also, it was the main component of the rust layer in the early corrosion stage of carbon steel material. It could dehydrate to form γ-Fe$_2$O$_3$. However, after long-term exposure, it could transform into Fe$_3$O$_4$ with more thermodynamic stability. Fe$_3$O$_4$ could be oxidized to α-FeOOH under the function of oxygen, α-FeOOH was a relatively stable corrosion product, and its grain was finer than that of γ-FeOOH. With the content of α-FeOOH increasing, the stability of the rust layer was enhanced, so the rust layer with longer exposure time was denser. The colloidal hydroxide Fe(OH)$_3$ contained a certain amount of crystal water; it could be dehydrated to form FeOOH or Fe$_2$O$_3$ under certain conditions. The formation of FeSO$_4 \cdot n$H$_2$O came from the adsorption of SO$_2$ in the atmosphere; it deposited on the surface of the wet rust layer and then reacted with Fe.

3.5. EDS Analysis. EDS surface scanning and element analysis were performed on the Q235 carbon steel samples after being exposed in Chengdu atmospheric environment for 15, 30, 90,

180, and 365 days, respectively. The EDS results are shown in Table 3; the rust layers with different exposure time had the main constituent elements of Fe and O. So the principal corrosion products of Q235 carbon steel material exposed in Chengdu station were the compounds containing Fe and O, which was consistent with the XRD analysis results of the corrosion products: γ-FeOOH, α-FeOOH, Fe$_3$O$_4$, and Fe$_2$O$_3$. At the same time, the rust layer also contained trace S, Cl, and N elements. The S element might be derived from SO$_2$ or sulfate deposited in the atmospheric environment, N elements might come from NO or NO$_2$ pollution, and Cl elements might come from chlorine ion pollution in the atmospheric environment.

3.6. FTIR Analysis. FTIR spectra of the corrosion products of the Q235 carbon steel samples exposed at different periods in Chengdu station are shown in Figure 5. From the infrared spectra of Figure 5, it could be seen that the characteristics peaks at 1144 cm^{-1}, 1021 cm^{-1}, and 745 cm^{-1} corresponded to the characteristic absorption of γ-FeOOH, illustrating that one kind of the corrosion products was γ-FeOOH. There was a strong absorption peak in the absorption band near 1630 cm^{-1}, because it was the curved vibration characteristic peak of -OH, indicating that there was a large amount of crystal water in the corrosion products. In addition, it can be seen that the characteristic absorption peak of the α-FeOOH at 798 cm^{-1} was gradually reflected with the exposure time increasing, indicating that in the later exposure time of 180 days and 365 days, γ-FeOOH started to transform to α-FeOOH gradually.

Among various hydroxyl oxides of iron, the electrochemical stability of α-FeOOH was the best, while other corrosion products such as β-FeOOH, γ-FeOOH, δ-FeOOH, and amorphous phase all had electrochemical activity, which were easy to be reduced. Hence, it had definite protective effect on the rust layer after the occurrence of α-FeOOH in the rust layer. When the Q235 carbon steel samples were exposed in high-humid atmospheric environment of Chengdu for 365 days, plenty of γ-FeOOH were formed. However, there was not a large number of corrosion product α-FeOOH detected in the rust layer because the corrosion time is not long enough. The results indicated that although the Q235 carbon steel specimen had formed a dense rust layer on the surface, its rust layer still showed the existence of electrochemical instability. Comprehensive analysis of the results of XRD and FTIR revealed that the corrosion products of Q235 carbon steel material exposed in Chengdu atmospheric environment for 365 days mainly contained γ-FeOOH, $Fe(OH)_3$, Fe_3O_4, and a small amount of α-FeOOH; also, a lot of water of crystallization exists in the corrosion products. Furthermore, with the growth of the exposure time, γ-FeOOH began to transform to α-FeOOH, so the electrochemical stability of the rust layer tended to increase.

4. Conclusions

(1) In the corrosion process of Q235 carbon steel material, the degree of corrosion on the front side was much greater than that on the back side. With exposure time increasing, the area of the rust layer expanded and the rust layer gradually became thicker

(2) With exposure time increasing, the surface microscopic corrosion morphologies changed from irregular particles and vesicle structures to rod-shaped and spherical particles and loose clusters. Finally, the corrosion products connected to the layered structure, and the surface rust layer was obviously dense and flat

(3) The corrosion products were mainly composed of γ-FeOOH, α-FeOOH, $Fe(OH)_3$, γ-Fe_2O_3, Fe_3O_4, and $FeSO_4 \cdot nH_2O$. In the later exposure periods, the proportions of α-FeOOH, γ-Fe_2O_3, and Fe_3O_4 were increased

Data Availability

The data used to support the findings of this study are included within the article.

Conflicts of Interest

The authors declare that there is no conflict of interest regarding the publication of this paper.

Acknowledgments

References

[1] Z. Y. Liu, *Electric power and energy in China*, China Electric Power Press, Beijing, China, 2012.

[2] Z. Y. Liu, *UHV AC and DC power grid*, China Electric Power Press, Beijing, China, 2013.

[3] Q. Yu, C. F. Dong, Y. H. Fang et al., "Atmospheric corrosion of Q235 carbon steel and Q450 weathering steel in Turpan, China," *Journal of Iron and Steel Research, International*, vol. 23, no. 10, pp. 1061–1070, 2016.

[4] A. De Marco, A. Screpanti, M. Mircea, A. Piersanti, C. Proietti, and M. F. Fornasier, "High resolution estimates of the corrosion risk for cultural heritage in Italy," *Environmental Pollution*, vol. 226, pp. 260–267, 2017.

[5] D. Persson, D. Thierry, and O. Karlsson, "Corrosion and corrosion products of hot dipped galvanized steel during long term atmospheric exposure at different sites world-wide," *Corrosion Science*, vol. 126, pp. 152–165, 2017.

[6] W. Han, G. C. Yu, and Z. Y. Wang, "Characterisation of initial atmospheric corrosion carbon steels by field exposure and laboratory simulation," *Corrosion Science*, vol. 49, no. 7, pp. 2920–2935, 2007.

[7] S. J. Oh, D. C. Cook, and H. E. Townsend, "Atmospheric corrosion of different steels in marine, rural and industrial environments," *Corrosion Science*, vol. 41, no. 9, pp. 1687–1702, 1999.

[8] Y. J. Zhi, D. M. Fu, D. W. Zhang, T. Yang, and X. G. Li, "Prediction and knowledge mining of outdoor atmospheric corrosion rates of low alloy steels based on the random forests approach," *Metals*, vol. 9, no. 3, p. 383, 2019.

[9] B. Liu, D. W. Wang, H. Guo, Z. H. Ling, and K. Cheung, "Metallic corrosion in the polluted urban atmosphere of Hong Kong," *Environmental Monitoring and Assessment*, vol. 187, no. 1, p. 4112, 2015.

[10] Y. Cai, Y. Zhao, X. Ma, K. Zhou, and Y. Chen, "Influence of environmental factors on atmospheric corrosion in dynamic environment," *Corrosion Science*, vol. 137, pp. 163–175, 2018.

[11] *Sichuan climate impact assessment in 2017*, Sichuan Provincial Meteorological Bureau, 2018.

[12] *Sichuan environmental bulletin in 2017*, Department of Ecological Environment of Sichuan Province, 2018.